Engineering Porous Silicon Nanoparticles for Delivery of Peptide Nucleic Acid Therapeutics

By

Kelsey Ross Beavers

Dissertation

Submitted to the Faculty of the

Graduate School of Vanderbilt University

in partial fulfillment of the requirements

for the degree of

DOCTOR OF PHILOSOPHY

in

Interdisciplinary Materials Science

May, 2017

Nashville, Tennessee

Approved:

Craig L. Duvall, Ph.D.
Sharon M. Weiss, Ph.D., M.S.
Jeremy W. Mares, Ph.D.
Raymond L. Mernaugh, Ph.D.
Todd D. Giorgio, Ph.D.
David W. Wright, Ph.D.
Kasey C. Vickers, Ph.D.

This work is dedicated to my husband and my family. Their unwavering love and support provided the foundation for every sentence in this thesis.

I would also like to dedicate this work to my first mentor, Dr. Lawrence Bottomley. Dr. B inspired me to earn my doctorate and shared with me the three basic rules of good science:

1. Know thine instrument
2. Test all assumptions
3. Think, dammit.

ACKNOWLEDGEMENTS

First and foremost, I would like to thank my two Ph.D. advisors: Professors Craig Duvall and Sharon Weiss. Their guidance and support, both individually and as a team, pushed me to be a better scientist, teacher, and leader. Their hard work made this project possible. I would like to thank the members of my thesis committee—Professors Jeremy Mares, Ray Mernaugh, Todd Giorgio, Kasey Vickers, and David Wright—for their insight, encouragement, and time. I would like to thank my colleagues in the VU Photonics, VU Biomaterials, Carrie Wiese, as well as all of the undergraduate students I had the pleasure to work with. Their contributions propelled this research farther than I had dreamed possible. I am also grateful to the members of K.A.T.T. for their support and guidance in my professional development.

I gratefully acknowledge Dr. Alexander Deiters for providing all cell lines used in this work. I am grateful to Dr. Wade Calcutt for his expertise in mass spectrometry, and to Dr. John McLean's group at Vanderbilt University for providing access and technical expertise with MADLI-MS. I am also thankful for Ms. Rossane Delapp and Dr. David Kosson in Vanderbilt's Department of Civil and Environmental Engineering for ICP-OES analysis of silicon content for biodistribution studies. This work was supported in part by the National Science Foundation (DMR-120701), the Department of Defense (DOD PRORP OR130302), the National Institutes of Health (R01 EB019409), and NSF Graduate Research Fellowships. Confocal Imaging was performed in part through the use of the VUMC Cell Imaging Shared Resource, (supported by NIH grants CA68485, DK20593, DK58404, HD15052, DK59637 and Ey008126). DLS, TGA, and STEM-EDS were performed in the Vanderbilt Institute of Nanoscale Science and Engineering (VINSE). Histology sections were prepared through the use of Vanderbilt's Translation Pathology Shared Resource (TPSR).

TABLE OF CONTENTS

Page

LIST OF TABLES

LIST OF FIGURES

CHAPTER 1

INTRODUCTION AND SIGNIFICANCE

1.1 Motivation

In February 2001, two research groups led by Francis Collins and Craig Venter published a nearly complete sequence of the human genome [1, 2]. Their work was the culmination of the Human Genome Project (HGP)—a 13-year coordinated effort by a group of 32 scientists in 14 countries. One striking finding from the HGP is that only 1.5% of the approximately 30,000 genes in the human genome encodes for protein [3]. This is surprising because proteins are the most common organic molecules found in cells [4]. If DNA is an instruction manual, then proteins are the building blocks of life. What then is the point of the other 98.5% of our DNA? While the purpose of much of the genome remains a mystery, between 5–10% of DNA is transcribed into non-coding RNA [5, 6]. Non-coding RNA molecules are never translated into proteins, yet they are highly abundant and serve critical functions within all cells. Mutations and imbalances in one class of regulatory non-coding RNAs, known as microRNA (miRNA), correlate with development of diseases such as cancer and cardiovascular disease [7]. Inhibition of miRNA is a potentially potent therapeutic strategy because single miRNAs are known to regulate hundreds of different disease-associated genes [8]. Consequently, there is a tremendous opportunity to develop a new class of therapeutics that can target and correct the expression of aberrant miRNA.

One promising candidate for therapeutically inhibiting miRNA is a peptide nucleic acid (PNA). PNAs are synthetic nucleic acids wherein the negatively charged sugar-phosphate backbone is replaced with charge-neutral peptide bonds [9]. Nucleobases (A, C, T, and G) are

spaced along the peptide backbone such that PNA hybridization with DNA and RNA obeys the rules of Watson-Crick base pairing [10, 11]. PNA offer several advantages over DNA- and RNA-based drugs, including greater binding affinity for target RNA molecules [12] and innate resistance to enzymatic degradation [13, 14]. These attributes make PNAs ideal candidates for application as anti-miRNA therapeutics [15].

Unfortunately, intravenously delivered PNA will exit a patient's blood stream and clear their kidneys in under 5 min [16]. This short blood circulation half-life is due to PNA's small size and neutral charge, which also prevent it from interacting with and entering into diseased cells [16]. Thus, potentially the biggest challenge in clinical translation of PNA therapies is achieving efficient biodistribution and activity in target tissue while minimizing side-effects in healthy tissue. To address this challenge, the field of material science turns to the tools of nanoscience—engineering materials at a scale one-billion times smaller than a meter to create devices for targeted delivery of the next generation of therapeutics.

1.2 Approach

This work focuses on engineering nanoparticle (NP) vectors to improve PNA delivery and anti-miRNA activity in target cells [17]. Unlike isolated PNA, NPs can be tightly engineered to control stability in blood, uptake by cells, and PNA delivery to the cellular cytoplasm where miRNA targets are located [18-21]. Specifically, NPs made from porous silicon (PSi) are engineered to improve the intracellular delivery and anti-miRNA activity of therapeutic PNA. PSi is an ideal material for drug delivery because it is biocompatible, meaning that it is not harmful to living tissue [20], and biodegradable, meaning that PSi is eventually broken down by the body into non-

toxic metabolites [22]. PSi possesses a large internal surface area for drug loading [23, 24] and can be fabricated into particles suited for intravenous drug delivery [18-20, 23, 25].

As the core of the delivery construct, porous silicon nanoparticles (PSNPs) enable accurate particle distribution in the targeted tissue before the PSNPs degrade and release their PNA payload. PSNPs also serve a critical role as a scaffold for PNA loading. Negatively charged DNA and RNA-based oligonucleotides are typically loaded into NPs by electrostatic interactions. Unmodified PNA is neutrally charged and cannot be loaded electrostatically into conventional nucleic acid delivery systems. In this work, the high internal surface area (>100 m^2 cm^{-3})[26] and polar surface chemistry of oxidized PSNPs [27] are leveraged to enable a high degree of PNA loading. Finally, the surface of the drug-loaded particles is functionalized with a polymer that enhances PSNP stability in the blood and improves the PNA delivery to its site of action in the cell cytosol.

This polymer, referred to as PEGDB, is composed of two blocks. The first block is hydrophilic poly[(ethylene glycol)] (PEG), the second consists of hydrophobic butyl methacrylate (B) and pH-responsive dimethylaminoethyl methacrylate (DMAEMA) [28]. PEGDB's amphipathic and pH-responsive nature allows it to self-assemble on the surface of PSNPs. On the outermost surface of the PEGDB/PSNP nanocomposite, PEG enhances particle colloidal stability and decreases interaction with blood serum proteins. PEG therefore increases the circulation half-life of the particles in blood. When PNA-loaded nanocomposites reach target cells they are internalized by a process called endocytosis. During endocytosis, compartments known as endosomes gradually acidify as they attempt to break down the internalized particles. The pH-responsive DB component of the nanocomposite takes advantage of this natural acidification process by disrupting endosomal membranes and triggering release of PNA into the cell cytosol. Thus, the combination of PSi and PEGDB improves the delivery and activity of PNA therapeutics.

1.3 Innovation

There are currently no clinically-approved anti-miRNA therapeutics. PNA has shown tremendous therapeutic promise in vitro, but its clinical translation is stymied by a lack of delivery technologies suited for systemic administration in vivo. This work introduces a nanocomposite proven to overcome both systemic and intracellular barriers to anti-miRNA PNA delivery. The innovative use of PSi as a PNA loading scaffold resulted in the highest reported PNA loading of any nanoparticle system to date. Furthermore, the novel combination of PSi with an endosomalytic polymer yielded a composite material with enhanced stability in the blood and improved PNA delivery to its intracellular site of action. These novel nanocomposites can be used to tailor PNA dose, blood circulation half-life, release profile, and cell-permeability. PSi nanocomposites therefore allow greater control over PNA anti-miRNA pharmacokinetics than current PNA delivery technologies. Consequently, this delivery platform may aid the clinical translation of a valuable new class of therapeutics.

1.4 Specific Aims

This works' central hypothesis is that PNA anti-miRNA activity can be improved by engineering PSNPs to increase PNA blood circulation half-life, cellular uptake, and intracellular delivery to the cytoplasm. This hypothesis will be evaluated through the completion of the following three specific aims:

Aim 1: Develop and assess strategies for loading PNA into PSi.

Three different, non-electrostatic loading strategies will be developed and evaluated according to the degree of drug loading, purity of loaded PNA sequence, and control over PNA release. The effect of loading strategy on PNA bioactivity will be investigated in vitro in Huh7 human liver cancer cells using Luciferase as a bioluminescent reporter for anti-miRNA activity.

Aim 2: Develop and assess the activity of PEGDB/PSNP nanocomposites in vitro.

A method will be developed for coating PSNPs with pH-responsive PEGDB polymers (comprised of a hydrophilic polyethylene glycol (PEG) segment and a hydrophobic, pH-responsive, endosomalytic segment). The effect of the PEGDB polymer coating on particle stability in serum, cellular uptake, intracellular trafficking, and anti-miRNA activity will be assessed in Huh7 human liver cancer cells in vitro.

Aim 3: Assess the activity of PNA-loaded PSNPs targeted against miR-122 in vivo.

MiR-122 is a well-studied, liver-specific miRNA involved in cholesterol biosynthesis and Hepatitis C viremia [29]. PNA therapeutics validated against miR-122 will be delivered systemically to mice using both uncoated PSNPs and the PEGDB/PSNP nanocomposites developed in Aim 2. The biodistribution, pharmacokinetics, and toxicity of intravenously-delivered PNA will be evaluated as a function of delivery platform. PNA anti-miRNA activity will then be evaluated by monitoring changes in the expression of miR-122, its downstream gene targets, and the concentration of plasma cholesterol in the blood.

1.5 Outline

This dissertation describes the development and validation of a nanoparticle delivery vehicle for improved delivery of PNA anti-miRNA therapeutics. Chapter 2 will review how miRNA inhibition works, how PNA anti-miRNA design compares with other relevant oligonucleotides, and how PNA delivery barriers might be overcome using PSNPs. Chapter 3 compares strategies for loading PNA into PSi and details methods for fabricating PSNPs. Chapter 4 describes the development of PEGDB/PSNP nanocomposites and evaluates their ability to overcome intracellular barriers to in vitro PNA anti-miRNA activity. Chapter 4 then evaluates the effectiveness of PEGDB/PSNP nanocomposites at overcoming systemic delivery barriers to PNA anti-miRNA activity in vivo. Finally, a summary of the major results and a discussion of the broader impacts, challenges, and future directions for this work will conclude this dissertation.

CHAPTER 2

BACKGROUND

Text partially adapted from:

Beavers KR, Nelson CE, Duvall CL. MiRNA Inhibition in Tissue Engineering and regenerative Medicine. Advanced Drug Delivery Reviews. 2015; 88: 123-137

2.1 Therapeutic miRNA inhibition

The body relies upon a complicated series of checks and balances to maintain homeostasis. Imbalances or malfunctions in this regulatory network commonly result in disease. MiRNA molecules are key players in this system of checks and balances because they regulate nearly all of the body's fundamental processes [30]. MiRNA act by preventing translation of messenger RNA (mRNA) into protein [31]. Individual miRNA are often cross-reactive with hundreds of different mRNA [8]. As a result, miRNA can orchestrate comprehensive responses by affecting a broad network of related genes.

Multiple stages during the biogenesis of miRNA represent potential points of intervention for anti-miRNA therapeutics (**Figure 2.1**). The first step in miRNA production is transcription into long primary RNA transcripts known as pri-miRNAs. The pri-miRNAs are cleaved by Drosha in the nucleus into a 70 base pair pre-miRNA hairpin intermediate. Pre-miRNAs are then exported to the cytoplasm and processed by Dicer ribonucleases into mature, double-stranded miRNA that are between 18 and 25 nucleotides in length. The mature miRNA interacts with the proteins that comprise the RNA-induced silencing complex (RISC), which separates the guide strand of the

mature miRNA from the passenger strand—retaining the guide strand to form an active RISC [32, 33]. The miRNA guide strand then binds to complementary mRNA and enables target mRNA cleavage by the RISC-associated endonuclease Argonaut2 (Ago2) (**Figure 2.1A**) [33]. As illustrated in **Figure 2.1**, anti-miRNA oligonucleotides (AMOs) molecules can be designed to inhibit either the mature miRNA in the active RISC complex or any of its precursors [34].

Potential disadvantages in targeting miRNA precursors are that precursors are relatively transient species and not all miRNAs are equally susceptible to inhibition at the level of the pre- or pri-RNA [35]. Pri-miRNAs are especially difficult targets because they require inhibitor delivery to the nucleus. Consequently, most miRNA inhibitors (including the PNA anti-miRNA therapeutics used in this work) are designed to bind to and inhibit the activity of the mature miRNA guide strand once it is loaded into the RISC (**Figure 2.1D**) [36]. However, an alternative approach to inhibiting mature miRNA activity is to use "blockmir" technology. Blockmirs are ~15mer oligonucleotides that are targeted to the mRNA instead of the miRNA; they function to target and competitively inhibit miRNA binding sites (**Figure 2.1E**) [37]. Because blockmirs target individual mRNAs, they may provide a means to reduce off-target effects and to achieve more predictable pharmacodynamics then anti-miRNA therapeutics that block all miRNA activities. This better specificity may aid clinical translation of anti-miRNA therapeutics, but it also abrogates the ability to develop therapeutics that simultaneously regulate multiple genes. Therefore, direct inhibition of mature miRNA remains the most high-impact and widely investigated strategy.

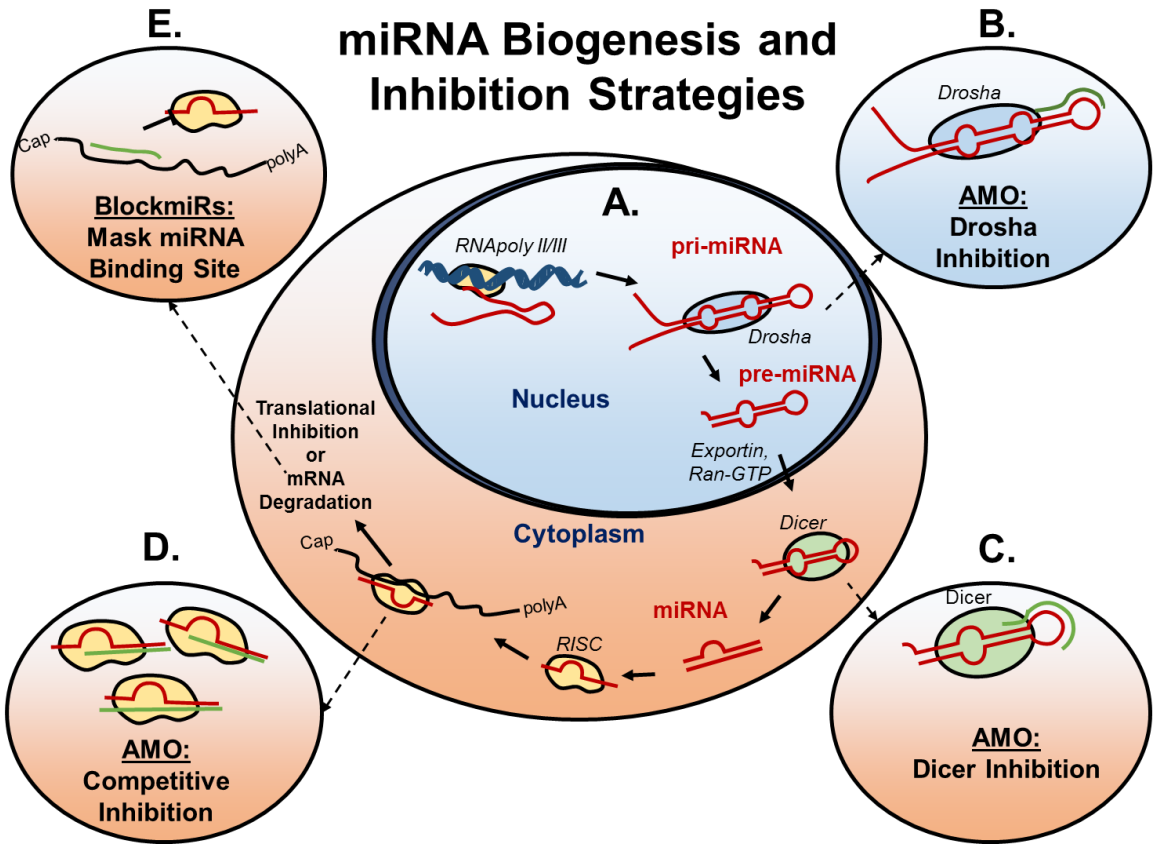

Figure 2.1. Sites of intervention for different anti-miRNA therapeutics along **A)** the miRNA biogenesis pathway. Anti-miRNA oligos (AMOs) are typically single stranded oligos that are introduced exogenously into the cell and can bind to **B)** pri-miRNA to inhibit Drosha activity or **C)** pre-miRNA to inhibit Dicer cleavage. **D)** AMOs are most commonly designed to bind to and inhibit mature miRNA. **E)** Blockmirs are oligonucleotides that block miRNA activity by specifically masking the 3' UTR of target mRNA. [Adapted from *Advanced Drug Delivery Reviews*, 88, Kelsey R. Beavers, Christopher E. Nelson, Craig L. Duvall, "MiRNA inhibition in tissue engineering and regenerative medicine", 123-127, 2014, with permission from Elsevier.]

2.2 Anti-miRNA oligonucleotides

Anti-miRNA oligonucleotides are the most prevalent class of miRNA inhibitors. There are several variants of AMOs utilized as anti-miRNA therapeutics, but they are all generally designed to be perfectly complementary to the full mature miRNA. Most AMOs bind to and sterically inhibit the binding of the RISC-loaded miRNA guide strand to target mRNAs (**Figure 2.1D**) [38]. Effective AMOs must have high specificity and strong binding affinity for target miRNA [31]. The first

AMO developed was a DNA oligo of complementary sequence and equal length to the target miRNA [39]. Later work revealed that the instability of unmodified DNA AMOs in serum severely limits effectiveness of miRNA inhibition in vivo [40]. Subsequent AMO designs have, therefore, focused on increasing AMO stability and endonuclease resistance, in addition to improving binding affinity to miRNA.

Most AMOs are single stranded nucleic acids with modifications to the backbone chemistry incorporated to improve binding and/or impart nuclease resistance. The earliest tested AMO modifications included methylation of nucleoside ribose 2' hydroxyl groups (**Figure 2.2B**). This "OMe" modification improves RNA binding affinity and contributes a modest improvement in nuclease resistance compared to unmodified sequences. However, OMe modified AMOs still suffer from relatively poor stability in serum [36]. Replacing the phosphodiester bonds in the AMO backbone with phosphorothiolate (PS) linkages is a more effective way of conferring nuclease resistance, but it also results in decreased AMO binding to target miRNA (**Figure 2.2D**) [41]. An additional modifier, N,N-diethyl-4-(4-nitronaphthalen-1-ylazo)-phenylamine, dubbed "ZEN" increases the binding affinity and nuclease resistance by enhancing steric blocking when positioned near the ends of OMe-modified RNA (**Figure 2.2E**) [38]. Antagomirs are another AMO derivative designed to improve the biostability and bioavailability of OMe oligos [42, 43]. Antagomirs possess a 3' end conjugation to cholesterol which imparts nuclease resistance [43]. As an added benefit, this hydrophobic cholesterol moiety enables antagomirs to better traverse the cell membrane and enter cells without the aid of a delivery vector. However, clinical translation of antagomirs is limited as they require relatively high doses to achieve miRNA inhibition (up to 80 mg kg^{-1} in a mouse model) [42], and have shown concerning off-target effects in vivo, as

evidenced by discrepancies in the cardiac phenotypes of animals with genetic depletions of miR-21 and miR-133a and those treated with antagomirs against miR-21 and miR-133a [42, 44-46].

The most effective, high-affinity AMO designs rely on highly-modified, synthetic oligonucleotide chemistries: locked nucleic acids (LNA), phosphorodiamidate morpholino oligonucleotides (PMOs), and PNA. LNA contain a methylene bridge between the 2'-O and 4'C of ribose to "lock" it into a configuration which is optimal for hybridization. LNA are also highly resistant to nuclease degradation (**Figure 2.2C**) [47]. Consequently, LNA-based AMOs show higher anti-miRNA activity at lower doses compared with the equivalent antagomir [48]. PMOs, another AMO derivative, substitute ribose with 6-membered morpholine rings, and phosphorodiamidates are used rather than phosphodiester bonds, making the overall molecule neutrally-charged (**Figure 2.2F**) [49]. These modifications sterically hinder nuclease binding and thus prevent enzymatic degradation of PMOs, but PMOs exhibit lower binding affinity for miRNA compared to LNA [49, 50]. In general, the AMO binding affinity listed from lowest to highest affinity follows the order: DNA<OMe oligos<PS-modified OMe oligos< ZEN-modified OMe oligos< PMO<LNA [38, 48, 49]. PNA, in comparison, have similar binding affinity and nuclease resistance to LNA [50]. This is the result of PNA's chimeric structure, in which nucleobases are spaced along a peptide backbone (**Figure 2.2G**) [51]. PNA's synthetic structure imparts both nuclease and protease resistance to PNA AMOs [15], while PNA's charge neutrality allows it to bind with high affinity and specificity to miRNA targets [12]. PNA also has the unique advantage that it can be synthesized at large scales using standard peptide synthesis protocols [52].

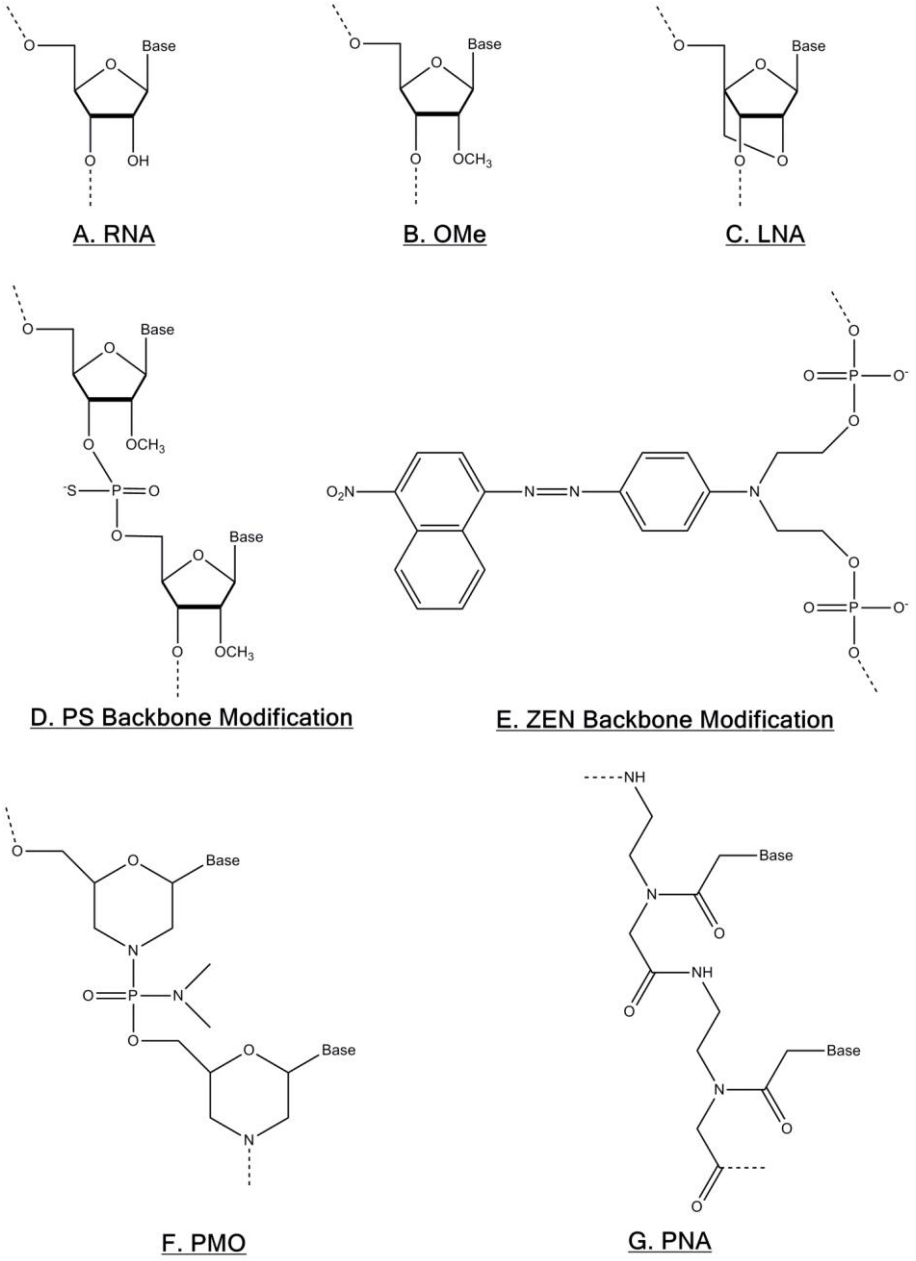

Figure 2.2. Common oligonucleotide modifications to improve anti-miRNA activity. **A)** The 2' OH of ribose RNA can be methylated to create **B)** OMe-modified RNA, or a methylene bridge can be added between the ribose 2'-O and 4'-C to create **C)** locked nucleic acid (LNA). **D)** The phosphodiester bonds in the backbone can be replaced with phosphorothiolate (PS) bonds, or a **E)** ZEN modifier can be added between phosphate groups near oligo ends. Finally, neutrally-charged, synthetic **F)** phosphorodiamidate morpholino oligonucleotide (PMO) and **G)** peptide nucleic acid (PNA) chemistries can also be designed strongly inhibit miRNA. [Adapted from *Advanced Drug Delivery Reviews*, 88, Kelsey R. Beavers, Christopher E. Nelson, Craig L. Duvall, "MiRNA inhibition in tissue engineering and regenerative medicine", 123-127, 2014, with permission from Elsevier.]

2.3 Anti-miRNA delivery considerations

To be effective, anti-miRNA therapeutics need to be efficiently distributed in the target tissue site, internalized by the target cells, and trafficked to the cell cytosol where mature miRNA and the RISC machinery are located. Basic scientists often carry out in vitro mechanistic studies utilizing non-viral anti-miRNA delivery methods and reagents (e.g., cationic lipofection reagents) that do not meet these needs and are therefore not suitable for clinical use [53-56]. In contrast, other work has focused on developing agents that improve clinical anti-miRNA delivery and to expand the therapeutic index of anti-miRNA therapeutics. Examples of these agents include dendritic polymer nanoparticles [57], amphiphillic polymer micelles [58], gold nanoparticles [59, 60], lipid nanoparticles [48, 61, 62], and cell penetrating peptides (CPPs) [48, 63]. Conveniently, many of the advances in improving biodistribution and uptake for RNA-based drugs (such as shielding with PEG to improve circulation time, or conjugation to targeting antibodies) can be adapted for delivery of most AMOs [64].

PNA by exception require additional delivery-vector design considerations due to their lack of charge. To enable electrostatic loading into carriers, or facilitate carrier-free cell uptake, PNA are often modified with charged amino acid residues such as lysine and arginine [65]. For example, modification of PNA with positively-charged lysine residues enabled effective in vivo miRNA inhibition at a 50 mg kg^{-1} PNA dose in mice [66]. Although the incorporation of positive charged moieties aids PNA intracellular delivery, it can also cause undesirable non-specific binding to DNA [67]. Minimizing these non-specific binding events is critical to preventing negative side effects of PNA therapeutics for eventual clinical application.

One strategy for reducing off-target side effects is to modify PNA such that its uptake into cells is triggered by cues in the disease environment. For example, Cheng et. al. conjugated PNA

to a pH-responsive peptide which enables targeted PNA delivery to the acidic tumor microenvironment [68]. Additionally, the peptide utilizes an environmentally-activated non-endocytic cell uptake / membrane transduction mechanism. This enabled miRNA inhibition at a 1 mg kg^{-1} dose in a mouse model of lymphoma. Conjugation of PNA to an environmentally-responsive peptide is effective at targeting tumor-associated miRNA; however, this strategy is limited to the inhibiting miRNAs in acidic microenvironments. Nanoparticles are a more versatile solution to the problem of PNA delivery.

As an alternative to chemically modifying PNA, Babar et al. demonstrated that PNA encapsulation into poly(lactic-co-glycolic acid) (PLGA) nanoparticles coated with a cell-penetrating peptide reduced the effective anti-miRNA PNA dose to 1.5 mg kg^{-1} in mice [69]. PLGA is a biocompatible and biodegradable material, but inefficient water in oil in water (W/O/W) emulsion is required for PLGA NP formation and PNA drug loading. Consequently, PLGA nanoparticles suffer from low PNA loading (0.35 wt% PNA). Low drug loading efficiency is common for PLGA nanoparticles and is considered the major hurdle limiting their clinical translation [70]. Although the PLGA study suggests that NPs can improve PNA anti-miRNA efficacy, a nanomaterial with higher drug-loading capacity is needed for clinical translation of PNA therapeutics.

2.4 Porous silicon for drug delivery

Porous silicon (PSi) is a promising biomaterial for PNA delivery [20]. Accidentally discovered at Bell Laboratories in 1956 [71], PSi is a versatile material that was spotlighted for biomedical applications in 1995 when Leigh Canham demonstrated that PSi is biodegradable and non-toxic [72]. In contrast to PLGA, PSi is an inorganic material with a large internal surface area (up to 800

m^2 g^{-1}) that can be exploited for PNA loading [73, 74]. PSi is typically fabricated using a top-down approach, whereby the crystalline Si is porosified by electrochemical anodization.

This process begins by immersing a clean, hydrogen-terminated silicon wafer in an organic solution (such as ethanol or acetonitrile) containing hydrofluoric acid (HF). The dissolution process that results in pore formation can be described by **Equation 2.1**. Under open circuit conditions, the surface of the silicon wafer is passivated by silicon hydride. When an anodic bias is applied to the wafer, an electronic hole (h^+) migrates to the surface to catalyze replacement of superficial H atoms by highly electronegative fluoride ions (F^-). The Si-F bond created under this anodic bias is highly polar, opening up Si-Si bonds to nucleophilic attack by F^- ions in the etchant solution. The progressive repetition of this process releases H_2 gas and removes Si from the surface in the form of dissolved SiF_6^{2-} species [75].

$$Si + 4HF_2^- + h^+ \rightarrow SiF_6^{2-} + 2HF + H_2 + e^- \quad \textbf{(2.1)}$$

To form pores rather than electropolish the Si surface, the applied electrical current must be kept within a range such that anodization occurs preferentially at the tips of growing pores. During pore growth, electronic holes are depleted from the area adjacent to the silicon/electrolyte interface). The width of this depletion layer is dependent on the surface curvature. Therefore, Si dissolution (pore growth) occurs only at the pore tip where the radius of curvature is largest and holes are available to participate in the dissolution reaction. As a consequence of this directional pore growth, the porosity, pore size, and pore depth can be tuned *in situ* to create complex structures such as the perforated multilayer in **Figure 2.4**. Perforated multilayer PSi can be used as a precursor material for the formation of PSNPs [76].

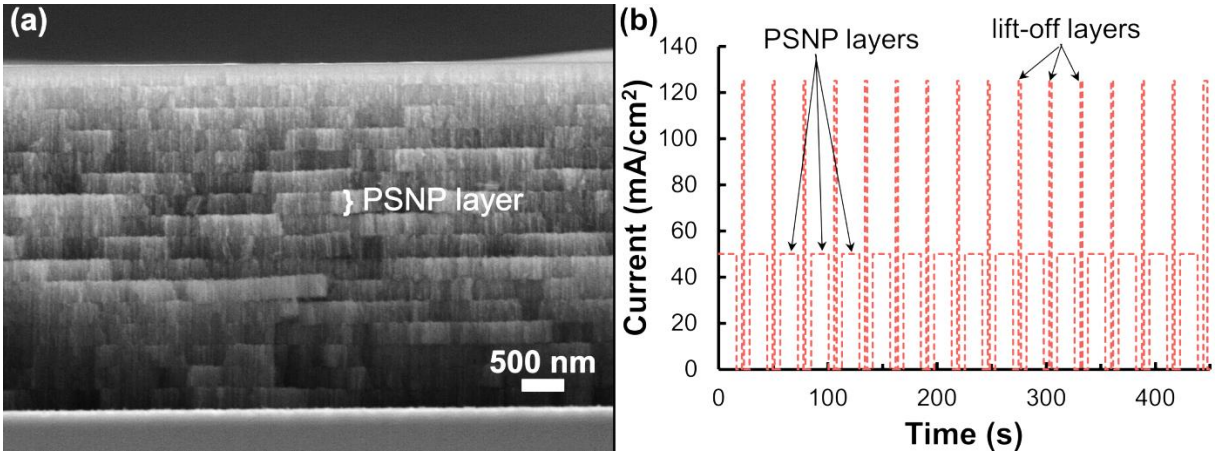

Figure 2.3. Perforated PSi multi-layer for PSNP generation. **A)** Side-profile scanning electron micrograph of a 16-layer perforated PSi film used to generate PSNPs by ultrasonic fracture. **B)** Current profile used to generate the multilayer film shown in (A). [Adapted from *Bioconjugate Chemistry*, 25 (7), Kelsey R. Beavers et. al., "In Situ Synthesis of Peptide Nucleic Acids in Porous Silicon for Drug Delivery and Biosensing", 1192-1197, 2014, with permission from the American Chemical Society.]

PSi can be fabricated into particles with controlled porosity, shape, and size by tuning parameters such as wafer type and resistivity, the applied etch current time and density, and the electrolyte composition [19, 21, 25, 76]. Due to its prevalence as an electronic material, the technologies for fabricating and processing PSNPs are rapid, scalable, and relatively inexpensive. One commonly used, high-throughput means of generating PSNPs is through mechanical fracture of perforated multilayer PSi films (either by ball-milling or ultrasonication) [23, 76, 77]. After fabrication, PSNPs can be modified by a wide range of chemistries pioneered by the microelectronics industry.

Chemical modifications such as oxidation, silanization, and hydrosilation have been used to tailor PSNPs for drug delivery applications [74]. In biological solutions, unoxidized PSNPs break down into orthosilicic acid: the non-toxic, natural bioavailable form of silicon that is easily metabolized by and excreted from the body [22, 78]. Thermal and chemical oxidation can be used to tune the half-life of PSNPs in biological solutions from the order of hours to weeks [79-81].

Following oxidation, PSNP surfaces are decorated with hydroxyl groups that can be reacted with organic compounds to assist in grafting drugs or other biofunctional compounds to the particle surface. The variety of available PSi surface modifications allows PSNPs to efficiently load many different types of drugs. Proven PSNP payloads include large hydrophilic biomolecules like short interfering RNA (siRNA) [82], small hydrophobic molecules like the anti-inflammatory drug indomethacin [83], and neutrally charged molecules like PNA [24, 84].

As a consequence of their versatility, PSNPs have emerged as drug delivery vectors in broad range of biomedical applications. The Sailor group at the University of California, San Diego pioneered the use of PSNPs for in vivo tumor targeting and imaging [85]. Ferrari and co. later developed a multistage delivery system (MDS) consisting of PSi microparticles loaded with smaller nanoparticles for the treatment of cancer [21]. The shape and size PSi particles were engineered to improve MDS uptake in tumors where the subsequent release of nanoparticles delivers therapeutics to cancer cells [19]. In addition to tumor delivery, other groups have shown PSNPs improve drug delivery to numerous organs. These include the eye, liver, brain, and heart for the treatment diseases such as of proliferative vitreoretinopathy, hyperlipidemia, brain injury, and heart failure [24, 82, 86, 87]. Taken together these studies confirm that PSNPs are versatile, biocompatible NPs with high drug loading capacity and a demonstrated ability to overcome systemic delivery barriers in vivo. PSNPs are therefore poised to overcome the main challenges associated with PNA therapeutic delivery.

CHAPTER 3

PSNP DESIGN AND DEVELOPMENT OF PNA LOADING STRATEGIES

Text partially adapted from:

Beavers KR, Mares JW, Swartz CM, Zhao Y, Weiss SM, Duvall CL. In Situ Synthesis of Peptide Nucleic Acids in Porous Silicon for Drug Delivery and Biosensing. Bioconjugate Chemistry. 2014; 25 (7): 1192-1197

3.1 Introduction

The advantageous properties of PSi (reviewed in section 2.4) have motivated a large body of research into PSi technologies for drug delivery. However, prior to the publication of this work in 2014 [84], the only reported method of PNA attachment to PSi was nonspecific adsorption for nucleic acid biosensing [88]. There were no published studies for delivery of PNA-based therapeutics using PSNPs. Prior work seeking to improve PSi functionalization with biomolecules established methods for synthesizing peptides directly from PSi [89-91]. In addition, our group has shown that base-by-base synthesis of DNA directly within PSi films (referred to as *in situ* synthesis) significantly increases DNA loading relative to attachment of pre-synthesized oligos [92]. Building upon these results, this chapter describes the first use of PSi as a platform for the automated synthesis and label-free characterization of PNA. *In situ* PNA synthesis is compared against two other, non-electrostatic strategies for loading a PNA anti-miRNA therapeutic into oxidized PSi. It is shown that *in situ* PNA synthesis increases PNA loading relative to conjugation of the pre-synthesized molecule. The advantage of this approach is demonstrated for intracellular

delivery of a well-characterized anti-miR122 PNA [93] which targets a liver-specific miRNA whose suppression has been linked to treatment of hyperlipidemia and hepatitis C viremia [94].

3.2 Materials and methods

3.2.1 PSi and PSNP fabrication and characterization. PSi films are the precursor material for PSNPs. Additionally, PSi films are advantageous substrates for solid-state PNA synthesis (discussed in section 3.2.2) and for evaluation of PNA loading efficiency (discussed in section 3.2.6). This is because reflectometry can non-destructively quantify changes in pore content by measuring changes in PSi film optical thickness. Optical thickness, defined below in **Equation 3.1**, is the product of the effective refractive index of PSi (n_{eff}) and the thickness of the PSi film (L). Effective medium theory states that n_{eff} is a function of both the refractive index of the silicon matrix and that of the pore filling material [95]. Consequently, changes in optical thickness are directly correlated with changes in PNA loading.

$$Optical\ Thickness = 2n_{eff}L \qquad \textbf{(Equation 3.1)}$$

PSi films used for optical evaluation of PNA loading efficiency were etched from p-type Si (0.01Ω-cm) using 15% hydrofluoric acid in ethanol to form 10 μm thick single layers (70% porosity, 30 nm average pore diameter). Multilayer films used for PSNP generation were fabricated by multiple repetitions of two anodization steps: 50 mA/cm^2 for 8 s to yield "particle" layers with 70% porosity, and 60 mA/cm^2 for 2 s to form mechanically fragile "lift-off" layers (**Figure 2.3**). All porous silicon films were thermally oxidized at 800°C for 30 min in ambient air.

To generate PSNPs, multilayer films were ultrasonicated in isopropanol (IPA) for 2 h after completion of *in situ* PNA synthesis. Deionized water was used to reduce the concentration of IPA in the sonicated particle suspension to 65%. PSNPs were then filtered through a 2.6 μm syringe filter and immediately isolated using a 10 kDa molecular weight cutoff centrifugal filter to separate free PNA from PNA-conjugated PSNPs. Free PNA was collected from the filtrate, and PNA-functionalized particles (PNA-PSNPs) were collected from the concentrate. Aliquots of both the free PNA and PNA-PSNPs solutions were taken for analysis by UV-Vis spectroscopy and nanoparticle tracking analysis (NTA) [96]. To quantify the amount of PNA conjugated to PSNPs, a known concentration of PNA-PSNPs was dissolved in 5x PBS overnight, and PNA concentration was determined by measuring PNA absorbance at 260 nm.

3.2.2 In situ PNA synthesis. Oxidized PSi films were functionalized with 3-aminopropyltriethoxysilane (APTES) by drop-casting a solution of 1% APTES in anhydrous toluene onto the porous surface and incubating the sample at room temperature for 10 min. Following APTES attachment, films were rinsed 3x with ethanol to remove excess silane. The silanized films were thermally annealed at 150ºC for 15 min to promote stable APTES monolayer formation, and the films were then soaked at room temperature in deionized water for 3 h to remove any unwanted silane multilayers.

In situ synthesis of anti-miR122 PNA (NH_2-ACA AAC ACC ATT GTC ACA CTC CA-COOH) was conducted directly on APTES-functionalized PSi within a custom reaction vessel (**Figure 3.1**). A schematic of the synthesis process is presented in **Figure 3.2**. After synthesis, Bhoc protecting groups were removed from nucleobases by 10 min incubation with 5% (v/v)

anisole in trifluoroacetic acid (TFA), followed by 5 min washing with dichloromethane (DCM), 2x, rinsing with methanol, 3x, drying under nitrogen gas, and storage in a vacuum desiccator.

To investigate whether pore widening improves monomer coupling efficiency for longer oligos, changes in optical thickness were monitored during synthesis of anti-miR122 PNA from a KOH-exposed PSi film (**Figure 3.6**). Following electrochemical etching, PSi films were exposed to a 9 mM pore-widening solution of KOH in ethanol at room temperature for 20 min. Pore size distributions were quantified from SEM micrographs using ImageJ analysis software.

Figure 3.1. Custom reaction vessel for the *in situ* synthesis of PNA on PSi films.

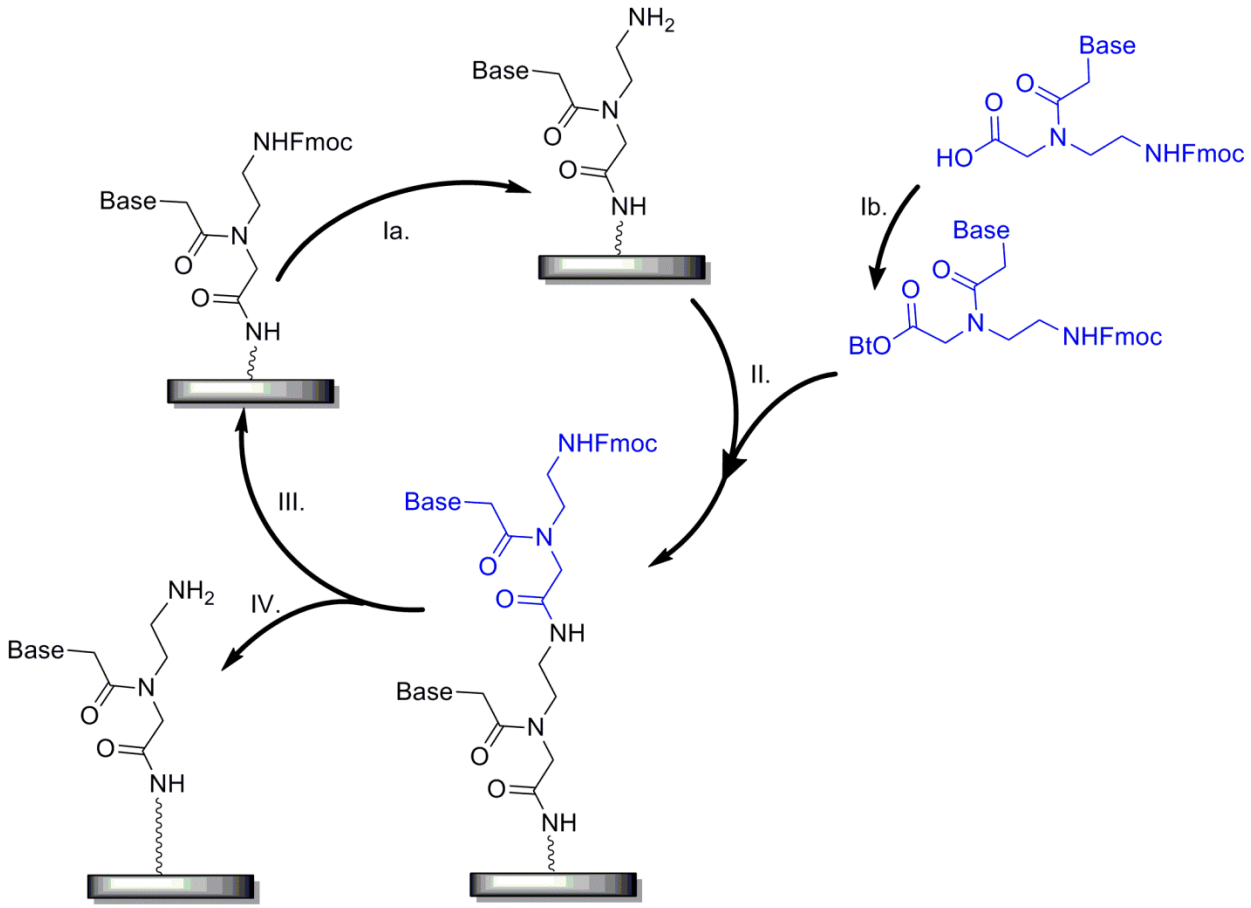

Figure 3.2. *In situ* synthesis of PNA from a PSi film solid support (shaded box). Each base addition requires **(Ia)** Fmoc deprotection of growing PNA chains on the PSi surface, 2x, **(Ib)** activation of PNA monomer C-termini and **(II)** coupling of preactivated monomers to growing PNA oligos, 3x, followed by either **(III)** automated repetition of the cycle to further elongate PNA oligos, or **(IV)** final deprotection of N-termini and exit from the cycle. [Adapted from *Bioconjugate Chemistry*, 25 (7), Kelsey R. Beavers et. al., "In Situ Synthesis of Peptide Nucleic Acids in Porous Silicon for Drug Delivery and Biosensing", 1192-1197, 2014, with permission from the American Chemical Society.]

3.2.3 Pre-synthesized PNA conjugation. Pre-synthesized cys-PNA was conjugated to APTES-functionalized PSi via an amine-to-sulfhydryl heterobifunctional crosslinker, *N*-succinimidyl 3-(2-pyridyldithio) propionate (SPDP) (**Figure 3.3**). SPDP was first reacted with the freshly-silanized surface in ethanol at room temperature for 1 h using a 20x molar excess of SPDP. The

number of successfully attached SPDP groups was quantified with a control sample by reducing conjugated SPDP with TCEP and measuring absorbance of released pyridine-2-thione at 343 nm.

Prior to attachment, pre-synthesized cys-PNA dissolved in deionized water was reduced on immobilized TCEP resin. Immediately afterwards, the SPDP-functionalized PSi film was incubated with the reduced cys-PNA at a PNA:SPDP molar ratio of 4:1. The reaction was allowed to proceed at room temperature on a shaker for 2 h, after which the reaction supernatant was removed and retained for subsequent characterization. The PNA-conjugated film was rinsed 3x with water, 2x with ethanol and 2x with methanol, then dried with nitrogen gas and stored in a desiccator under vacuum. Reaction efficiency was quantified by comparing moles of pyrdine-2-thione released from PNA attachment to moles of SPDP conjugated to the surface.

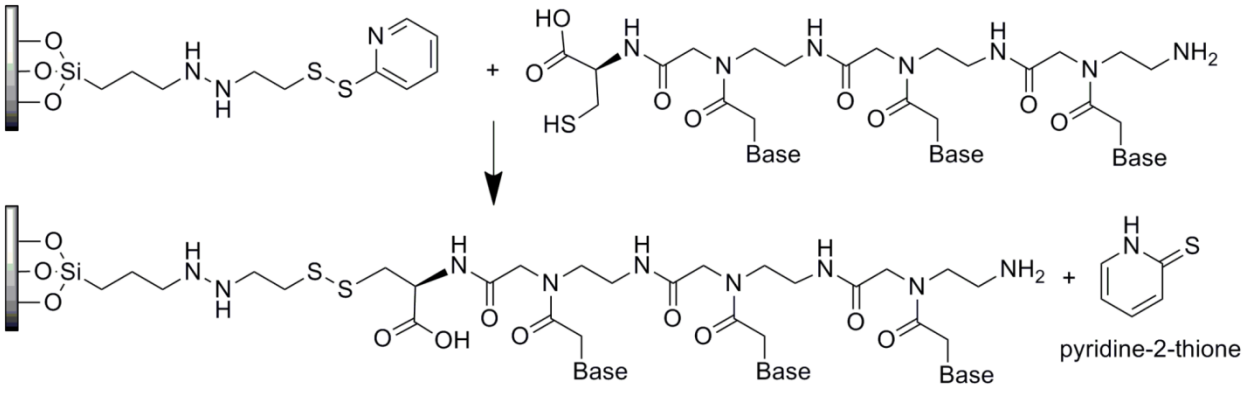

Figure 3.3. Direct conjugation of pre-synthesized PNA to a PSi film (shaded box). [Adapted from *Bioconjugate Chemistry*, 25 (7), Kelsey R. Beavers et. al., "In Situ Synthesis of Peptide Nucleic Acids in Porous Silicon for Drug Delivery and Biosensing", 1192-1197, 2014, with permission from the American Chemical Society.]

3.2.4 Physical PNA adsorption. Physical adsorption of PNA (**Figure 3.4**) was accomplished using by incubating oxidized PSi films with PNA in water at an equivalent concentration to that used to

conjugate pre-synthesized PNA to PSi (1 µmole PNA/2.6 mg PSi) for 2 hours at room temperature. Following incubation, films were washed 3x with water, 2x with ethanol and 2x with methanol. In these films, PNA are either adsorbed to the PSi internal surface, or absorbed within the open pore volume.

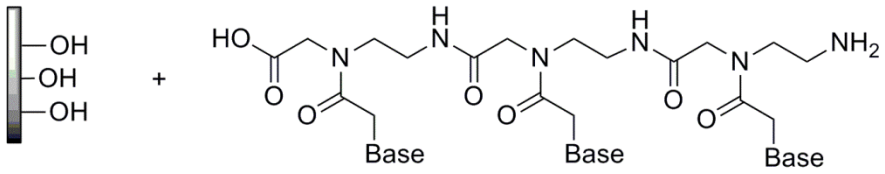

Figure 3.4. Physical adsorption of pre-synthesized PNA to an oxidized PSi film (shaded box). [Adapted from *Bioconjugate Chemistry*, 25 (7), Kelsey R. Beavers et. al., "In Situ Synthesis of Peptide Nucleic Acids in Porous Silicon for Drug Delivery and Biosensing", 1192-1197, 2014, with permission from the American Chemical Society.]

3.2.5 Mass spectrometry. Matrix assisted laser desorption-ionization mass spectrometry (MALDI-MS) was utilized to confirm the expected mass of the synthesized PNA [97]. MALDI spectra were acquired using a Voyager DE-STR mass spectrometer in linear, positive mode with an external Nd:YAG laser ionization source (frequency tripled, 355 nm). The matrix employed for the MALDI measurement consisted of either 2.5 mg of 3,5-dimethoxy-4-hydroxycinnamic acid (sinapinic acid) or 1 mg of α-cyano-4-hydroxycinnamic acid (CHCA), dissolved into 100 µL of a 7:3 v/v solution of acetonitrile:water, with 2 µL of 10% TFA. To liberate PNA from PSi, an area of PNA-loaded porous silicon film (approximately 6 mm^2) was scraped into 40 µL of deionized water, sonicated for several minutes and allowed to dissolve for approximately 1 h. This suspension was then added in equal volume to the matrix solution and agitated. The matrix was drop-cast onto a conventional stainless steel MALDI plate and dried prior to measurement.

3.2.6 In vitro PNA loading and release. PNA loading studies were performed by monitoring the change in optical thickness of dry PSi films before and after PNA loading. Optical thickness was quantified as the peak in the Fourier transform of the PSi reflectivity spectrum, taken with a spectrophotometer (Ocean Optics, Dunedin, FL, USA). Release studies were performed by incubating PNA-loaded PSi films in 1x PBS at 37ºC. Releasate was collected at pre-determined times and analyzed for PNA concentration by monitoring the absorbance of the nucleic acid at 260 nm. Collected releasate was replaced with fresh PBS to maintain infinite sink conditions over the course of the study.

3.2.7 Cell culture and biological assays. All Huh7 human hepatic carcinoma cells were maintained in Dubelco's modified eagle medium (DMEM) containing 10% fetal bovine serum (FBS), 2% penicillin-streptomycin antibiotics, and 2μg mL^{-1} ciprofloxacin at 37ºC/5% CO_2. To enable visualization of intracellular PNA delivery, N-termini of free and PSi-bound PNA were labeled with NHS-Alexa-488 at a molar ratio of 1:2 (Alexa:PNA). Excess NHS-Alexa and reaction byproducts were removed by sequential centrifugal filtration (3 kDa cutoff centrifugal filters) and resuspension in deionized water, 4x. Alexa-labeled free PNA and PNA-PSNPs were then lyophilized for storage until used.

Cells were seeded onto 8-well chamber slides (Thermo Fisher Scientific Inc., Waltham, MA) at a density of 12,500 cells/well and incubated at 37ºC for 8 h. Cells were then treated for either 1 or 24 h with free PNA or PNA-PSNPs at a 2 μM dose of PNA (~3.7 μg mL^{-1} PSNPs for PNA-PSNP treatments). Subsequently, the cells were washed with PBS and stained for 5 min with Hoechst nuclear dye prior to imaging with confocal microscopy (Zeiss LSM 710Meta, Oberkochen, Germany).

PSNP cytotoxicity was determined using a lactate dehydrogenase CytoTox-ONE™ homogenous membrane activity assay (Promega Corporation, Madison, WI). Huh7-psiCHECK-miR122[98] cells were seeded at 6,000 cells per well in black, clear-bottom, 96-well plates (BD Falcon, San Jose, CA) and incubated at 37ºC for 8 h. Cells were then treated with free PNA, empty PSNPs, or PNA-PSNPs at a 2 μM dose of PNA (~3.7 μg mL^{-1} PSNPs for PSNP and PNA-PSNP treatments) in DMEM containing 1% FBS for 24 h at 37ºC/5% CO_2. Note that all PSNPs in this study were fabricated from pore-widened PSi. After 24 h, the cells were washed with PBS and the media was replaced with DMEM containing 10% FBS, 2% penicillin-streptomycin, and 2 μg mL^{-1} ciprofloxacin. Cells treated with a miR-122 antagomir (AMO) (2′-OMe PS modified oligonucleotide 5′ ACAAACACCAUUGUCACACUCCA 3′; IDT DNA)[40, 98] were transfected using Fugene 6 (3 μL reagent: 1 μg AMO) (Promega) in Opti-Mem media. Cells treated with AMO were incubated at 37 °C for 4 h followed by the replacement of transfection media with standard DMEM growth media. The cell viability was determined after 44 h after treatment according to the manufacturer's proliferation assay protocol.

Luciferase anti-miR122 activity was evaluated in Huh7 cells modified to increase the expression of *Renilla* Luciferase in response to miR-122 inhibition. These Huh7-psiCHECK-miR122[98] cells were seeded at 6,000 cells per well in black, clear-bottom, 96-well plates (BD Falcon, San Jose, CA) and incubated at 37ºC for 8 h. Cells were then treated with free PNA, empty PSNPs, or PNA-PSNPs at a 2 μM dose of PNA (~3.7 μg mL^{-1} PSNPs for PSNP and PNA-PSNP treatments) in DMEM containing 1% FBS for 24 h at 37ºC/5% CO_2. Note that the PSNPs and PNA-PSNPs in this study were fabricated from pore-widened PSi. After 24 h, the cells were washed with PBS and the media was replaced with DMEM containing 10% FBS, 2% penicillin-streptomycin, and 2 μg mL^{-1} ciprofloxacin. As a positive control, an optimized AMO (2′-OMe PS

modified oligonucleotide 5′ ACAAACACCAUUGUCACACUCCA 3′; IDT DNA)[40, 98] was transfected using Fugene 6 (3µL reagent: 1 µg AMO) (Promega) in Opti-Mem media. Cells treated with AMO were incubated at 37 °C for 4 h followed by the replacement of transfection media with standard growth media. Luciferase activity was measured based on bioluminescence using an in vivo imaging system (IVIS; Perkin Elmer, Waltham, MA) after addition of luciferase substrate.

3.3 Results and discussion

In situ PNA synthesis was characterized by reflectometry and matrix assisted laser desorption-ionization mass spectrometry (MALDI-MS) (**Figure 3.5**). Increases in optical thickness are directly proportional to the amount of monomer coupled to growing PNA oligos within the PSi film [99]. Addition of the first 9 bases resulted in a stepwise increase in optical thickness, while the change in optical thickness was increasingly non-linear for the addition of nucleobases 10-23 (**Figure 3.5A)**.

To verify synthesis of the desired PNA sequence, *in situ* synthesized PNA was analyzed by mass spectrometry at two critical points during synthesis: after completion of the 9-mer miRNA seed-targeting sequence and after the full 23-mer anti-miRNA (**Figure 3.5B**). The seed-targeting sequence of therapeutic PNA is the most important miRNA-binding motif [93], whereas the full 23-mer sequence improves PNA target specificity and anti-miRNA activity [93]. MALDI spectra of the 9-mer seed-targeting sequence contained a single peak corresponding to the expected molecular weight of the APTES-conjugated PNA, 2485 Da, and two additional, closely-spaced peaks corresponding to Na+ and K+ adducts were resolved at 2507 Da and 2523 Da, respectively. MALDI spectra of the full 23-mer PNA revealed an intense peak at the expected m/z for the full

PNA oligo, 6243 Da, as well as a series of less intense peaks grouped at molecular weights corresponding to PNA sequences that were truncated during synthesis.

It is postulated that steric crowding of the growing PNA oligos within nano-sized pores causes the partial truncation seen during *in situ* synthesis [100]. The molecular length of APTES is approximately 8 Å [101], and each PNA base extends a growing oligo by approximately 3.5 Å [102]. Thus, the full, 23-mer PNA is estimated to be 8.9 nm in length. Electrochemical porosification of Si produces a Gaussian-like distribution of pore sizes, so while the average pore diameter of PSi films in this study is 30 nm, it is estimated that approximately 40% of the pores are between 10 and 25 nm in diameter [103]. To investigate whether the yield of longer oligos can be improved by increasing the minimum pore size, anti-miR122 PNA was synthesized from a PSi film that was first exposed to a pore-widening solution of potassium hydroxide (KOH) in ethanol at room temperature for 20 min (**Figure 3.6**). Pore widening increased the average pore diameter by 5 nm and decreased the number of pores with diameter less than 25 nm by ~20%, resulting in increased shifts in optical thickness during *in situ* synthesis (**Figure 3.6**). These data suggest that longer oligos can be more efficiently synthesized within a porous silicon matrix by increasing the average pore size. Although it was outside the scope of our testing, it may also be beneficial to utilize a fabrication method that yields more homogenous pores. Since pore widening improved synthesis of the 23-mer anti-miR122, it was implemented for in vitro functional studies, i.e. cytotoxicity and bioactivity assays (all other studies were done with non-pore-widened substrates). Overall, these results, combined with subsequent experimental readouts, are a promising demonstration of successful synthesis of functional 23-mer PNA from PSi, with highly efficient growth of the vital anti-miR122 PNA seed sequence.

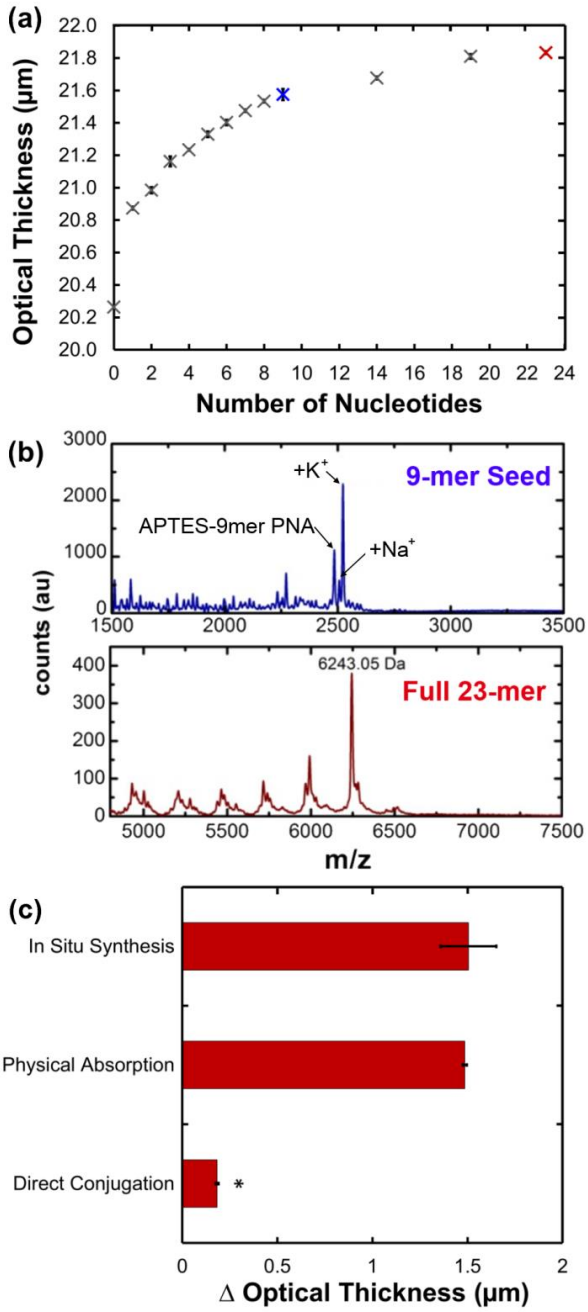

Figure 3.5. Characterization of *in situ* PNA synthesis and comparison of PNA loading methods. **A)** Non-destructive optical characterization of *in situ* synthesis of 23-mer anti-miR122 PNA using reflectometry and Fourier transform analysis to determine the optical thickness of the loaded PSi film. **B)** MALDI-TOF mass spectrometry of *in situ* synthesized 9-mer miRNA seed targeting sequence (top) and the full 23-mer PNA (bottom). **C)** Comparison of the PNA loading capacity achieved using *in situ* synthesis, physical adsorption, and direct conjugation of a 23-mer PNA to PSi. Loading was calculated based on increase in optical thickness due to the addition of PNA to the PSi surface. (* P<0.0001) [Adapted from *Bioconjugate Chemistry*, 25 (7), Kelsey R. Beavers et. al., "In Situ Synthesis of Peptide Nucleic Acids in Porous Silicon for Drug Delivery and Biosensing", 1192-1197, 2014, with permission from the American Chemical Society.]

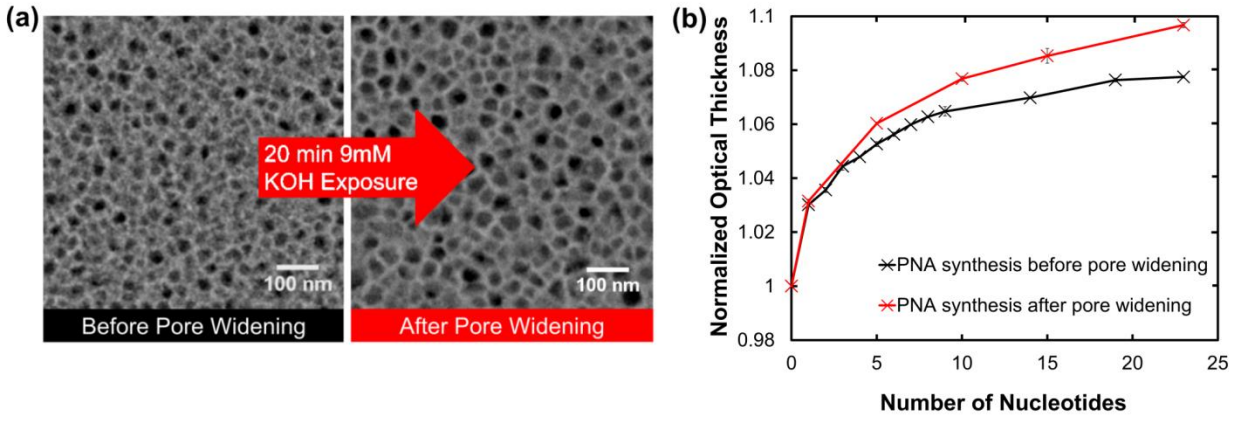

Figure 3.6. Pore widening improves in situ PNA synthesis. **A)** Top-view of PSi films before and after KOH pore-widening (SEM; scale bars=100nm). **B)** Characterization of optical thickness profile during PNA synthesis to illustrate changes in monomer coupling efficiency and yield of longer oligos following pore widening. Results are normalized to the optical thickness of each film's corresponding optical thickness following APTES functionalization. [Adapted from *Bioconjugate Chemistry*, 25 (7), Kelsey R. Beavers et. al., "In Situ Synthesis of Peptide Nucleic Acids in Porous Silicon for Drug Delivery and Biosensing", 1192-1197, 2014, with permission from the American Chemical Society.]

Optical thickness measurements were also used to determine the amount of anti-miR122 PNA loaded within PSi through *in situ* synthesis compared to standard methods of physical adsorption and conjugation of pre-synthesized PNA (**Figure 3.5C**). Consistent with our previous studies of DNA conjugation to PSi [92], PNA loading from *in situ* synthesis was 8-fold greater than the amount of PNA loading achieved from conjugation to a PSi surface. This corresponds to a yield of 8.6×10^{-4} moles PNA per g PSi, or 5.3 g PNA per g PSi for anti-miR122 synthesized *in situ* in non-pore widened PSi, quantified by measuring the absorbance at 260 nm of PNA released after dissolution of the PSi matrix. It is postulated that during PNA loading by direct conjugation, PNA preferentially attaches nearer to the pore openings at the film surface, thereby restricting access of PNA deeper into the pores. Interestingly, there was no significant difference in the loading efficiency of *in situ* synthesis and physical adsorption within the pores. It is hypothesized

that, in the case of nonspecific PNA loading by adsorption, lack of PNA covalent binding allows PNA to freely diffuse further into the pores and achieve a level of loading similar to *in situ* synthesis. Although nonspecific adsorption yielded a similar level of loading, we later demonstrate in **Figure 3.7** that the covalent attachment achieved from *in situ* synthesis provides more sustained release in the context of therapeutic PNA delivery.

To evaluate PNA therapeutic delivery potential, the in vitro PNA temporal release profile of *in situ* synthesized PNA from PSi films was compared to that of physically adsorbed PNA (**Figure 3.7A**). Release of PNA synthesized *in situ* was significantly ($p<0.005$) less than adsorbed PNA at every time point within the first 24 h. Overall, the PNA synthesized *in situ* showed reduced initial burst and more sustained release profiles. It is anticipated that hydrolytic degradation of the PSi matrix is the primary mechanism of PNA release because *in situ* synthesized PNA are covalently attached to pore walls. *In situ* synthesis therefore provides more controlled PNA delivery when compared to physical adsorption [91, 104]. Mass spectra in **Figure 3.5B** provide support for a surface-degradation PNA release mechanism because the molecular weight of PNA released from *in situ* films corresponds to APTES-conjugated PNA.

PNA anti-miRNA activity is dependent upon delivery into the cytoplasm where active micro-RNA is located [93]. To demonstrate the application of *in situ* PNA synthesis for drug delivery, anti-miR122-loaded multilayer PSi films were ultrasonically fractured to produce PNA-functionalized PSNPs. The resultant PSNP mean size (236 nm) and size distribution were determined by Nanoparticle Tracking Analysis (NTA) and confirmed by scanning electron microscopy (SEM) (**Figure 3.7B**).

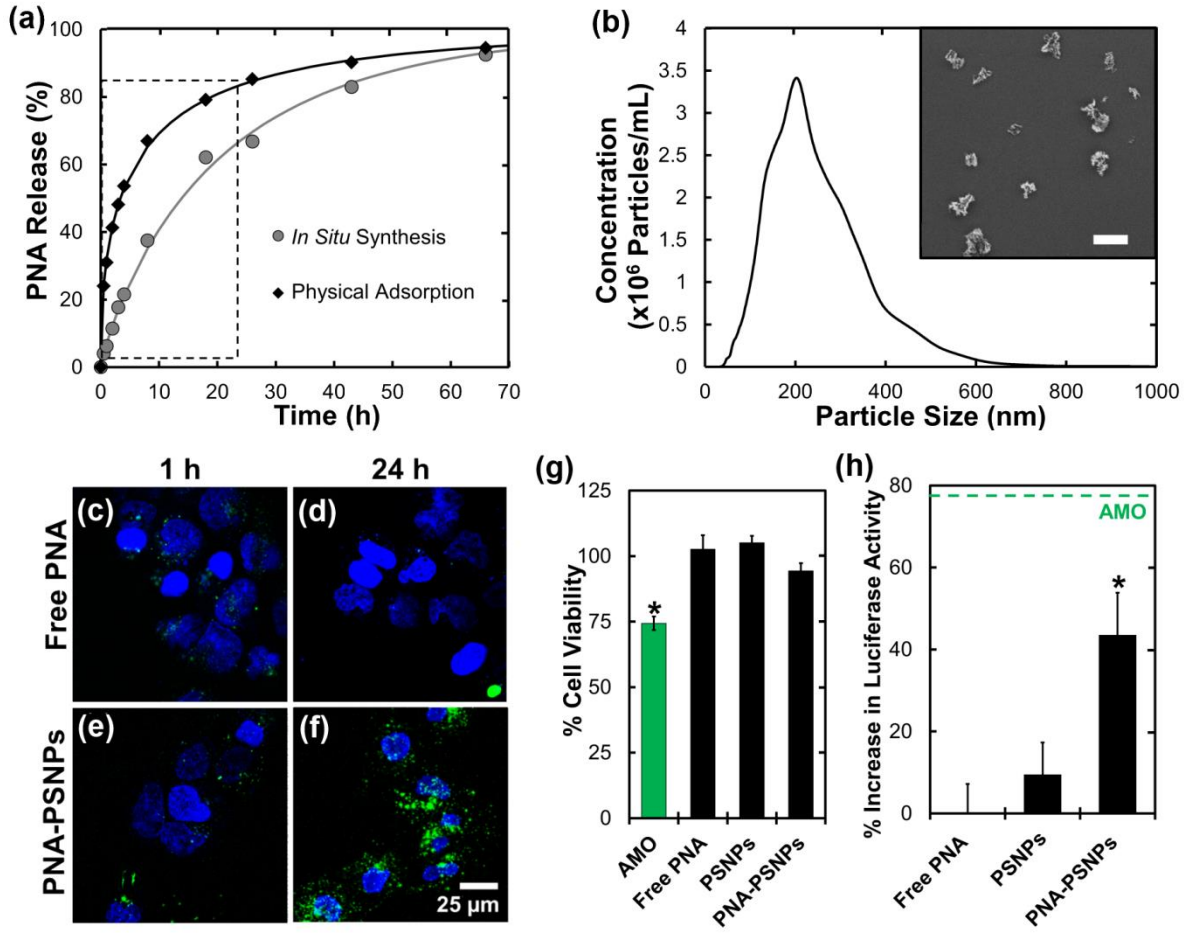

Figure 3.7. In vitro characterization of PNA-PSNP morphology and bioactivity A**)** Cumulative release of physically-adsorbed PNA and *in situ* synthesized PNA in PBS at 37°C. Release of *in situ* synthesized PNA was significantly lower ($p<0.005$) for time points within the boxed region. **B)** PNA-PSNP size distribution characterized by NTA. Inset: Representative SEM image demonstrating PSNP size and morphology (scale bar=400nm). **C-F)** Confocal micrographs of Huh7 cells incubated for either 1 or 24 h with **(C and D)** free PNA, or **(E and F)** PNA-PSNPs at a 2 µM dose of anti-miR122 PNA (3.7 µg mL^{-1} PSNPs for PNA-PSNP treatments). Labels: Hoechst nuclear dye (blue), Alexa-488 labeled PNA (green). **G)** PSNPs had no significant effect on Huh7 cell viability relative to untreated negative control samples, in contrast to a 2'OMe-modified AMO delivered with Fugene 6 ($p<0.05$). **H)** Anti-miR122 activity indicated by luciferase activity in Huh7-psiCHECK-miR122 cells 44 h after treatment with free PNA, empty PSNPs, or PNA-PSNPs (2 µM dose of anti-miR122 PNA, 3.7 µg mL^{-1} PSNPs). Results are normalized to cell number and expressed relative to luciferase activity in Huh7-psiCHECK-miR122 control cells without treatment. Dashed green line indicates anti-miR122 activity 44 h after treatment with 2 µM of an optimized anti-miR122 AMO delivered via the Fugene 6 commercial transfection reagent [40]. [Adapted from *Bioconjugate Chemistry*, 25 (7), Kelsey R. Beavers et. al., "In Situ Synthesis of Peptide Nucleic Acids in Porous Silicon for Drug Delivery and Biosensing", 1192-1197, 2014, with permission from the American Chemical Society.]

Huh7 human hepatic carcinoma cells were selected for evaluation of PNA-PSNP cellular uptake, cytotoxicity, and anti-miRNA activities because they express elevated levels of miR122. Huh7 cells therefore provide a good platform for testing anti-miR122 therapies [93, 98]. Intracellular delivery of a 2 μM dose of fluorescently-labeled free or *in situ* synthesized PSNP anti-miR122 PNA was evaluated by confocal microscopy (**Figure 3.7 C-F)**. At each treatment time, cells treated with PNA-PSNPs showed greater intracellular delivery of PNA relative to those treated with free PNA. Additionally, a lactate dehydrogenase enzymatic assay was used to compare the cytotoxicity of PNA-PNSPs to that of a 2'OMe-modified anti-miRNA oligonucleotide (AMO) delivered by the commercial transfection reagent, Fugene 6 (Promega) (**Figure 3.7G**). Consistent with previous studies on the cytotoxicity of thermally-oxidized PSi nanoparticles [105], no reduction in cell viability was observed for the PSNP concentration investigated in this study (2 μM PNA, 3.7 μg mL^{-1}), whereas AMO treatment led to a 25% decrease in cell viability at an equivalent dose.

Finally, Huh7 cells stably transfected with a psiCHECK-miR122 *Renilla* luciferase reporter for endogenous miR122 activity [98] were used to determine the anti-miRNA activity of PNA *in situ* synthesized on pore-widened PSi prior to ultrasonic particle formation (**Figure 3.7H**). In this reporter cell line, luciferase is translated upon inhibition of miR122. PSNP delivery of a 2 μM dose of *in situ* synthesized anti-miR122 PNA triggered a significant, 44% increase in luciferase activity at 44 hours after treatment, while treatment with an equivalent dose of free PNA or empty PSNPs had no significant effect relative to untreated controls. These results provide evidence that PSNPs improve the intracellular delivery and bioactivity of therapeutic PNA without the need for fusion with cell-penetrating peptides or use of cytotoxic transfection reagents, such as that used to deliver the AMO control in this study.

3.4 Conclusion

A new method for automated PNA synthesis from PSi has been developed and applied for anti-miRNA drug delivery. The optical properties of nano-structured PSi were exploited to non-destructively monitor synthesis progression with single-base resolution. *In situ* synthesis addresses the need for efficient, covalent conjugation of PNA to PSi—demonstrated by 8-fold greater PNA loading when compared to covalent attachment of pre-synthesized PNA to the surface via a cross-linker. I*n situ* synthesis is equally efficient as physical adsorption at loading PNA into PSi, and the covalent means of attachment enabled greater control of PNA release. However, physical adsorption is a promising alternative method for drug loading provided that the carrier incorporates a secondary means to minimize PNA burst release (such as the polymer coating introduced in Chapter 4). Anti-miR122 PNA-loaded PSi nanoparticles were biocompatible and increased the intracellular delivery and bioactivity of therapeutic PNA. Taken together, these studies demonstrate the utility of PSNPs for developing improved systems for controlled intracellular delivery of PNA therapeutics.

CHAPTER 4

DEVELOPMENT OF A PSNP NANOCOMPOSITE TO IMPROVE PNA THERAPEUTIC ACTIVITY IN VIVO

Text adapted from:

Beavers KR, Werfel TA, Shen T, Kavanaugh TE, Kilchrist KV, Mates JW, Fain JS, Wiese CB, Vickers KC, Weiss SM, Duvall CL. Porous Silicon and Polymer Nanocomposites for Delivery of Peptide Nucleic Acids as anti-microRNA Therapies. Advanced Materials. 2016.

4.1 Introduction

As discussed in Chapter 2, inhibition of disease-associated miRNA is a potentially potent therapeutic strategy because a single miRNA can control the expression of hundreds of different genes [106]. PNA have been successfully delivered in vitro using approaches such as fusion with cell penetrating peptides or lipophilic moieties [107], but the clinical translation of PNA anti-miRNA therapeutics is limited by physiologic delivery barriers. These barriers include poor cellular uptake, lack of endosomal escape, and rapid clearance following intravenous delivery (<5 min blood circulation half-life) [16]. While the neutrally-charged PNA backbone can provide a functional advantage, it obviates the use of conventional nucleic acid delivery strategies that rely on charge, such as formulation with cationic polymers and lipids to form nanomedicines. To overcome these delivery barriers and formulation challenges, we have developed polymer/porous silicon nanocomposites with high cargo loading capacity independent of electrostatics, stability in

the blood based on surface PEGylation, and endosomal escape functionality to facilitate PNA delivery to the cytoplasm where miRNA targets are located [108].

Chapter 3 demonstrated that packaging PNA into "naked" porous silicon nanoparticles (PSNPs) improves the cellular uptake and therapeutic activity of PNA in vitro [84]. However, after internalization, porous silicon cannot efficiently trigger release of PNA from endo-lysosomal vesicles into the cytoplasm [109], and we have observed that PSNPs are not colloidally stable at high concentrations in saline solutions amenable to intravenous administration. One PSNP modification strategy to enable endosomal escape, developed by the Santos group, is to covalently attach a zwitterionic copolymer of polyethyleneimine (PEI) and poly(methyl vinyl ether-co-maleic acid) (PMVE-MA) to the porous silicon surface [109]. PEI, which is debated to mediate endosome escape via a proton sponge mechanism [110, 111], was shown to improve endosomal escape and therapeutic activity of the small molecule drug methotrexate in these studies (though not larger biologics). The PMVE-MA-based particles have a highly negative zeta potential (-31.7 ±1.7mV) which is associated with poor in vivo pharmacokinetics relative to surface charge neutral nanoparticles [112]. Furthermore, PMVE-MA activates the innate immune system through both toll like receptor and complement activation pathways and thus is not an ideal material for systemic therapeutic applications [113]. Nanoprecipitation-based coating of hydrophobic porous silicon nanoparticles with amphiphilic block-copolymers containing poly(histidine) has also been explored for pH-triggered release of small molecules. However, this approach has not been utilized to deliver intracellular-acting biologics and its potential endosomal-disrupting function has not been explored [114].

Our group recently developed an endosomolytic polymer poly[(ethylene glycol) – *block* – (2-(dimethylamino)ethyl methacrylate – *co* – butyl methacrylate)] (PEGDB), and tuned it to have

optimal endosomal escape properties for systemic delivery of negatively-charged nucleic acids [28]. PEGDB consists of a hydrophilic PEG block and a second block comprising 50:50 mol% of cationic and pH-responsive 2-(dimethylamino)ethyl methacrylate (DMAEMA; D) and hydrophobic butyl methacrylate (BMA; B). The resulting polymer is finely tuned to disrupt membranes in acidic environments representative of early (pH 6.8) and late endosomes (pH 6.2) but not at physiologic pH (pH 7.4) [28]. Neutrally charged PNA cannot be electrostatically loaded into PEGDB polyplexes. Here, we explored oxidized, PNA-loaded PSNPs with a highly negative surface charge as "scaffolds" for PEGDB electrostatic surface coating. We demonstrate that this approach yields surface charge neutral composite NPs with enhanced stability, improved pharmacokinetics, and increased cytosolic delivery and bioactivity of PNA relative to PSNPs without a polymeric coating.

4.2 Materials and methods

4.2.1 PSNP fabrication. PSi films were etched from p-type Si (0.01Ω-cm) using 15% hydrofluoric acid in ethanol. Multilayer films used for PSNP generation were fabricated by multiple repetitions of two anodization steps: 60 mA cm^{-2} for 8 s to yield "particle" layers with 75% porosity, and 100 mA cm^{-2} for 2 s to form mechanically fragile "lift-off" layers. Afterwards, PSi films were fractured into particles by ultrasonication in H_2O_2 for 2 h. To further oxidize the particle surfaces, ultrasonicated PSi in H_2O_2 was transferred to a hotplate and heated while stirring at 115°C for 4 hours. The particles were then transferred to ultracentrifuge tubes and washed 3x by pelleting at 14.1 x g for 15 min and replacing the supernatant with fresh ethanol. Following the final wash step, PSNPs were isolated from larger debris by centrifuging at 300 x g and collecting the smaller nanoparticles in the supernatant.

4.2.2 PNA synthesis and loading. Non-specific adsorption, rather than *in* situ PNA synthesis, was selected as the method for PNA loading in this chapter so that the negatively-charged PSNP surface would be accessible for PEGDB coating. Cysteine-modified anti-miR122 PNA (NH2-ACA AAC ACC ATT GTC ACA CTC CA-cys-COOH) used in this chapter was synthesized from Rink Amide LL resin (EMD Millipore) using fluorenylmethyloxycarbonyl chloride (Fmoc) solid phase chemistry within a PS3 automated peptide synthesizer (Protein Technologies). Note that all PNA used in Chapter 4 was modified by addition of a single cysteine at the C-terminus of the PNA. This was done to promote crosslinking of PNA following loading into PSNPs and reduce PNA diffusion from pores. PNA was purified by reverse-phase high-pressure liquid chromatography using a Waters 1525 series HPLC equipped with a Phenomenex Luna C18 (10 x 250 mm, 5μm) column (linear gradient from 99% H2O 0.01% formic acid to 40% ACN 0.01% FA in 18 minutes with a flow rate of 3 mL min^{-1}). PNA was confirmed to be >99% pure by liquid chromatography-mass spectrometry (LC-MS).

Fluorescent PNA used in cell uptake and co-localization studies were labeled by coupling the PNA N-termini to Oregon Green 488 carboxylic acid, succinimidyl ester. Similarly, fluorescent PNA used in circulation half-life and biodistribution studies were labeled by coupling N-termini to Cy5 N-hydroxysuccinimidyl ester. In both cases, PNA and fluorophores were reacted for 1 hour in PBS containing (tris(2-carboxyethyl)phosphine) at pH 7.5. Fluorescent PNA was purified from unreacted products using a PD Miditrap G-10 desalting column (GE Healthcare Life Sciences).

PNA was loaded into PSNPs by non-covalent physical adsorption. Composite PSNPs were impregnated with PNA prior to polymer coating. PNA dissolved in deionized H_2O was added to a solution of oxidized PSNPs in H_2O at a 1:2 PNA:PSNP weight ratio. The PNA/PSNP solution was

briefly ultrasonicated and then mixed on a shaker at room temperature for 3 hours. Finally, PNA-loaded PSNPs were frozen at -80°C and lyophilized overnight. Excess PNA was purified from drug loaded PSNPs by suspending lyophilized particles in H_2O, centrifuging particles at 15k x g for 15 min, then removing the supernatant.

PNA loading was quantified by first dissolving/degrading the PSi substrate in PBS with 10 mM KOH for 48 hours at 37°C. Samples were then spun at 15,000 x g for 10 min, and 150 µL of supernatant was removed and analyzed for PNA content by liquid chromatography mass spectrometry (LCMS). The gradient described in Table 4.1 was used to separate any polymer or silicon from the PNA, which was detected in elutant at 6.5 min after injection. PNA concentration was calculated by integration of the peak at 6.5 min in the total ion count (TIC) chromatograph, and comparing against a standard curve of free PNA injected under the same conditions.

Table 4.1. LCMS Gradient for PNA purification. Solvent A=H_2O+0.05% Formic Acid, and solvent B=CAN.

Time (min)	Flow (ml min^{-1})	%A	%B
0	0.3	99	1
1	0.3	99	1
5	0.3	95	5
10	0.3	0	100
11	0.3	0	100
15	0.3	99	1

4.2.3 PEGDB polymer synthesis. The reversible addition-fragmentation chain transfer (RAFT) chain transfer agent for polymer synthesis, ECT, was synthesized as previously described, and the R-group of the chain transfer agent was subsequently conjugated to PEG. Briefly, dicyclohexylcarbodimide (4 mmol, 0.82 g) was added to the stirring solution of monomethoxy-

poly(ethylene glycol) (Mn = 5000, 2 mmol, 10 g), ECT (4 mmol, 1.045 g), and 4-dimethylaminopyridine (DMAP, 10 mg) in 50 mL of dichloromethane. The reaction mixture was stirred for 48 h. The precipitated cyclohexyl urea was removed by filtration, and the dichloromethane layer was concentrated and precipitated into diethyl ether twice. The precipitated PEG-ECT was washed three times with diethyl ether and dried under vacuum (yield ~10g). ^{1}H-NMR (400 MHz $CdCl_3$) revealed 91% substitution of the PEG (data not shown)[28].

RAFT polymerization was used to synthesize a 50:50 butyl methacrylate (BMA; B):2-(dimethylamino)ethyl methacrylate (DMAEMA; D) copolymer using the PEG-ECT macro-CTA. The target degree of polymerization was 160, and the monomer plus CTA was 40% weight per volume in dioxane. The polymerization reaction was carried out at 70^{o}C for 24 hours using AIBN as the initiator with a 5:1 [CTA]:[Initiator] molar ratio. A monomer feed ratio of 50:50 mol % [B]:[D] was used, and a double alumna column was utilized to remove inhibitors from D and B monomers prior to polymerization. The reactions were stopped by removal from heat and exposure of the polymerization solution to air. The resulting PEGDB polymers were precipitated into a co-solvent of 90% pentane and 10% diethyl ether. The isolated polymers were vacuum-dried, dissolved in water, further purified by dialysis for 24 hours, and lyophilized. Polymers were characterized for composition and molecular weight by ^{1}H-NMR spectroscopy (Bruker 400 MHz spectrometer equipped with a 9.4 T Oxford magnet). Absolute molecular weight and polydispersity of PEGDB polymers was determined using DMF mobile phase gel permeation chromatography (GPC, Agilent Technologies, Santa Clara, CA, USA) with inline Agilent refractive index and Wyatt miniDAWN TREOS light scattering detectors (Wyatt Technology Corp., Santa Barabara, CA).

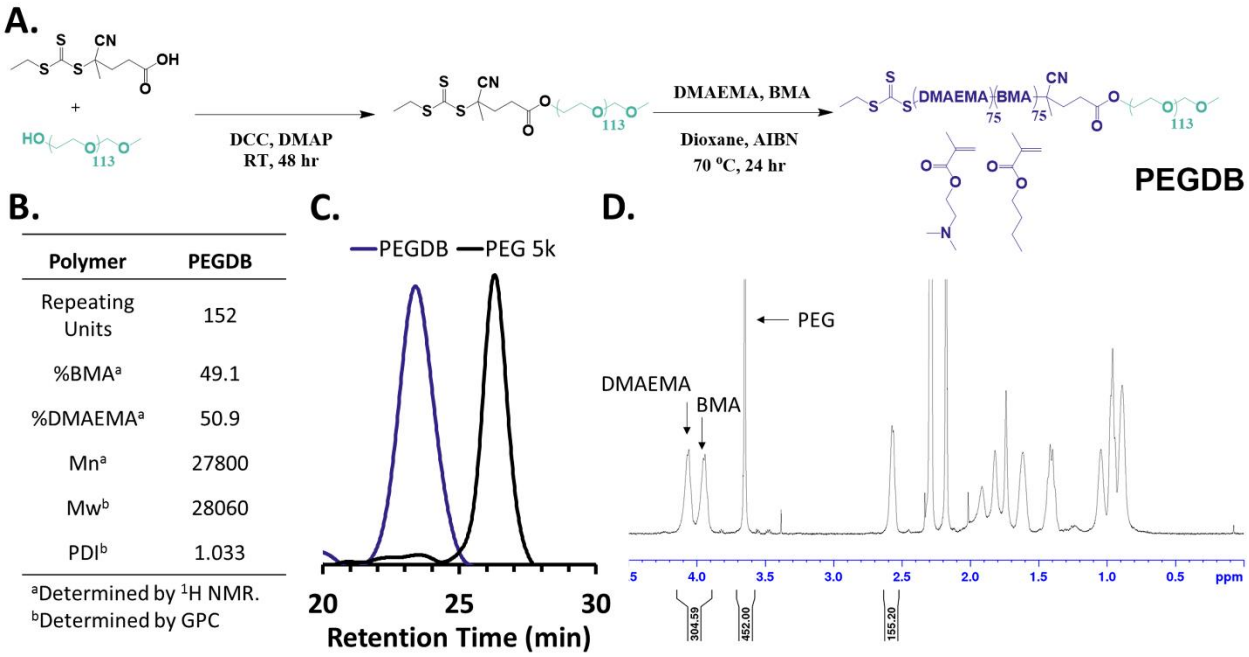

Polymer	PEGDB
Repeating Units	152
%BMA[a]	49.1
%DMAEMA[a]	50.9
Mn[a]	27800
Mw[b]	28060
PDI[b]	1.033

[a]Determined by ^{1}H NMR.
[b]Determined by GPC

Figure 4.1. Polymer synthesis and characterization. **A)** PEGDB synthesis scheme. **B)** Table of polymer characterization values. **C)** Gel permeation chromatography elugram of PEGDB and 5 kDa PEG-ECT precursor. **D)** ^{1}H NMR spectrum of PEGDB. [Adapted from *Advanced Materials*, Kelsey R. Beavers et. al., "Porous Silicon and Polymer Nanocomposites for Delivery of Peptide Nucleic Acids as Anti-MicroRNA Therapies", 2016, with permission from John Wiley & Sons]

4.2.4 Nanocomposite formation. The surface of oxidized porous silicon is negatively charged (ζ= -20mV) at pH 5.5. At that pH, the PEG-(DMAEMA-co-BMA) is positively charged and largely unimeric in solution. Composite particles were formed electrostatically by mixing the two components together in de-ionized H_2O (pH 5.5) while stirring at RT for 30 min, and the pH was subsequently raised to 7.4 using PBS. Coated PSNPs were purified from excess polymer by pelleting under centrifugation and removing the supernatant. The relative amounts of PEGDB and porous silicon within the composites were quantified by thermal gravimetric analysis (TGA). DLS and zeta potential measurements were performed using a Zetasizer NanoZS (Malvern Instruments, Worcestershire, UK) to assess changes in particle size and surface charge following polymer coating. Lastly, coated particle morphology and elemental composition were characterized by

scanning transmission electron microscopy-energy-dispersive X-ray spectrometry (STEM-EDS), using a Tecnai Osiris microscope (FEI, Oregon, USA) at a 120 keV accelerating voltage.

4.2.5 Cell culture and in vitro bioactivity. Huh7 cells were cultured in Dubelcco's modified eagle medium supplemented with 10% fetal bovine serum, 2% penicillin/streptomycin, and 2 μg mL^{-1} ciprofloxacin. To characterize cellular uptake by confocal microscopy and flow cytometry, Huh7 cells were treated for 24 h with either free Oregon Green-labeled PNA, or labeled PNA loaded into uncoated, partially coated, and fully coated composite PSNPs at a 2 μM PNA dose.

Huh7-psiCHECK-miR122 luciferase reporter cells were used to assay for anti-miR122 activity [115]. Cells were seeded at 3,000 cells per well in 96-well black-walled plates and allowed to adhere overnight. Cells were then treated in 10% serum for 24 hours at a 2 μM PNA dose. Luciferase expression was measured in triplicate using a Dual Luciferase Assay Kit (Promega Corporation, Madison, WI) according to the manufacturer's protocol, and the luminescence was recorded an IVIS Lumina III imaging system (Xenogen Corporation, Alameda, CA, USA). Relative luciferase expression was calculated as the average ratio of *Renilla* to firefly luciferase expression for each of the three triplicates. Cytotoxicity was calculated from the constitutively expressed firefly luciferase luminescence.

4.2.6 Ex vivo hemolysis assay for endosomal escape. Red blood cells (RBCs) were isolated from human whole blood according to well-established protocols [116]. RBCs were then incubated with either PEGDB (15 μg mL^{-1} PEGDB) or PSNPs alone (24 μg mL^{-1} PSNPs), or with composite PSNPs (at PEGDB concentrations of 15 μg mL^{-1}) in buffers of pH 7.4, 6.8, 6.2, and 5.6. The pH of these buffers was selected to model the extracellular, early endosome, late endosome, and

lysosome environments, respectively, encountered along the endolysosomal pathway. After 1 h of incubation, RBCs were pelleted by centrifugation, and the supernatant was spectrophotometrically analyzed at 451 nm to determine percent hemolysis relative to Triton X-100 detergent.

4.2.7 In vivo pharmacokinetics and biodistribution. CD-1 mice (10 weeks of age; Charles River) were injected intravenously into the tail vein with cy5-labeled anti-miR122. Retro-orbital blood collection was performed at 5 and 10 min after injection (n=8 per treatment group). In a second cohort of mice (n=5 per treatment group), retro-orbital blood collection was performed at 40 and 80 min after injection. Circulation half-life was determined by measuring Cy5 fluorescence in the plasma collected retro-orbitally at 5, 10, 40 and 80 min. The % injected dose in plasma was quantified by comparing to a known set of PNA standards in PBS (-/-) over the range of 200% to 1.5% of the injected dose.

Mice were euthanized 1 min, 20 min, 160 min, and 24 h after injection and organs were harvested for biodistribution analysis. An IVIS Lumina III imaging system was used to quantify Cy5 fluorescence in explanted lungs, heart, liver, kidney, and spleen using Living Image 4.4 quantification software. Pharmacokinetics curves were calculated from each organ by integrating each curve from 0–24 h after injection, after baseline subtraction of tissue autofluorescence quantified in a saline control group. Bioavailability in major organs was then quantified from the average of the areas under the pharmacokinetics curves for each organ. For Si content analysis, organs were weighed, homogenized in 3 mL of 20% ethanol in 1N NaOH and left for 48 h at room temperature for extraction of Si. Organ homogenate was then centrifuged at 42000 x g for 25 min. Following centrifugation, 1 mL of the supernatant was removed and diluted to 10 mL using de-ionized H_2O. Finally, all samples were syringe filtered using a 0.2 μm syringe

filter, and Si content was measured using inductively coupled plasma-optical emission spectroscopy (ICP-OES) analysis.

ICP-OES analyses of aqueous / homogenized tissue samples were carried out at Vanderbilt University (Department of Civil and Environmental Engineering) using an Agilent ICP Model 720-ES. A seven-point standard curve was used for an analytical range between approximately 0.05 mg L^{-1} and 10 mg L^{-1} for silicon at a wavelength of 252 nm. Analytical blanks and analytical check standards at approximately 0.5 mg L^{-1} were run and required to be within 15% of the specified value. When applicable, analyses were performed on undiluted samples to minimize total dissolved loading to the instrument. Samples for analysis were diluted gravimetrically to within the targeted analytical range using 2% v/v Optima grade nitric acid (Fisher Scientific) if the maximum calibration was exceeded. Yttrium at 1 mg L^{-1} was used as the internal standard. Instrument settings were 1 kW radio frequency (RF) power, 15 mg L^{-1} argon plasma flow, 0.75 L min^{-1} nebulizer flow, and 5 seconds per replicate read time for 3 replicates.

4.2.8 In vivo miR-122 inhibition and toxicology. Female C57BL/6J mice (12 weeks age, Jackson Laboratories) were divided into the following 6 treatment groups (6 mice per group): saline, empty composite PSNPs, free anti-miR122 PNA (5 mg kg^{-1} PNA), PNA loaded into uncoated PSNPs (1 mg kg^{-1} PNA), or PNA loaded into composite PSNPs (1 and 5 mg kg^{-1} PNA). Note that uncoated PSNPs were not assessed at the 5 mg kg^{-1} PNA dose due to acute toxicity caused by particle instability—further emphasizing the translational significance of the coating approach. Mice were injected intravenously into the tail vein every other day for 6 days (3 injections). Mice were sacrificed on day 6 and the livers were harvested for histology, mRNA, and miRNA analysis.

Real-time PCR and individual TaqMan assays were used to quantify levels of miR-122 and its mRNA targets. RNA was isolated from liver tissue using Qiazol and miRNeasy Mini Kits (Qiagen Venlo, Netherlands) and purified with RNeasy spin column (Qiagen, Venlo, Netherlands). The RNA was reverse transcribed using a Taqman microRNA reverse transcription kit based on manufactures instructions (Applied Biosystems) and miR-122 was quantified by real-time PCR with individual TaqMan miRNA assays (assay ID: 002245, Applied Biosystems). Relative quantitative values were determined using the ΔCT method ($RQV = 2^{-(Ct(miRNA)-Ct(U6))}$) normalized to U6. For mRNA quantification, 1 µg of total RNA was reverse transcribed with an iScript™ Reverse Transcription Supermix kit (Bio-Rad Laboratories), and *Aldoa*, *Gys1*, *MTTP*, *IL-6*, and *TNA-α* were quantified by real-time PCR with TaqMan mRNA assays (assay IDs: Mm00833172_g1, Mm01962575_s1, Mm00435015_m1, Mm00446190_m1, and Mm00443258_m1, Applied Biosystems) and normalized to peptidylprolyl isomerase A (PPIA). Relative quantitative values were determined using the ΔCt method ($RQV = 2^{-(Ct(mRNA)-Ct(PPIA))}$).

Plasma collected from cardiac puncture on day 6 was used to analyze mouse plasma cholesterol using heparin as an anti-coagulant. Mouse plasma was injected into an ÄKTA Pure FPLC using a Superdex 200 increase 10/300 column (Amersham BioSciences). HDL and LDL fractions were pooled separately, and then concentrated using Amicon Ultra 15 mL centrifugal filters with a MW cut-off of 3 kDa. Total cholesterol in the concentrated HDL or LDL fractions was quantified using a Wako Total Cholesterol Kit, as per manufacturer's instructions, and normalized to total protein content using Pierce BCA Protein Assay kit. Results are presented relative to cholesterol content in the HDL and LDL fractions of mice injected with saline only.

Blood collected by cardiac puncture on day 6 was used for toxicological analysis. Serum alanine aminotransferase (ALT) levels (marker of liver toxicity) and blood urea nitrogen (BUN)

levels (marker of kidney toxicity) were measured using a commercially available Transaminase-CII kit and Blood Urea Nitrogen-B Test (Wako), respectively. Livers harvested on day 6 were formalin fixed and paraffin embedded and stained with H&E, then evaluated by an experienced veterinary pathologist blinded to the composition of the groups. There was no evidence of liver toxicity observed microscopically.

Mice were fed a standard chow diet ad libitum and had free access to water. All protocols were approved by the Institutional Animal Care and Use Committee of Vanderbilt University and done in accordance with the NIH Guide for the Care and Use of Laboratory Animals.

4.3 Results and discussion

Scheme 4.1 depicts the strategy for PSNP-polymer nanocomposite formation. PSNPs were fabricated by ultrasonic fracture of multi-layer porous silicon films and then oxidized in H_2O_2 at 115ºC for 4 hours. The PEGDB diblock polymer was synthesized based on previous work by Nelson et al., and comprised a 5 kDa PEG block and a BMA/DMAEMA copolymer block with approximately 50 mol% of each monomer (**Figure 4.1**) [28]. In deionized water at pH 5.5, the surfaces of oxidized PSNPs are negatively charged (ζ = -20 mV), while the tertiary amines on DMAEMA (pKa ~ 6) are predominantly protonated, making PEGDB positively charged and unimeric in solution. Composite particles were formed electrostatically by mixing the two components together in de-ionized H_2O (pH 5.5) while stirring at room temperature for 30 min. Coated PSNPs were purified from excess polymer by centrifugally pelleting the PSNP-polymer composites and removing the supernatant containing free, unbound polymer. The particle pellet was then re-suspended in phosphate buffered saline at physiologic pH (pH 7.4). Exposure of the DB polymer block to physiologic pH makes it water-insoluble and triggers polymer self-

aggregation [28], potentially contributing to hydrophobic stabilization of the surface coating and stabilization of the drug loading into the PSNP interior pores. At physiologic pH, addition of PEGDB neutralizes negative PSNP surface charge (**Scheme 4.1**), which is important for systemic delivery applications [112].

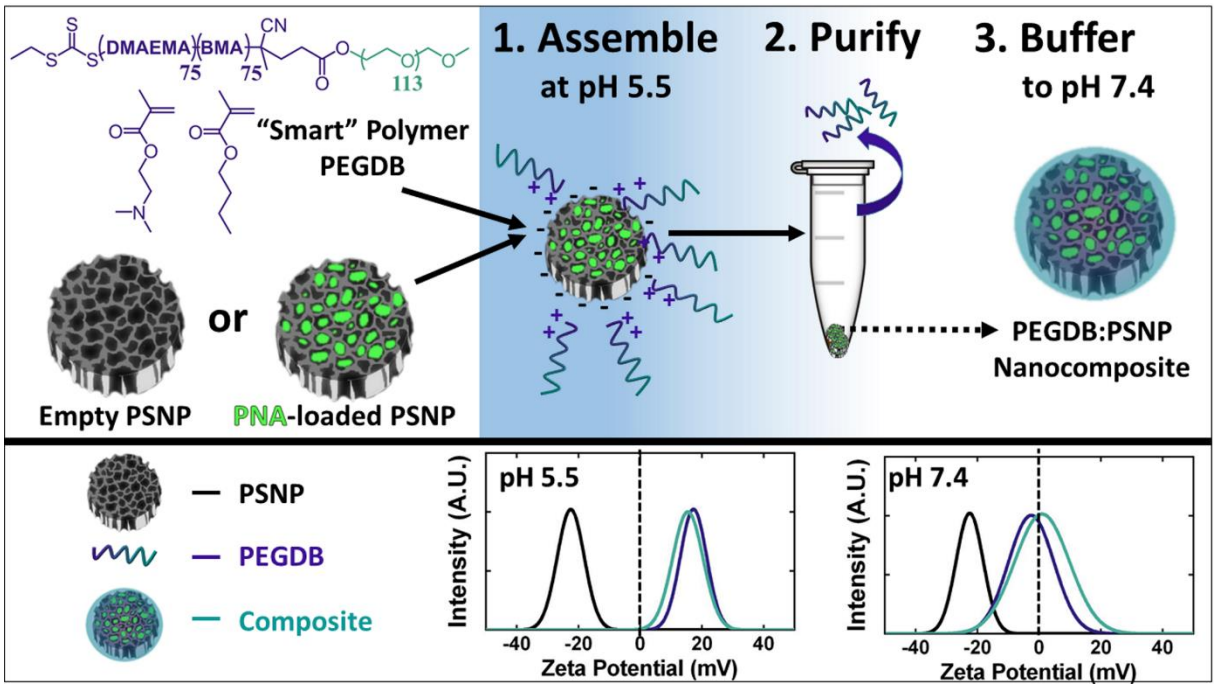

Scheme 4.1. PSi-polymer nanocomposite fabrication. 1. Electrostatic assembly of PEGDB on the negatively charged PSNP surface. 2. Purification of nanocomposites by removal of free PEGDB in the supernatant following centrifugation. 3. Buffering the nanoparticle solution to physiologic pH increases polymer self-aggregation, potentially contributing to hydrophobic stabilization of the surface coating and drug loading into the PSNP interior pores. The bottom panel shows surface charge of oxidized PSNPs, PEGDB, and nanocomposites during assembly at pH 5.5, and after buffering pH to 7.4. [Adapted from *Advanced Materials*, Kelsey R. Beavers et. al., "Porous Silicon and Polymer Nanocomposites for Delivery of Peptide Nucleic Acids as Anti-MicroRNA Therapies", 2016, with permission from John Wiley & Sons, Ltd.]

The ratio of PEGDB polymer to porous silicon was tuned to create a library of nanocomposites with varied degrees of polymer surface functionalization (**Figure 4.2**). Reactant weight ratios of 1:5, 1:1, 20:1, and 80:1 (PEGDB:PSNP) yield composite particles containing 12, 24, 50, and 60 wt% PEGDB, respectively, as determined by thermal gravimetric analysis (TGA) (**Figure 4.2A**). Dynamic light scattering (DLS) measurements reveal that as % PEGDB is increased, the PSNP ζ-potential at physiologic pH (7.4) increases and approaches charge neutrality (**Figure 4.2B**). The average hydrodynamic diameter of nanocomposites with up to 24 wt% PEGDB is the same as that of uncoated PSNPs (220 nm) (**Figure 4.2C**). Scanning transmission electron microscopy-energy-dispersive X-ray spectrometry (STEM-EDS) analysis of nanocomposites confirms that nitrogen and sulfur signals generated by PEGDB co-localize with the Si matrix at the nano-scale, supporting our hypothesis that electrostatic interactions facilitate PEGDB assembly onto the PSNP surface (**Figures 4.2D and 4.3**). Spectroscopic evaluation of PSNP colloidal stability reveals that coating of PSNPs with PEGDB minimizes particle aggregation and precipitation in the presence of salt-containing physiologic buffered saline (**Figure 4.2E-F**). This increased stability can be attributed to PEG's ability to sterically block surface adsorption of proteins and ions, consequently preventing particle aggregation [117].

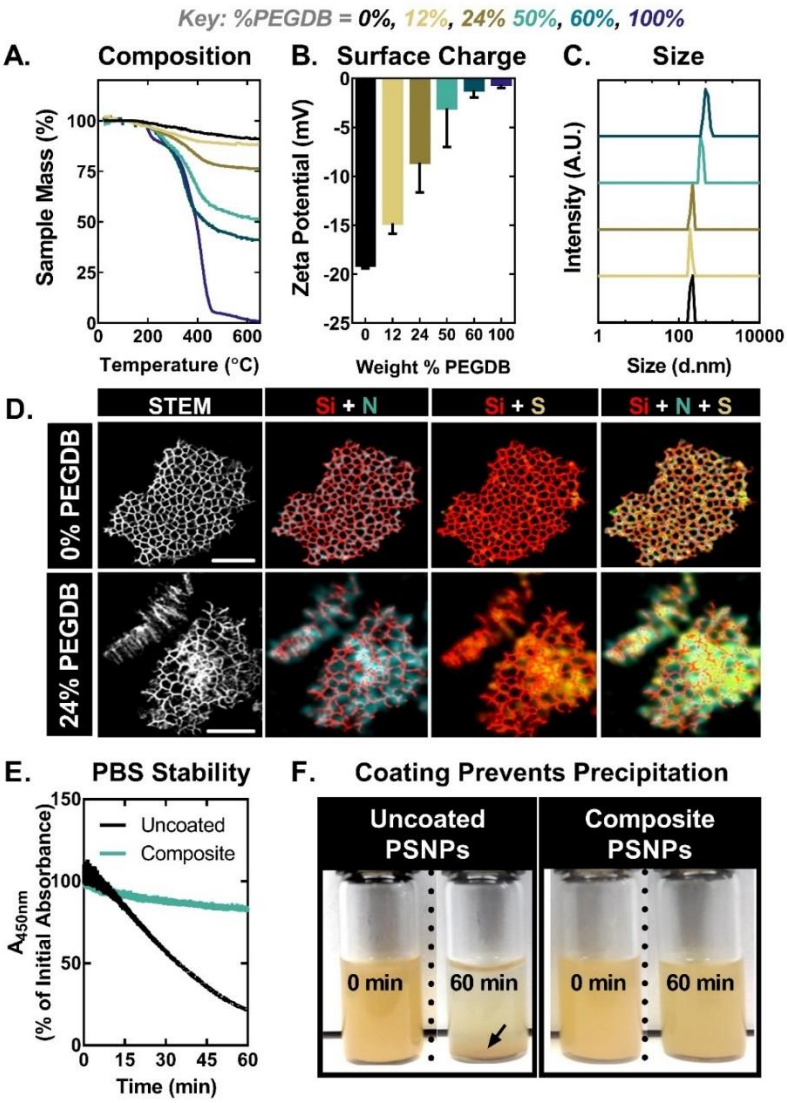

Figure 4.2. PEGDB effectively coats PSNPs, neutralizing particle surface charge and imparting colloidal stability within physiologic buffered saline. Characterization of nanocomposite library by **A)** thermal gravimetric analysis, **B)** ζ-potential, and **C)** hydrodynamic size measurements acquired in PBS at pH 7.4. **D)** STEM-EDS elemental mapping of (top) an uncoated PSNP and (bottom) composite PSNPs partially coated with PEGDB (24 wt%). The increased strength and dispersion of N and S signals in elemental maps of composite particles (bottom) indicates successful PEGDB coating of the PSNP matrix. High-angle annular dark-field images are shown in the left-most panels. Maps of Si, N, and S are indicated in red, teal, and yellow, respectively. Scale bar = 200 nm. **E)** Particle aggregation and precipitation out of solution, quantified by monitoring PSNP absorption at 450 nm over time, shows that fully coated 50% PEGDB nanocomposites have increased colloidal stability in PBS. **F)** Photographs depict PSNP and composite colloidal stability in PBS after 60 min. Black arrow indicates precipitated PSNPs. [Adapted from *Advanced Materials*, Kelsey R. Beavers et. al., "Porous Silicon and Polymer Nanocomposites for Delivery of Peptide Nucleic Acids as Anti-MicroRNA Therapies", 2016, with permission from John Wiley & Sons, Ltd.]

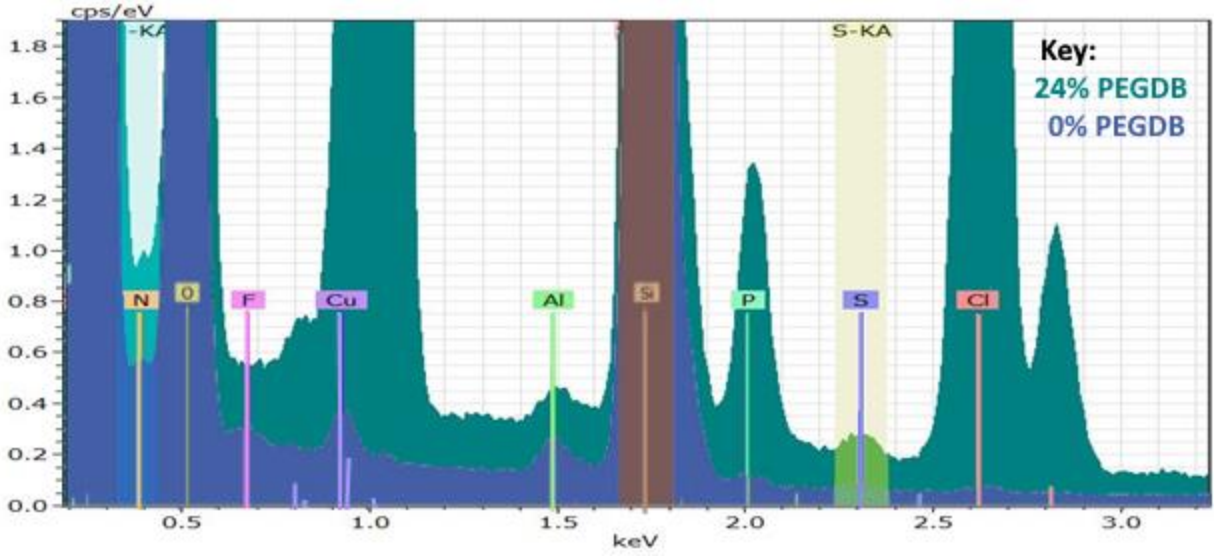

Figure 4.3. STEM-EDS Spectra of oxidized PSNPs and 24% Composite PSNPs shown in Figure 4.2D. Cu and Al signals are background from the TEM sample holder. Cl, Na, and P signals are due to the presence of salts from the PBS buffer in which the particles are fabricated. Si is attributed to the porous silicon matrix, and O can be attributed to both the oxide on the PSNP surface as well as within the PEG chain. N and S signals are attributed to PEGDB (see Scheme 4.1 and Figure 4.1 for chemical structure). [Adapted from *Advanced Materials*, Kelsey R. Beavers et. al., "Porous Silicon and Polymer Nanocomposites for Delivery of Peptide Nucleic Acids as Anti-MicroRNA Therapies", 2016, with permission from John Wiley & Sons, Ltd.]

To assess the impact of PEGDB coating density on PSNP uptake and anti-miRNA activity, composites with the minimum amount of PEGDB necessary to fully shield the porous silicon surface (50 wt%, zeta -3.1 ± 4.0 mV), and composites which were only partially shielded by PEGDB (24 wt%, zeta -8.6 ± 3.0 mV) were selected for further in vitro characterization. Cell internalization and bioactivity was assessed for a PNA designed to inhibit miR-122, a liver-specific miRNA involved in cholesterol biosynthesis. Inhibition of miR-122 is a promising therapeutic approach for reducing viremia in patients infected with Hepatitis C, as well as lowering elevated cholesterol and triglyceride levels due to hypercholesterolemia [118]. In this study, nanocomposites were loaded with anti-miR122 PNA (NH_2-ACA AAC ACC ATT GTC ACA CTC CA-cys-COOH) by physically adsorbing PNA within oxidized PSNPs, followed by coating with

PEGDB as described above. The average PNA loading in the nanoparticle formulations was quantified by LCMS to be 34, 22, and 20 nmoles PNA per mg porous silicon (21, 14, and 12 wt% PNA) for uncoated, partially coated, and fully coated nanocomposites, respectively (**Figure 4.4 and Table 4.2**). To our knowledge, this is the highest reported PNA loading in any nanoparticle system, and is 60x higher than what has been reported for anti-miRNA PNA loading in PLGA nanoparticles [69], highlighting an important advantage of highly porous PSNPs that do not require emulsion fabrication/loading approaches.

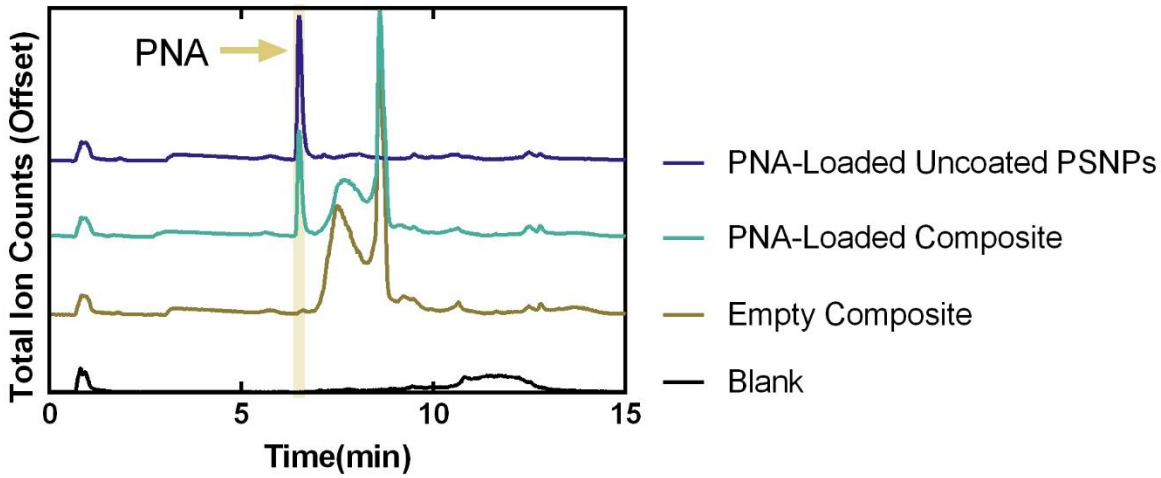

Figure 4.4. LCMS chromatographs used to evaluate PNA loading in PSNPs, showing how the polymer component of the composite was separated from PNA for drug loading quantification. The highlighted peaks were confirmed to be pure anti-miR122 PNA by mass spectrometry. [Adapted from *Advanced Materials*, Kelsey R. Beavers et. al., "Porous Silicon and Polymer Nanocomposites for Delivery of Peptide Nucleic Acids as Anti-MicroRNA Therapies", 2016, with permission from John Wiley & Sons, Ltd.]

Table 4.2. PSNP PNA loading calculated from LCMS.

Sample	PNA/PSNP (wt%)	PNA (nmoles mg^{-1})
Empty Comp	0	0.0
PNA-Loaded Full Composite	12	19.8
PNA-Loaded Partial Composite	14	21.9
PNA-Loaded Uncoated PSNPs	21	34.3

Cellular uptake and miR-122 inhibition studies were performed in vitro using Huh7 human liver cancer cells (**Figure 4.5)**. Cells were treated for 24 h in Dubelcco's modified eagle medium (DMEM, Gibco Cell Culture, Carlsbad, CA) supplemented with 10% fetal bovine serum, at a 2μM dose of PNA. Following treatment, uptake of fluorescently-labeled PNA was quantified by flow cytometry and imaged by confocal microscopy. PNA encapsulated in uncoated PSNPs is ~50x more efficiently internalized than free PNA (**Figure 4.5A**). Additionally, PNA uptake decreases proportionately with increasing wt% PEGDB (**Figure 4.5A and 4.5B**). This is likely due to PEG shielding on the outer surface of the composite [119]. Importantly, the extent of cytosolic PNA delivery increased with increasing PEGDB content, as quantified by co-localization analysis of PNA and lysosomes stained with LysoTracker®, 24 h after treatment (**Figure 4.5C**). This enhanced cytosolic PNA delivery can be attributed to both full and partial PEGDB nanocomposites possessing pH-dependent, membrane disruptive activity in a relevant endo-lysosomal range, whereas uncoated PSNPs do not (**Figure 4.5D**).

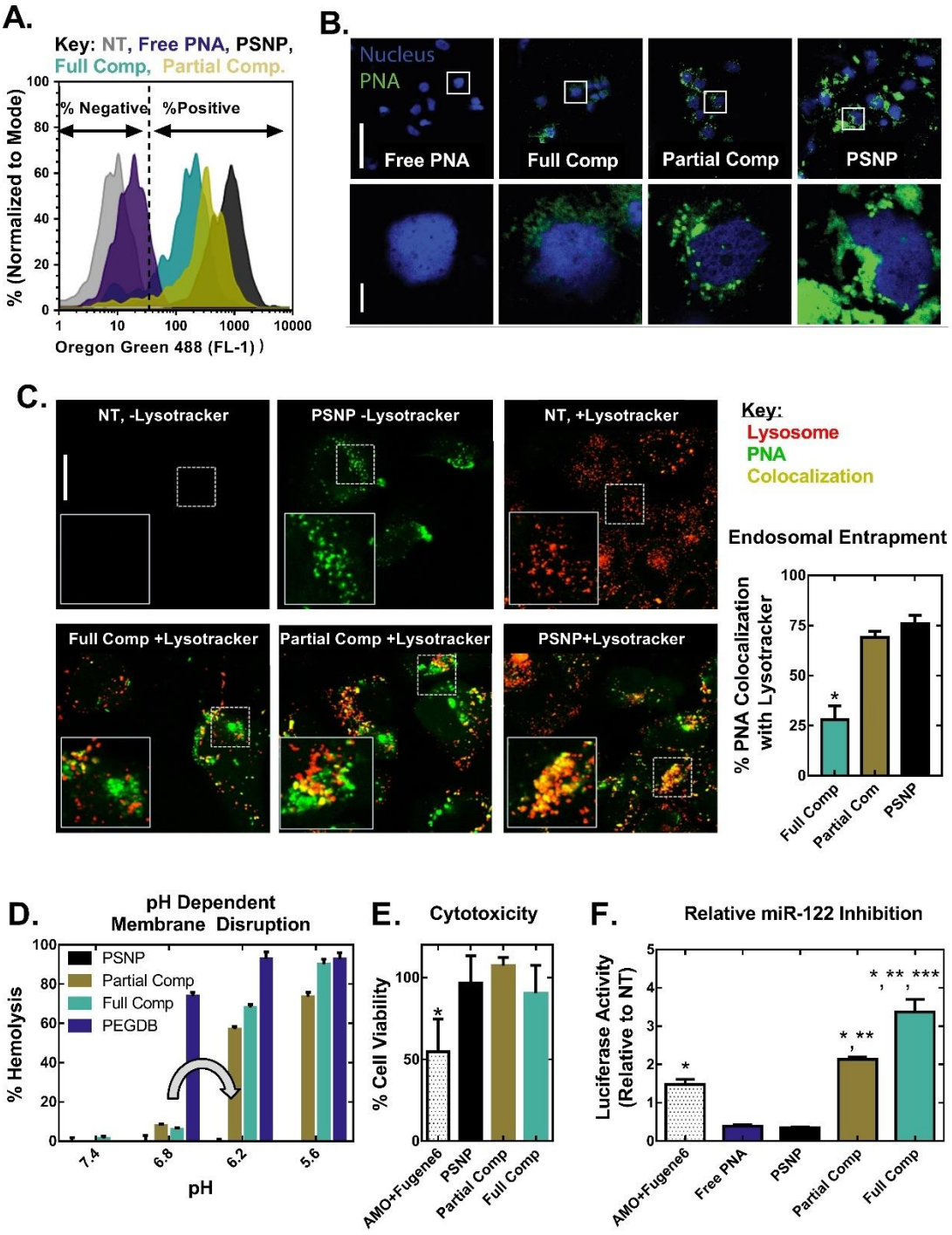

Figure 4.5. Coating of PSNPs with PEGDB decreases PNA uptake but increases both endosome escape potential and anti-miRNA activity relative to uncoated PSNPs in Huh7 human hepatocellular carcinoma cells. PEGDB functionalization decreases cellular uptake, as characterized by **A)** flow cytometry and **B)** confocal microscopy, 24 h after treatment with Alexa Fluor 488-labeled anti-miR122 PNA at a 2×10^{-6} M PNA dose. Top scale bar = 100 μm, bottom scale bar = 10 μm. **C)** PEGDB functionalization increases PNA cytosolic delivery, as shown by

colocalization analysis of Alexa Fluor 488-labeled PNA with LysoTracker at 24 h after treatment with 2×10^{-6} M PNA. Endosomal entrapment was quantified by calculating the Manders' overlap coefficients for green and red pixels, shown at the right as means ± SEM ($n \geq 3$ separate images). Increased cytosolic delivery observed for composite particles is due to **D)** the pH dependent membrane disruptive function (grey arrow) of PEGDB, as determined by a hemolysis assay. Composites did not disrupt erythrocyte membranes at pH 7.4, but produced robust hemolysis at pH 6.2, which is representative of late endosomes. **E)** A firefly luciferase assay reveals that all PSNP treatments are non-toxic at a 2×10^{-6} M PNA dose, in contrast to the gold-standard of a 2′OMe modified RNA delivered using a commercial cationic transfection reagent (AMO+Fugene6). **F)** Therapeutic anti-miR122 activity increases with increasing PEGDB polymer functionalization (based on *Renilla* luciferase readout tied directly to miR-122 inhibition) 24 h after treatment, when compared to free, unencapsulated PNA and the control, 2′OMe AMO ($p < 0.05$ when compared to *Free PNA or PSNP, **AMO+Fugene6, and ***Partial Comp). [Adapted from *Advanced Materials*, Kelsey R. Beavers et. al., "Porous Silicon and Polymer Nanocomposites for Delivery of Peptide Nucleic Acids as Anti-MicroRNA Therapies", 2016, with permission from John Wiley & Sons, Ltd.]

Anti-miR122 activity was quantified using Huh7 cells stably transfected with a *Renilla* luciferase sensor for endogenous miR-122 [115]. Inhibition of miR-122 in these cells causes an increase in luciferase signal. Both anti-miRNA activity and cytotoxicity were benchmarked against the anti-miRNA oligonucleotide (AMO) agent used in development and validation of this luciferase reporter cell line: 2'OMe PS modified RNA delivered with the cationic commercial transfection reagent, FuGENE® 6. All PSNP treatments cause significantly less cytotoxicity than FuGENE® 6 (**Figure 4.5E**), which is too toxic (and colloidally instable) for in vivo translation. Although cell uptake was reduced (**Figure 4.5A**), anti-miR122 activity was 6-fold and 10-fold greater than uncoated PSNPs for the partial and fully coated nanocomposites, respectively (**Figure 4.5F**). Furthermore, fully coated nanocomposite PSNPs demonstrate 2.3 fold higher miR-122 inhibition relative to the AMO standard. Taken together, these data suggest that fully coated composites are non-toxic and have potent anti-miRNA activity due to increased delivery of PNA to the cytosol, where miR-122 is located.

To evaluate whether nanocomposites improve the blood circulation half-life and miRNA inhibitory bioactivity of PNA in vivo, CD-1 mice (10 weeks of age, Charles River) were injected intravenously via the tail vein with 1 mg kg^{-1} cy5-labeled anti-miR122 PNA (free, loaded into uncoated PSNPS or fully coated nanocomposites) (**Figure 4.6**). Blood samples were collected 5, 10, 40, and 80 minutes after injection, and circulation half-life was determined based on the quantity of PNA in the plasma collected at each time point (**Figure 4.6A**). Uncoated PSNPs extended the circulation half-life of free PNA from <1 min to ~30min, and addition of the PEGDB coating to PSNPs more than doubled the half-life to nearly 70 min. As a result of increased circulation time, encapsulation of PNA anti-miR122 in nanocomposites increased its bioavailability by 73x, as quantified by the area under the curve (AUC).

The organ biodistribution of PNA and the PSNP carrier were determined by excising the heart, lungs, liver, spleen, and kidneys 160 min after injection. Investigations into novel nucleic acid delivery systems typically track the fluorescently-labeled nucleic acid without tracking the carrier system. An advantage of using porous silicon nanocarriers is that their biodistribution can be tracked label-free using inductively coupled plasma-optical emission spectroscopy (ICP-OES). **Figure 4.6B** compares the biodistribution of fluorescently labeled PNA cargo with that of Si from the porous silicon nanocarriers. The biodistribution of Si is similar to that of the PNA for both uncoated and composite nanoparticles, suggesting that the PNA cargo may remain stably associated with the porous silicon carrier in the circulation and during initial tissue biodistribution. It is well established that nanoparticles larger than 200 nm in size are preferentially sequestered in the liver sinusoidal endothelium [120]. Due to their size, PSNPs and nanocomposites increased PNA delivery to the liver (where hepatocytes containing the target miR-122 are located) by ~16%, and reduced the amount of PNA in the kidneys by ~33% when compared with free PNA (**Figure**

4.6B). ICP-OES analysis reveals a ~20% increase in Si in the spleen of composite particles when compared to uncoated particles. The spleen, like the liver, is known to play a primary role in nanoparticle clearance. Additionally, PEGDB coated nanoparticles display 12% less Si accumulation in lungs compared with uncoated PSNPs 160 min after injection, and 29% less lung bioavailability over 24 h (**Figures 4.6 and 4.7**), corroborating in vitro data (**Figure 4.2 E-F**) that PEGDB reduces flocculation which causes accumulation in the lungs [121]. A final observation is that while ~20% of all PNA is found in the kidneys, no more than 6% of all measured Si is detected in the kidneys by ICP-OES. Free PNA pharmacokinetics data suggests that the kidney is a preferential route of clearance, which is anticipated based on the small size of free PNA, below the renal cutoff. The difference in PNA and Si content suggests that a portion of the PNA cargo released from the PSNP carriers in circulation due to the noncovalent PNA loading mechanism.

We next tested whether PSNP-polymer nanocomposites improve PNA bioactivity (miR-122 inhibition) in the liver. Female C57BL/6J mice (12 weeks of age, Jackson Laboratories) were treated with either saline, free anti-miR122 PNA (5 mg kg^{-1} PNA), PNA loaded into composite PSNPs (5 mg kg^{-1} PNA, 42 mg kg^{-1} PSNP composite), or an empty composite vehicle control (42 mg kg^{-1} PSNP composite). Importantly, the uncoated nanoparticles demonstrated poor colloidal stability in physiologic solutions (**Figure 4.2E-F**). We were unable to safely inject uncoated PSNPs intravenously at 5 mg kg^{-1} PNA dose for this study due to acute mortality. The acute toxicity for the 5 mg kg^{-1} uncoated treatment group could be due to particle aggregation resulting in blockage of pulmonary capillaries. This result highlights the importance of the colloidal stabilization of PSNPs by PEGDB, which significantly reduced particle accumulation in the lungs (**Figures 4.6C and 4.7**).

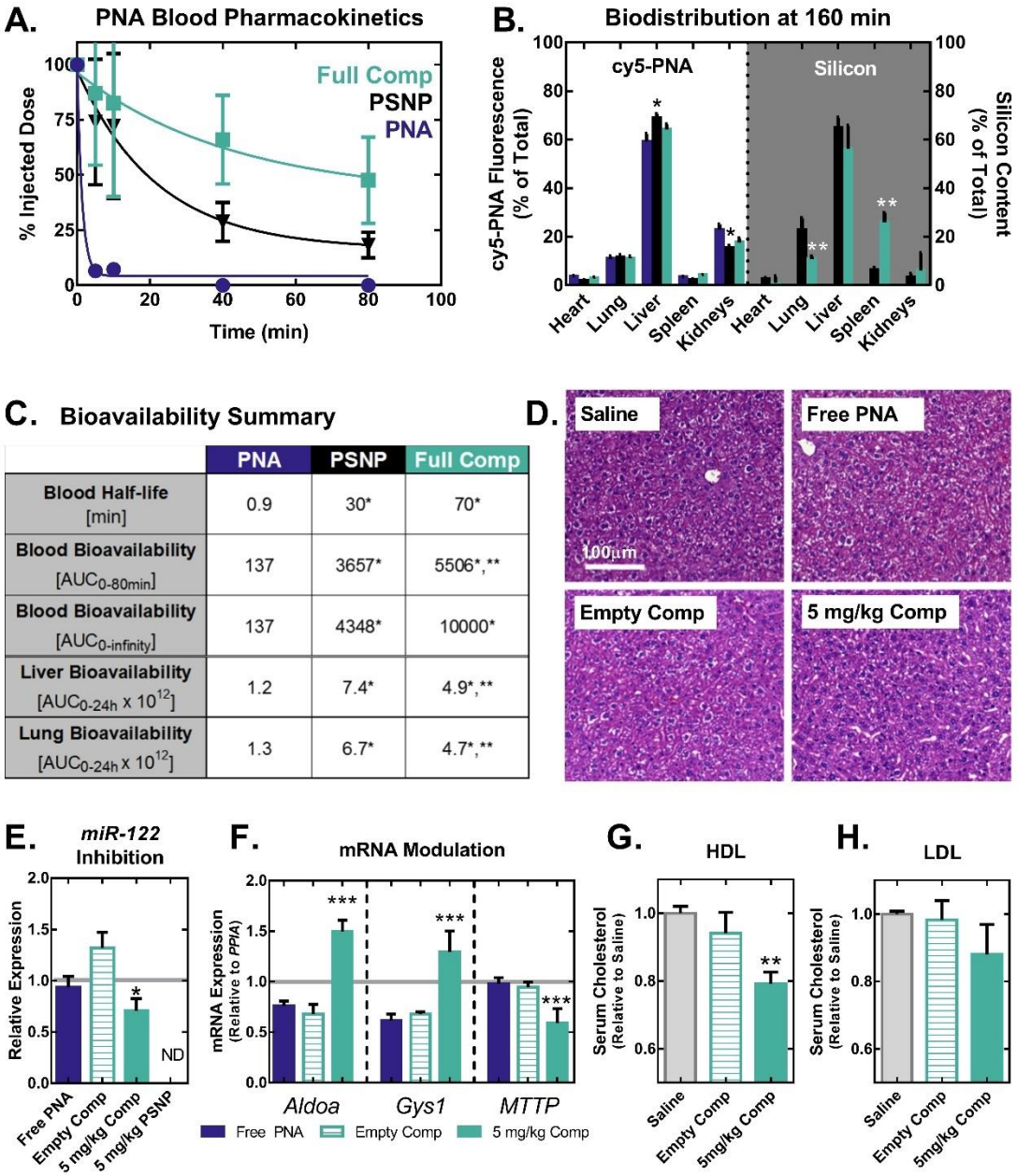

	PNA	PSNP	Full Comp
Blood Half-life [min]	0.9	30*	70*
Blood Bioavailability [$AUC_{0\text{-}80min}$]	137	3657*	5506*,**
Blood Bioavailability [$AUC_{0\text{-}infinity}$]	137	4348*	10000*
Liver Bioavailability [$AUC_{0\text{-}24h} \times 10^{12}$]	1.2	7.4*	4.9*,**
Lung Bioavailability [$AUC_{0\text{-}24h} \times 10^{12}$]	1.3	6.7*	4.7*,**

Figure 4.6. PSNP-polymer nanocomposites increase PNA blood circulation half-life, bioavailability, and anti-miRNA activity in vivo. **A)** Blood pharmacokinetics curves generated using cy5-labeled PNA show that PSNP composites increase circulation half-life of PNA when delivered I.V. through the tail vein of mice at a 1 mg kg^{-1}dose (n = 8 per group for 0–20 min, n = 5 per group for 40–80 min). **B)** In vivo biodistribution of cy5-PNA cargo and Si from the PSNP carriers was analyzed by fluorescent imaging and ICP-OES, respectively. PNA and Si organ distributions 160 min after injection show that PSNPs increase PNA accumulation in the liver and decrease uptake in the kidneys. **C)** Quantification of bioavailability in blood, liver, and lungs demonstrates that PEGDB functionalization improves blood circulation stability and decreases

accumulation of particles in the lungs. **D–H)** In vivo miR-122 inhibition studies following injection of a 5 mg kg^{-1} dose of PNA, every other day for 6 d (n = 6 mice per group). **D)** Livers were evaluated by an experienced veterinary pathologist blinded to the composition of the groups, who noted no evidence of liver toxicity observed microscopically (representative image shown,n = 6 mice per group). **E)** Nanocomposite delivery of anti-miR122 PNA **D)** significantly inhibits miR-122 and **F)** modulates the expression of miR-122 direct target genes, *Aldoa* and *Gys1*, in addition to the indirect target gene *MTTP* (Grey line indicates saline control). Cholesterol measurements on **G)** HDL and **H)** LDL fractions separated by fast protein liquid chromatography (FPLC) from plasma collected on day 6 reveals decreased cholesterol in HDL following treatment with nanocomposites loaded with anti-miR122 PNA. (*, **, and *** indicate $p < 0.05$ when compared to free PNA, PSNPs, and empty vehicle control, respectively). [Adapted from *Advanced Materials,* Kelsey R. Beavers et. al., "Porous Silicon and Polymer Nanocomposites for Delivery of Peptide Nucleic Acids as Anti-MicroRNA Therapies", 2016, with permission from John Wiley & Sons.]

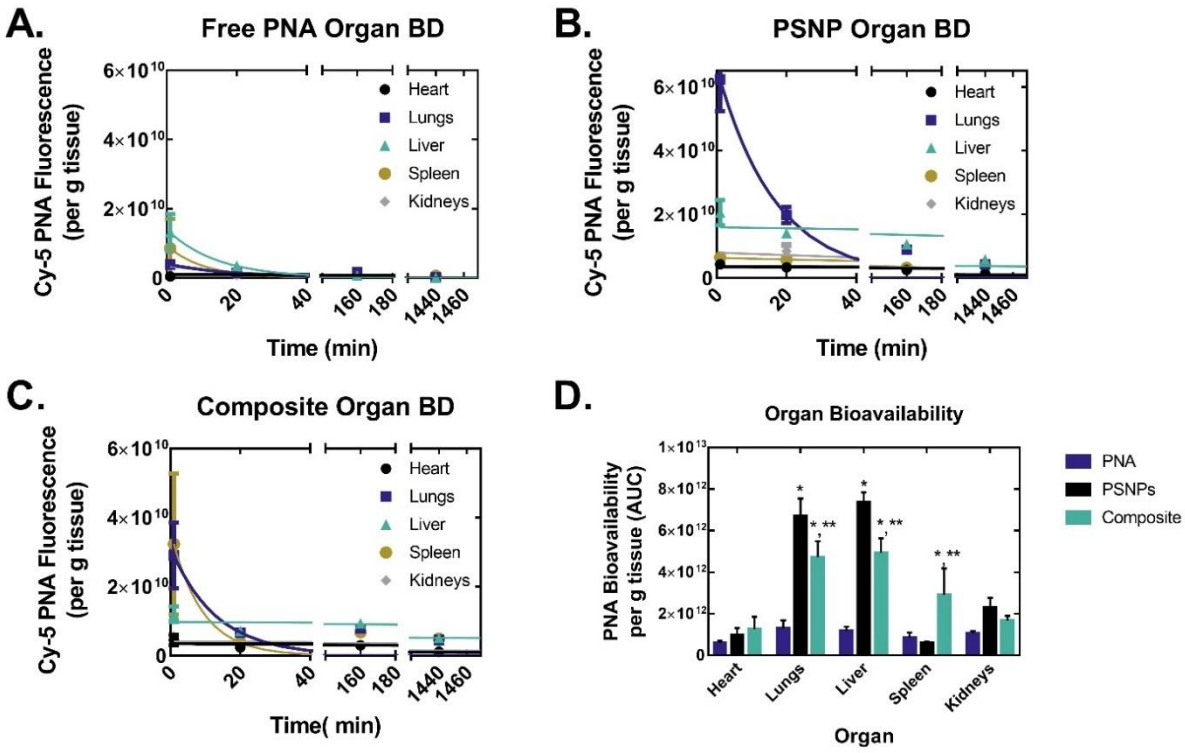

Figure 4.7. Biodistribution of cy5-PNA in the major organs as a function of time, following a single intravenous injection of **A**) 1 mg kg^{-1} free PNA, **B**) 1 mg kg^{-1} PNA loaded into uncoated PSNPs, and **C**) 1 mg kg^{-1} PNA loaded into composite nanoparticles (n > 3 mice/group). A non-linear, one-phase exponential decay model was used to generate pharmacokinetics curves for each data set (average curves shown as solid lines in charts A-C). **D**) PNA bioavailability was then characterized by calculating the area under the curves from 0-24 h. (* and ** indicate $p<0.05$ when compared to free PNA and PSNPs, respectively). [Adapted from *Advanced Materials*, Kelsey R. Beavers et. al., "Porous Silicon and Polymer Nanocomposites for Delivery of Peptide Nucleic Acids as Anti-MicroRNA Therapies", 2016, with permission from John Wiley & Sons, Ltd.]

Mice were injected intravenously into the tail vein every other day for 6 days (3 injections), then sacrificed, and their livers were harvested for mRNA, and miRNA analysis (**Figure 4.6 D-F**). There were no overt signs of toxicity for the composite nanoparticles, and levels of blood urea nitrogen (BUN) and alanine aminotransferase (ALT) measured on day 6 serum samples collected at the time of mouse sacrifice suggested that treatment did not cause kidney or liver toxicity relative to control treatment groups (**Figures 4.6D and 4.8**). Real-time PCR for miR-122 expression shows that composite PSNPs inhibited miR-122 by 46% relative to the empty vehicle control (**Figure 4.6E**). Additionally, treatment with nanocomposites caused an ~50% increase in expression of both Aldolase A (*Aldoa*) and Glycogen Synthase 1 (*Gys1*), validated miR-122 gene targets that encode for proteins which degrade cholesterol and synthesize glycogen, respectively (**Figure 4.6F**). Furthermore, expression of Microsomal Triglyceride Transfer Protein (*MTTP*), an indirect target of miR-122 known to be down-regulated upon miR-122 inhibition, was decreased by 36% relative to the vehicle control (**Figure 4.6F**) [122]. Finally, the functional impact of miR-122 inhibition was assessed by analyzing the cholesterol content in the high-density lipoprotein (HDL) and low-density lipoprotein (LDL) serum fractions collected from mice on day 6 (**Figure 4.6G-H**). Consistent with the known function of miR-122 [118], inhibition of miR-122 using PNA-loaded nanocomposites caused an ~20% decrease in HDL cholesterol. This is, to our knowledge, the first demonstration of in vivo PNA-mediated miR-122 inhibition, and the nanocomposite PNA delivery technology exhibits miR-122 inhibition at 16x lower dose than RNA-based anti-miR122 antagomirs [42], and 2.5x lower dose than a 2-O-methoxyethyl phosphorothioate AMOs [118].

Systemic and intracellular pharmacokinetics limitations are the biggest challenges facing PNA-based therapeutics. Our in vitro and in vivo results confirm that free PNA suffers both from poor cellular internalization, poor systemic pharmacokinetics, and lack of intracellular

bioavailability. Our in vitro data support the importance of overcoming intracellular delivery barriers. Despite a significantly higher level of cell uptake, the uncoated PSNP carriers produced significantly lower miRNA inhibition than composite particles with active endosomal escape capacity (**Figure 4.4**). Furthermore, the nanocomposite showed superior blood circulation time and systemic bioavailability (**Figure 4.6**) due to particle colloidal stabilization with PEG. Finally, PEGDB polymer coating enabled I.V. delivery of a 5x higher PNA dose than uncoated PSNPs. At this PNA dose (5 mg kg^{-1}), composite particles successfully inhibited miR-122 in the liver, de-repressed the miR-122 target gene, *Aldoa*, and lowered plasma cholesterol levels. Thus, the nanocomposite design was strategically crafted to overcome both the key systemic and intracellular delivery barriers facing PNA.

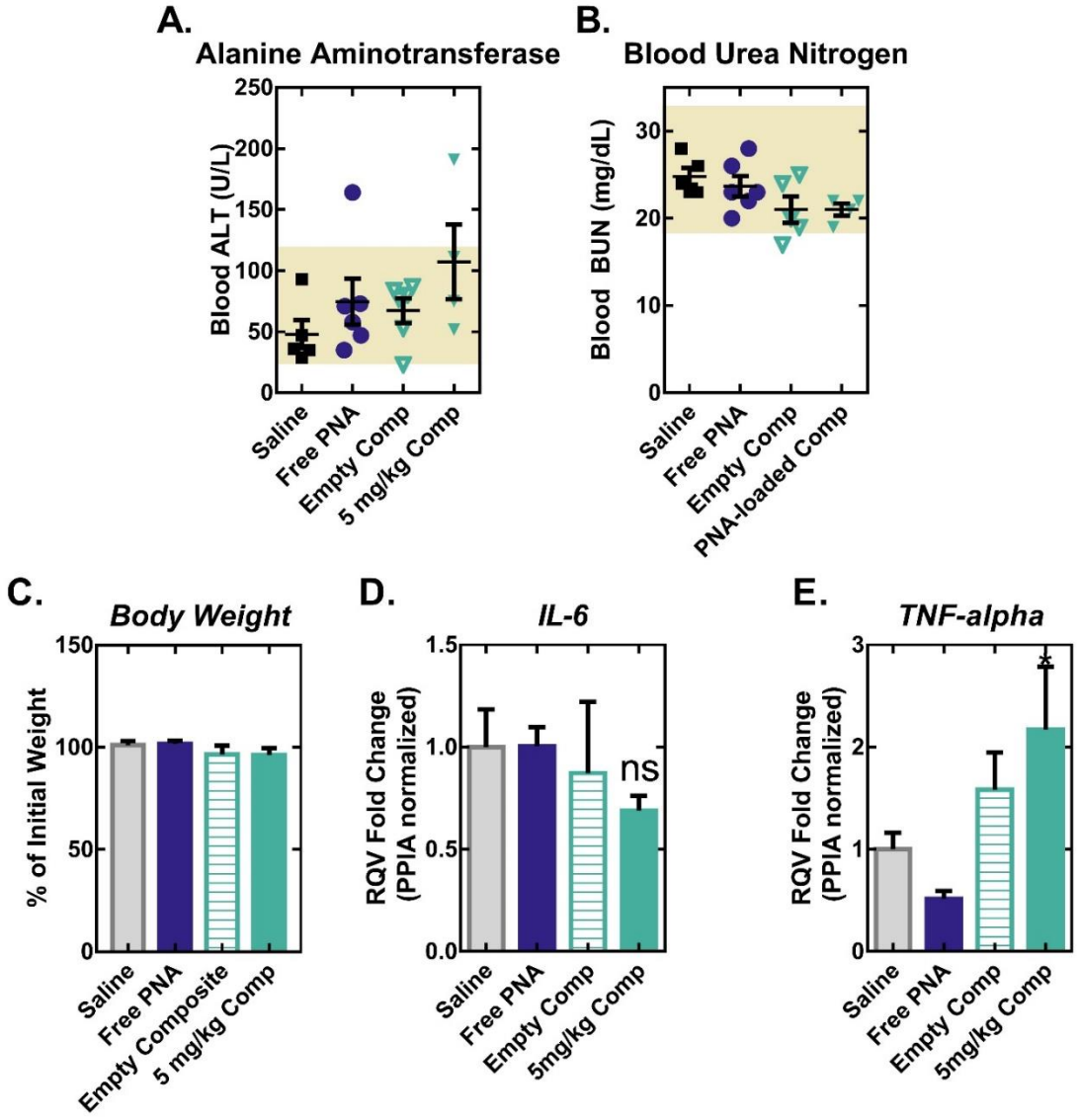

Figure 4.8. Toxicology assessments in mice at day 6 of in vivo miRNA inhibition study (following treatment on days 1, 3, 5 with 5 mg kg^{-1} PNA or equivalent unloaded carrier) showed no signs of toxicity from composite nanoparticles. **A**) Liver toxicity was evaluated by monitoring alanine aminotransferase (ALT) levels in blood, and **B**) kidney toxicity was evaluated by quantifying blood urea nitrogen levels. The healthy range is indicated by the gold shaded region in each graph. **C**) No significant change in body weight was measured 48 h after treatment with 5 mg kg^{-1} PNA treatment, or the corresponding empty vehicle control. Additionally, PCR analysis of livers on day 6 revealed no change in the expression of **D**) IL-6 inflammatory cytokines, whereas levels of the cytokine **E**) TNF-alpha were increased for nanocomposite treatment groups. (*$p<0.05$ compared to saline) [Adapted from *Advanced Materials*, Kelsey R. Beavers et. al., "Porous Silicon and Polymer Nanocomposites for Delivery of Peptide Nucleic Acids as Anti-MicroRNA Therapies", 2016, with permission from John Wiley & Sons, Ltd.]

4.4 Conclusion

This is, to our knowledge, only the fourth report of in vivo miRNA silencing with a PNA therapeutic [66, 68, 69], and the first report of an endosomolytic PNA delivery system. All other reports have focused on inhibition of miR-155 for treatment of lymphoma. Initial work by Fabani et al. modified PNA with positively-charged lysine residues and saw effective miR-155 inhibition at a 50 mg kg^{-1} PNA dose. In the study by Babar et al., PNA encapsulation into PLGA nanoparticles coated with a cell-penetrating peptide (0.35 wt% PNA loading) reduced the effective PNA dose to 1.5 mg kg^{-1}. Cheng et. al. conjugated PNA to a pH-responsive peptide which enables targeted delivery of anti-miRNA PNA to the acidic tumor microenvironment. Additionally, the peptide utilizes an environmentally-activated non-endocytic cell uptake/membrane transduction mechanism. This enabled miR-155 inhibition at a 1 mg kg^{-1} dose in a mouse model of lymphoma. Our non-targeted PNA delivery system beat or approached the level of miRNA inhibitory potency of these different targeted delivery approaches, and we hypothesize that this new long-circulating nanocomposite can be made more potent by adding targeting ligands, such as GalNAc for hepatocyte targeting [123].

In summary, this chapter showcases a new nanocomposite PNA delivery vehicle proven to overcome both systemic and intracellular delivery barriers. Porous silicon is leveraged as a highly porous scaffold amenable to high drug cargo loading; this substrate enables much higher and simpler drug loading relative to water in oil in water (W/O/W) emulsion methods commonly utilized to load hydrophilic cargo into hydrophobic polymer-based nano- and micro- carriers. Furthermore, simple electrostatic assembly was utilized for PSNP surface functionalization with a multifunctional polymer that enhances resultant particle colloidal stability, in vivo circulation, and intracellular bioavailability. This fabrication process is both facile and rapid, requiring only

sequential centrifugal wash steps for composite purification. This approach would also be potentially amenable to adaptation to more controlled microfluidic synthesis techniques, such as those developed by Santos et. al. [68, 124]. Furthermore, it is well-established that porous silicon can host a wide range of cargos [85, 125]. We anticipate that this composite system can facilitate the intracellular activity of a broad range of therapeutic and diagnostic payloads. Finally, based on its high bioavailability and long blood circulation half-life, this system can also potentially be functionalized with active targeting ligands and further tuned to facilitate preferential delivery to defined cells and tissues. Thus, PSNP-polymer nanocomposites represent a promising material platform with potential high impact in miRNA inhibitory and other biologic nanomedicines.

CHAPTER 5

CONCLUSIONS

5.1 Summary

Unraveling the secrets of the human genome, researchers have learned more about the role of non-coding RNAs in disease. The existence of functional non-coding RNAs (like miRNA) now makes sense. MiRNAs are well adapted to silence genes because they share the same nucleic acid language as their targets. Similarly, it seems that nucleic acid-based drugs are ideal for therapeutic silencing of pathological miRNAs. Peptide nucleic acids are excellent miRNA inhibitors, yet they have no innate ability to reach miRNA targets in the body. The challenge in developing clinical anti-miRNA therapies is therefore a challenge of delivery. This works' central hypothesis was that PNA anti-miRNA activity can be improved by engineering PSNPs to increase PNA blood circulation half-life, cellular uptake, and delivery to the cell cytoplasm.

In Aim 1, strategies for loading PNA into PSi were developed and assessed. Covalent attachment of pre-synthesized PNA was found to be the least efficient method of drug loading. Automated *in situ* synthesis of PNA from PSi was developed as an alternative, highly efficient covalent drug-loading strategy. Physical adsorption of PNA was an equally efficient drug loading strategy (due to PSi's high internal surface area), but *in situ* synthesis enabled more control over PNA release kinetics. Ultrasonic fracture of perforated PSi multilayers was then show to be an effective method for producing PSNPs loaded with PNA. These PSNPs are biocompatible and effective at increasing the uptake and activity of anti-miR122 PNA therapeutic in human liver cancer cells.

Aim 2 expanded PNA-loaded PSNP functionality by developing a method to coat these particles with PEGDB polymer. Polymer/PSi nanocomposites, formed by simple electrostatic self-

assembly, possess the pH-responsive endosomal escape properties of PEGDB without sacrificing the high PNA loading efficiency of PSi. As a result, these nanocomposites show increased cytosolic PNA delivery and improved anti-miRNA activity relative to uncoated PSNPs. Increased anti-miRNA activity was seen in spite of the fact that PEGDB decreased PSNP cellular uptake. This result highlights the therapeutic importance of PEGDB endosomal escape functionality.

Finally, Aim 3 assessed the activity of PNA-loaded PSNPs targeted against miR-122 in vivo. PEGDB functionalization was shown to enhance particle colloidal stability, and the PEG block of the polymer made particle surfaces more inert. Consequently, nanocomposites extended the blood circulation half-life of intravenously-delivered PNA from <1 min to 70min, increasing its bioavailability by 73x. Finally, these nanocomposites were shown to be non-toxic and enable PNA-mediated miR-122 inhibition in the liver in vivo, decreasing plasma cholesterol by 20%. The culmination of Aims 1 through 3 is a composite nanoparticle proven to overcome both systemic and intracellular barriers to the delivery of PNA therapeutics.

5.2 Future directions

As discussed in Appendix B, the *in situ* synthesis technique developed as a part of Aim 1 has been applied to PSi-based biosensors. These PNA-functionalized biosensors show enhanced stability and lifetime over current, DNA-based PSi biosensing technologies. Device stability may be further enhanced by alternative linkers for amine functionalization of PSi prior to *in situ* synthesis. In addition, future studies should optimize PNA probe density to strike a balance between device accuracy and sensitivity. Ultimately, the PNA/PSi biosensors should be evaluated using environments and samples that more accurately reflect the demands of their ultimate application.

The nanocomposite developed in Aim 2 showed improved anti-miRNA activity in the liver following systemic administration. The application of these nanocomposites should be extended to more novel miRNA therapeutic targets in the liver, such as those involved in hyperlipidemia and cardiovascular disease. Additionally, the exceptionally long blood circulation half-life of these nanocomposites makes them promising candidates for cancer therapy. Future work should investigate whether or not the extended circulation half-life increases particle accumulation and therapeutic activity in tumors. Finally, the functionality of these nanocomposites may be improved by investigating chemistries that improve PEGDB coating stability and/or incorporate specific targeting moieties onto the particle surface.

5.3 Conclusion

The ability to engineer materials at the nanoscale has expanded our toolkit for overcoming canonical drug delivery challenges. This work described a highly tunable materials system engineered to act as a nanoscale taxi for shuttling therapeutics to their site of action in the body. Using similar nanotechnology to inhibit pathological non-coding RNAs may ultimately herald a new generation of precision medicine.

APPENDIX A

COMPARISON OF PSI OXIDATION METHODS

Fresh porous silicon is covered with silicon hydride. It develops a thin native oxide upon exposure to air. This oxide provides limited resistance against PSNP degradation in biological media. Thermal and chemical oxidation methods are commonly used to tune PSNP degradation kinetics and slow biodegradation. **Figure A.1** shows how increasing the temperature and duration of oxidation can be used to slow the degradation of a PSNP in phosphate buffered saline at 37°C. I studied the feasibility of thermally oxidizing PSNPs, and found that the particles bonded with one another and often remain attached to the walls of their glass container. These results prompted investigations into the chemical oxidation of PSi. I chose to study three chemical oxidants: H_2O, H_2O_2, and piranha acid.

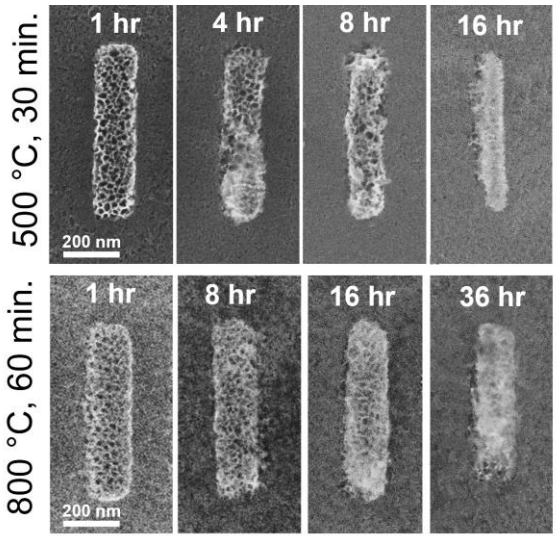

Figure A.1. PSi particle oxidation alters its degradation rate in biological media. The second row demonstrates that increasing oxidation temperature and time increases particle stability.

As PSi oxidizes, its effective refractive index decreases. This is because the refractive index of silicon oxide is ~1.45, whereas the refractive index of silicon is 3.4. Reflectometry was therefore used to compare the extent of oxide formation as a function of oxidation method (**Figure A.2**). Five-micron thick PSi films with 70% porosity were fabricated according to the procedure reported in Section 3.2.1. These films were then oxidized by the methods outlined in **Table A.1**. The change in PSi optical thickness (Δ2nL) before and after oxidation, measured by reflectometry, is given in **Figure A.2**. Of the chemical oxidants studied, high temperature piranha acid was determined to form the thickest oxide in the shortest time, but the subsequent time and particle loss associated with washing piranha from PSNPs limits its utility. At room temperature, submersion into solutions of either H_2O or H_2O_2 for 24 h produce similar changes in optical thickness. Increasing the temperature of the H_2O_2 solution to 115°C shortens the time required to form thick oxides on the PSi surface. H_2O_2 at 115°C for 4 h can produce a change in optical thickness comparable to that of piranha at 115°C for 2h.

Table A.1. List of oxidation methods and corresponding abbreviations.

Abbreviation	Method
H_2O (RT) 24 hr	Submersion into H_2O at room temperature (RT) for 24 h
H_2O_2 (RT) 24 hr	Submersion in H_2O_2 at room temperature (RT) for 24 h
H_2O_2 (115°C) 2 hr	Submersion in H_2O_2 at 115°C for 2 h
H_2O_2 (115°C) 3 hr	Submersion in H_2O_2 at 115°C for 3 h
H_2O_2 (115°C) 4 hr	Submersion in H_2O_2 at 115°C for 4 h
Piranha (115°C) 2 hr	Submersion in Piranha Acid at 115°C for 2 h
600°C 30 min	Oxidation in air at 600°C for 30 min
800°C 1 hr	Oxidation in air at 800°C for 1 h

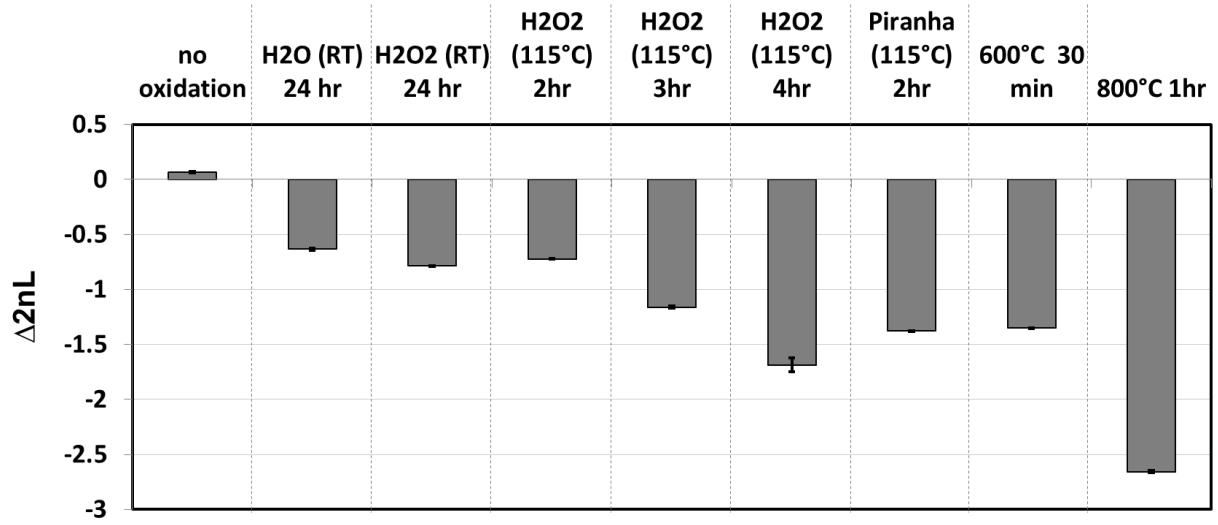

Figure A.2. Change in the value 2nL (where n is the refractive index and L is the thickness of the film) determined by reflectance measurements after oxidation.

Decreasing optical thickness can be caused by PSi dissolution, rather than oxidation. To test for oxide formation, films were analyzed by Fourier transform infrared spectroscopy (FTIR). **Figure A.3** shows a comparison of the FTIR spectra of PSi films left to form a native oxide layer in air for 24 h, submerged in H_2O for 24 h, chemically oxidized with H_2O_2 at 115°C for 4 h, or thermally oxidized in air at 600°C for 30 min. PSi samples exposed to either water or air at room temperature show strong absorption peaks due to Si-Si vibrations, Si-H bending, and Si-H_2 wagging near 615 cm^{-1}. Both also exhibit absorption peaks due to Si-H_2 scissor bending and Si-H stretching at 900 and 2150 cm^{-1}[126]. The lack of oxide bonds on the surface of the water oxidized sample suggests hydrolytic degradation as the primary reason for the previously observed decrease in optical thickness (**Figure A.2**). In contrast, the PSi films oxidized either thermally in air or chemically with H_2O_2 show a marked decrease in absorbance due to Si-Si, Si-H, and Si-H_2 bonds. Instead, strong absorption peaks from SiO_x, O_x-Si-H, and Si-OH bonds appear at 1100, 2245, and 3740 cm^{-1}[127]. Pore morphology after high temperature H_2O_2 oxidation, characterized by scanning electron microscopy (SEM), is similar to that of un-oxidized PSi (**Figure A.4**). This

result, combined with FTIR and reflectometry data, suggests that high temperature H_2O_2 oxidation causes formation of an oxide similar to that formed thermally in air at 600°C for 30 min. Unlike water oxidation, H_2O_2 oxidation does not cause significant hydrolytic degradation.

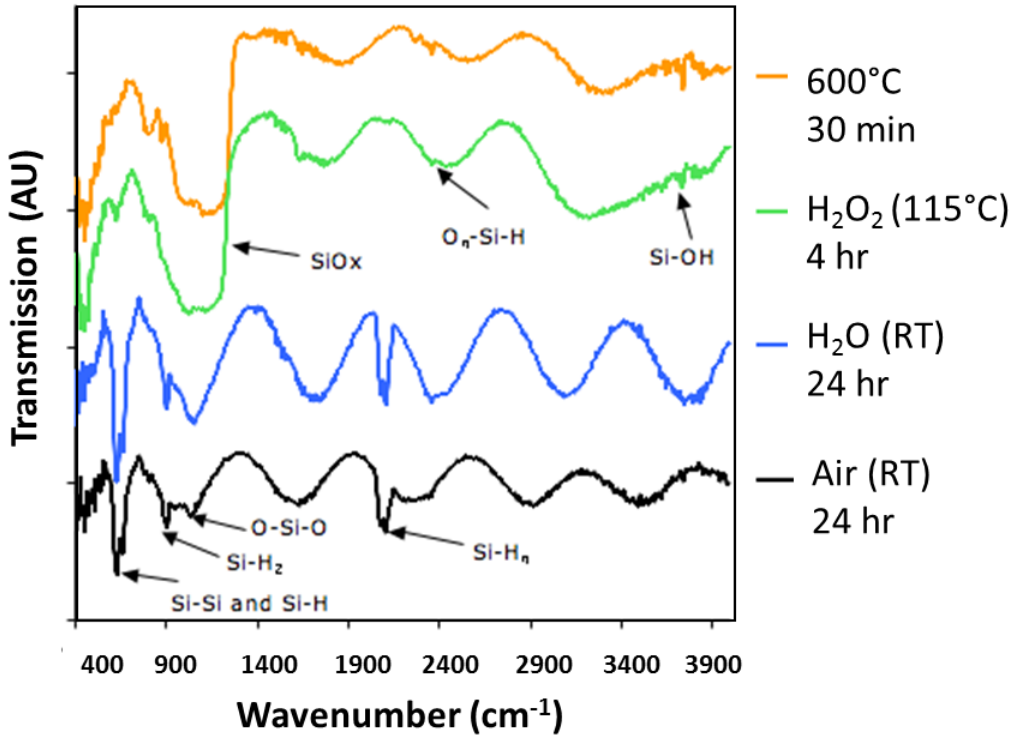

Figure A.3. FTIR spectra of PSi films subjected to various oxidation treatments.

As discussed previously, formation of a thick oxide layer should slow PSi aqueous dissolution. PSi pore morphology was evaluated before and after exposure to deionized water at 80°C for 1 h (**Figure A.4**). PSi films oxidized in H_2O_2 show less dissolution and pore widening than unoxidized PSi. In conclusion, chemical oxidation of PSNPs at 115°C for 4 h is an effective means of slowing PSi hydrolytic degradation and functionalizing the surface with hydroxide species that can be used for subsequent chemical modification.

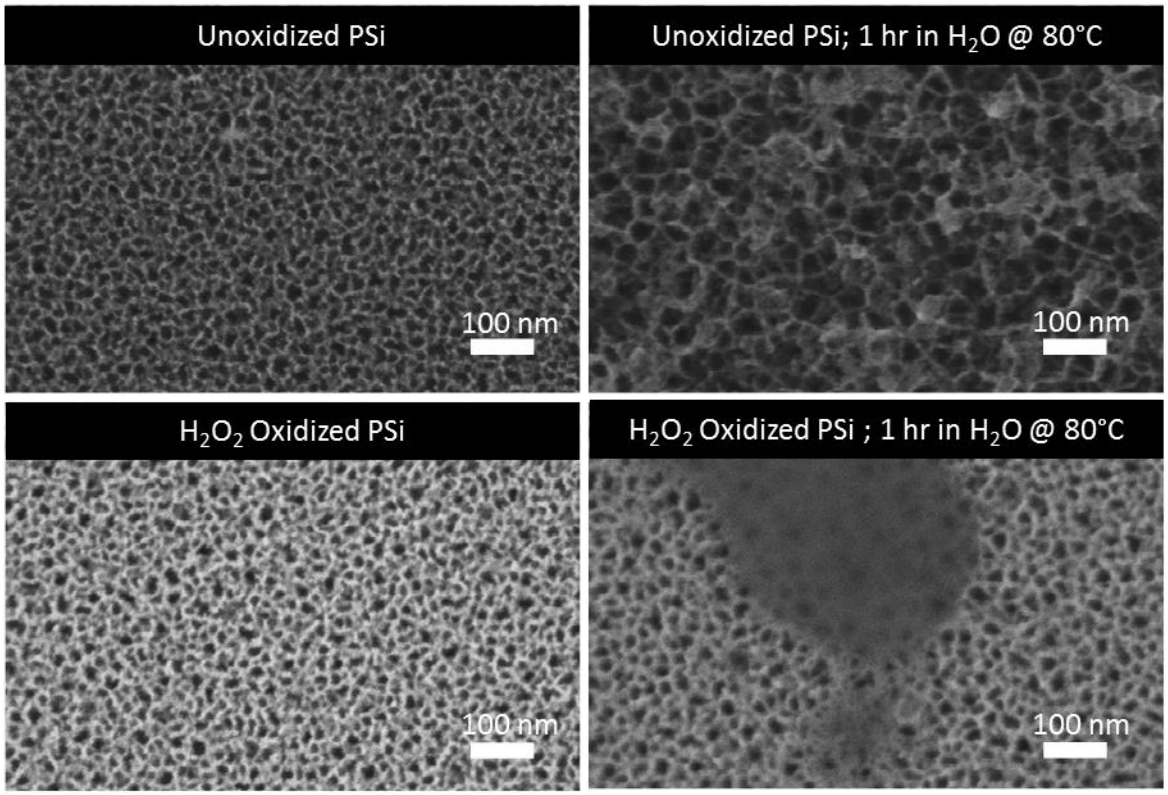

Figure A.4. SEM micrographs of PSi after to exposure to deionized water at 80°C for 1 h shows that high temperature H_2O_2 oxidation slows hydrolytic PSi degradation.

APPENDIX B

IN SITU SYNTHESIS OF PNA IN PSI FOR BIOSENSING

A biosensor is a device that detects an analyte of interest (such as glucose or viral RNA) using a biological probe (such as a protein or DNA) [128]. Biosensors that detect nucleic acids have many applications, including disease diagnosis and detection of food-borne pathogens [129]. To ensure both sensitivity and accuracy, these applications require stable integration of probes onto analytical devices capable of reproducible and sensitive hybridization detection [130, 131]. While nanostructured surfaces like PSi possess advantageous properties for enhancing detection signals [132], a major challenge facing nanostructured biosensors is sensor stability [133]. Our group recently showed that functionalization of PSi biosensors with negatively charged DNA molecules induces PSi corrosion that masks binding events with target molecules [134]. This corrosion is completely mitigated when DNA probes are replaced by charge-neutral PNA probes [134]. In addition to their neutral charge, PNA offer several advantages over DNA and RNA biosensor probes: greater binding affinity for complementary oligos [12] and the ability to form hybrids with less sensitivity to changes in temperature, pH, and ionic strength [11, 51]. Chapter 3 introduced *in situ* PNA synthesis as an effective means for efficient, covalent attachment of PNA to PSi surfaces. This appendix describes the use of *in situ* synthesis to functionalize PSi biosensors.

The first PSi biosensor evaluated in this study is a simple, single-layer, Fabry-Perot interferometer. In these devices, hybridization is detected optically as an increase in optical thickness following capture of the target nucleic acid by probe molecules in the pores. *In situ* synthesis and physical adsorption on PSi yield similar levels of PNA functionalization (Chapter 3). However, *in situ* synthesis results in covalent attachment of PNA to the PSi silicon surface.

We therefore hypothesized that *in situ* synthesis would yield a more stable PSi biosensor. For this investigation, a model 16-mer probe PNA (NH_2-TAG CTA TGG TCC TCG T-COOH) was synthesized from a 10μm thick single-layer PSi film. The stability of a biosensor functionalized with *in situ* synthesized PNA was compared against that of a separate device functionalized with physically adsorbed PNA of the same sequence. Stability was evaluated by soaking PNA functionalized biosensors in deionized water at room temperature for 1 h (**Figure B.1.)**. A decrease in optical thickness following the 1 h presoak indicates instability of the sensor surface, which was apparent only for the physically adsorbed PNA samples (**Figure B.1.A**.). This results supports the hypothesis that covalent attachment of PNA probes increases the stability of PSi biosensors.

Biosensor selectivity was evaluated by incubating with 10 μM solutions containing either a 100% complementary DNA target (NH_2-A CGA GGA CCA TAG CTA-COOH) or a 100% mismatch DNA sequence (NH_2-G GTT TCT GAT GCT GAC-COOH) in HEPES buffer. As shown in **Figure B.1.B.**, negligible change in optical thickness was observed following *in situ* synthesized device incubation with either the mismatch DNA sequence or buffer alone, suggesting that there are no significant non-specific binding events. In contrast, incubation with the complementary DNA target significantly increased the film optical thickness, confirming that DNA hybridized to the complementary PNA probe molecules (**Figure B.1.B**). As a result of its instability, the physically adsorbed device showed significantly less detection sensitivity than the *in situ* synthesized device (**Figure B.1.A**). *In situ* synthesis is, therefore, a more promising means of functionalizing PSi biosensors.

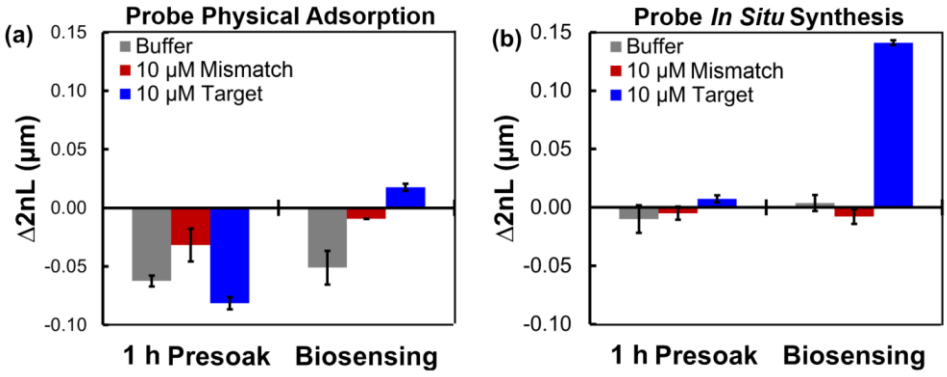

Figure B.1. Stability and selectivity assays on single-layer Fabry-Perot PSi interferometers functionalized with either **A)** physically adsorped, or **B)** *in situ* synthesized 16-mer probe PNA. [Adapted from *Bioconjugate Chemistry*, 25 (7), Kelsey R. Beavers et. al., "In Situ Synthesis of Peptide Nucleic Acids in Porous Silicon for Drug Delivery and Biosensing", 1192-1197, 2014, with permission from the American Chemical Society.]

We next evaluated the applicability of *in situ* PNA synthesis for more sophisticated PSi biosensors. A PSi waveguide is a device that consists of two PSi layers: a low porosity (high refractive index) layer, and a high porosity (low refractive index) layer [135]. A prism can be used to evanescently couple light into the waveguide. The angle at which light couples into the waveguide can be used to monitor hybridization because this resonance angle is dependent on the effective refractive index of the waveguide [135]. **Figure B.2.** shows that a PSi waveguide functionalized by *in situ* PNA synthesis can selectively detect target nucleic acids via an increase in resonance angle. While this result demonstrates selectivity for a 100% complementary sequence relative to a 100% mismatched sequence, the failure sequences resulting from *in situ* synthesis (discussed in section 3.3) may result in false positives due to binding of incomplete probe sequences to partially complimentary targets.

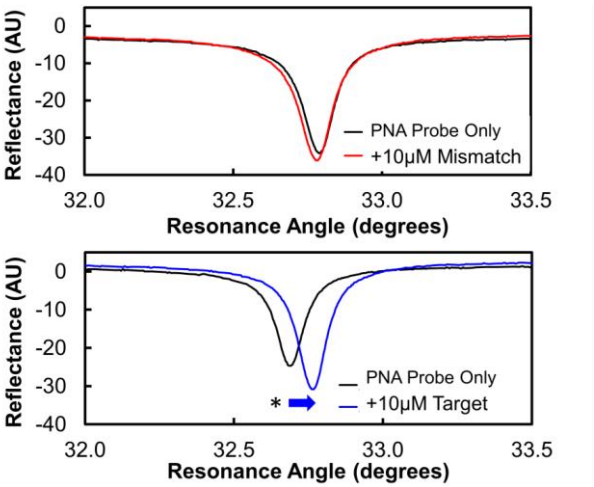

Figure B.2. Optical thickness-based hybridization assay using *in situ* synthesized 16-mer PNA on a PSi waveguide. Sequence-specific hybridization (indicated by a significant increase in resonance angle) was detected with a complementary target sequence but not with a mismatched control sequence. (*p<0.0005).

As discussed in Section 3.3, we hypothesize that incomplete PNA sequences are the result of steric crowing in smaller pores. Findings from studies done on DNA synthesis in controlled pore glass can be applied to estimate the minimum pore diameter (D_{min}) required for efficient PNA synthesis in PSi (**Equation B.1**) [136]. In this equation, the length of the PNA oligo (L_{oligo}) is estimated by multiplying the number of bases (n) with the average length of a single PNA monomer (L_{base}). This value is then added with the length of the linker molecule (L_{linker}) and multiplied by 4, since previous studies have estimated that oligo yield significantly decreases when pore size is less than four times the oligo length [136]. The molecular length of APTES is approximately 8 Å [101], and each PNA base extends a growing oligo by approximately 3.5 Å [102]. Thus, D_{min} for a 16-mer PNA is estimated to be 26 nm. The problem of failure sequences is therefore exacerbated for PSi devices with large populations of pores less than 25 nm in diameter.

$$D_{\min}=(L_{oligo}+L_{linker})\times 4=(nL_{base}+L_{linker})\times 4 \qquad \textbf{Equation B.1}$$

Figure B.3. compares the structures and synthesis coupling efficiencies of two PSi biosensor designs: a 10 um-thick Fabry-Perot interferometer, and a 200 nm-thick waveguide. The average pore size for the interferometer is 25 nm, whereas the average pore size for the waveguide is layer-dependent (**Figure B.3.A**). The low porosity layer of the waveguide has the smallest pore sizes (15 - 25 nm in diameter). Changes in optical thickness reflect the efficiency of PNA monomer coupling during synthesis. Decreasing changes in optical thickness with increasing PNA length correspond to imperfect coupling and creation of failure sequences. The coupling of nucleobases 10-16 is less efficient for the PSi waveguide when compared to the interferometer. This finding, together with the results of the pore widening study presented in **Figure 3.6**, supports our hypothesis that synthesis efficiency is dependent on pore diameter rather than pore length.

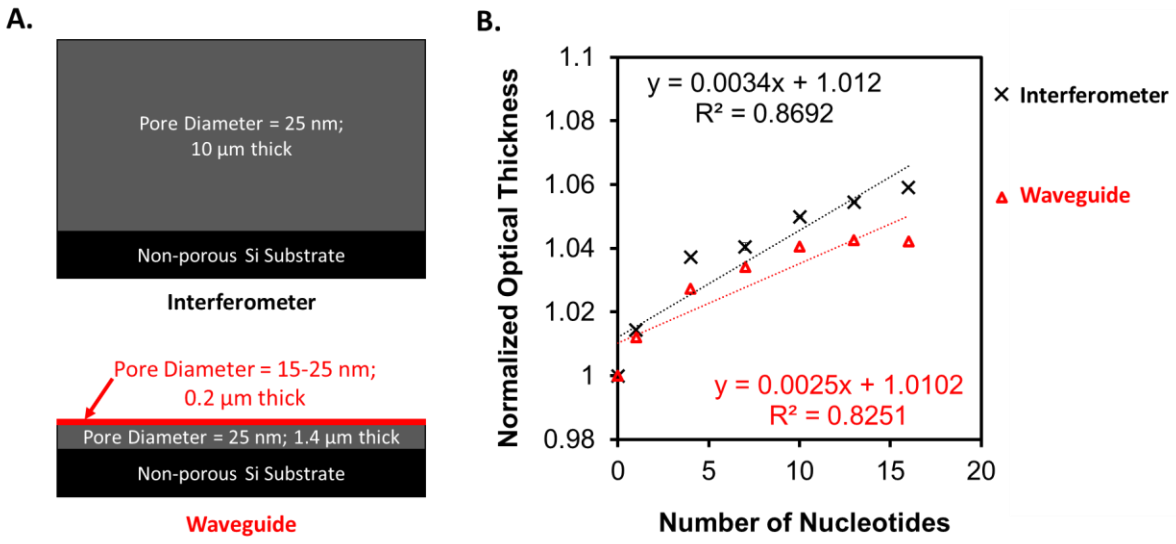

Figure B.3. Comparison of in situ PNA synthesis a PSi interferometer and waveguide. **A)** Cartoon schematics of the structures of a PSi interferometer and waveguide. **B)** Optical thickness profiles during PNA synthesis on the two different devices. Dashed lines indicate linear regression fits for the interferometer (black) and waveguide (red). Note that optical thickness is normalized to the optical thickness of the APTES-coated film for comparison.

Pore widening was previously shown to improve coupling efficiency (Chapter 3). My hypothesis is that this improved efficiency is due to decreased steric crowding of growing PNA oligos. I therefore anticipate that coupling efficiency can also be improved by decreasing the density of reactive sites for PNA synthesis on the PSi surface. To test this hypothesis, I first fabricated PSi films with the interferometer design outlined in **Figure B.3.A**. These films were then silanized with APTES using the same protocol as all previous studies (1% v/v APTES in Toluene incubated for 10 min at room temperature). The optical thickness of all of the silanized films was measured. A Kaiser test for free terminal amines [137] was then used to quantify the amount of grafted APTES on a single PSi sample. Using this information, I set up a series of reactions in which I varied the molar ratio of the nucleobase Adenine ("A") to APTES (**Table B.1**). After coupling, any unreacted amines were capped by acetylation with acetic anhydride.

Table B.1. Molar ratios of Adenine:APTES used in capping study for *in situ* PNA synthesis.

Treatment #	Molar ratio of A:APTES
I	4:1
II	0.75:1
III	0.5:1
IV	0.25:1
V	0:1

The effect of this capping procedure on the density of grafted PNA monomers was evaluated by reflectometry, optical absorbance of the fulvene-piperidine, and Kaiser tests. **Figure B.4** shows that the density of grated PNA monomers on the surface of a PSi biosensor can be tuned by varying the molar ratio of the first base to free amines, then capping unreacted amines. Using this capping procedure, a fresh PSi film was partially reacted with the first nucleobase such that the number of growing oligo chains took up only 20% of the free amines initially available on the

surface. Anti-miR122 PNA (23 nucleobases in length) was then synthesized from the surface of the capped device. **Figure B.5.** compares changes in optical thickness observed during synthesis with and without partial reaction and capping to decrease PNA surface density. As expected, the total shift in optical thickness is lower for the capped device. However, the optical thickness profile on the capped device is more linear than that of the device without capping. This suggests that decreasing the surface density of PNA chains during synthesis increases coupling efficiency. Future studies will need to verify this result by using LCMS to characterize the relative numbers of failure sequences with and without capping.

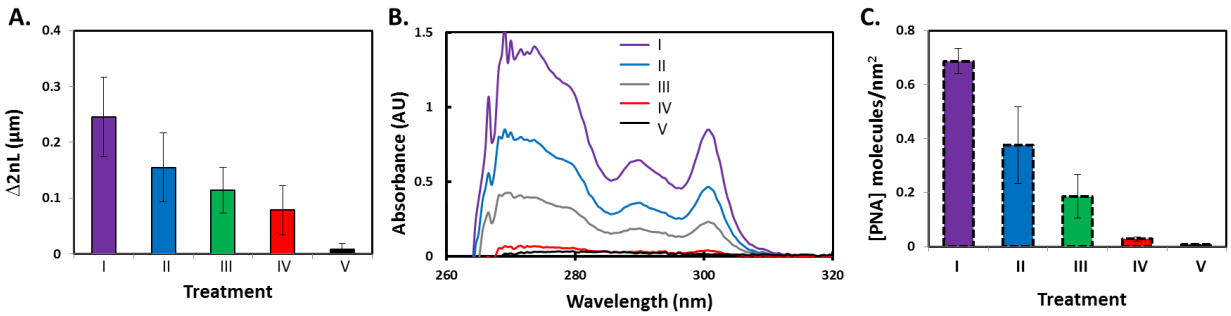

Figure B.4. The **A)** change in optical thickness, **B)** absorbance of the fulvene-piperidine released by deprotection of grafted monomers, and **C)** density of grafted monomers all decrease linearly after reacting with decreasing molar ratios of A:APTES and capping unreacted amines.

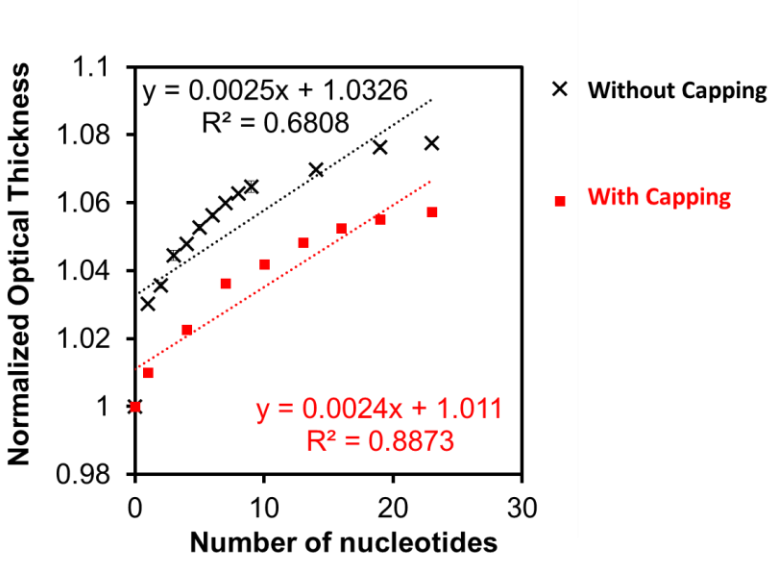

Figure B.5. Optical thickness profiles during PNA synthesis with and without capping to decrease steric crowding. Dashed lines indicate linear regression fits for synthesis without (black) or with (red) partial reaction and capping of free amines at the start of synthesis. Note that optical thickness is normalized to the optical thickness of the APTES-coated film for comparison.

In summary, this appendix has discussed the use of *in situ* synthesis to functionalize PSi nucleic acid biosensors. This method of functionalization was shown to increase biosensor stability relative to devices functionalized by physical adsorption. Furthermore, sequence-specific detection of target nucleic acids was demonstrated for both a PSi interferometer and a PSi waveguide. Pore diameter is shown to have an impact on the purity of synthesized PNA probes, and two strategies are presented to improve coupling efficiency for longer oligos: pore widening and partial reaction of the first base followed by capping. I anticipate that the density of probes on the surface will need to be optimized to allow dense coverage of PNA probes, yet leave adequate space for target nucleic acid hybridization. Further studies will also be needed to investigate whether PSi nucleic acid biosensors based on *in situ* synthesized PNA have superior selectivity and sensitivity relative to traditional DNA probe molecules, as has been suggested for other biosensing platforms [130, 131].

APPENDIX C

SHAPE ENGINEERING PSI FOR DRUG DELIVERY

Particle shape is known to significantly impact the mechanism of cellular internalization as well as the speed and degree of particle uptake [138-140]. In one example, Gratton et al. demonstrated that internalization of cylindrical particles made from cross-linked PEG-based hydrogels depends on aspect ratio (AR) [140]. Of all the particles tested, longer cylinders (150 × 450 nm) were more rapidly internalized by HeLa human cervical carcinoma cells than cubic particles of similar volume (200 × 200 nm) or shorter cylinders (100 × 300 nm). One possible explanation for shape-dependent differences in nanoparticle uptake is that spherical particles are internalized via different pathways [139]. Another possible explanation is that certain aspect ratios are better able to activate membrane-associated signaling cascades that initiate vesicle formation during endocytosis [141].

During endocytosis, macromolecules and solutes are taken into membrane-bound vesicles derived from the plasma membrane [142]. Human hepatocarcinoma (liver cancer) cells are expected to internalize extracellular milieu by clathrin mediated endocytosis, caveolae mediated endocytosis, macropinocytosis, and non-canonical endocytic pathways that are poorly understood [142]. Phagocytosis, a mechanism of solid particulate internalization in immune cells, is likely not a relevant pathway [142]. Each of these pathways is distinguished from the others by the proteins responsible for vesicle formation and the composition of the coating surrounding the endosomal vesicle. Particles larger than 200 nm in size (such as the PSNPs investigated in this study), by simple size exclusion, are unlikely to fit into clathrin-coated pits and caveolae [142]. Thus, macropinocytosis, a high capacity endocytitic mechanism, is the most likely pathway by which

PSNPs are taken up into the huh7 liver cancer cells. The quantities of particles internalized by macropinosomes has been shown to be dependent on particle shape [141]. We therefore investigated whether or not changing the shape of PSNPs affects the route and/or degree of cellular uptake, and if this changes the activity of delivered anti-miRNA PNA therapeutics.

For this investigation, Direct Imprinting of Porous Substrates (DIPS) [25, 143] was used to fabricate rectangular PSi nanoparticles with constant volume, but different aspect ratios (1 and 3.5). A schematic of the DIPS process is shown in **Figure A.1**. Briefly, PSi films are imprinted with a patterned stamp using a hydraulic press (**Figure A.1**). The stamp pattern and PSi film thickness ultimately determine nanoparticle shape and size. Following imprintation, a high-porosity, sacrificial PSi layer is etched beneath imprinted PSNPs bound to the underlying silicon substrate. Particles are then removed from the substrate and suspended in solution by brief ultrasonication. **Figure A.2** shows successful fabrication of shape-engineered PSNPs. The performance of these shape-engineered particles was benchmarked against particles fabricated by ultrasonication of multilayered PSi (Section 4.2.1).

Following fabrication, PSi particles were loaded with anti-miR122 PNA therapeutic and fully coated with PEGDB using the methods described in Chapter 4. The bioactivity of PNA delivered by these differently-shaped PSi nanoparticles was then characterized in the luciferase-expressing Huh7 cells used in Chapters 3 and 4. Cells were treated for 24 h with either 1 μM PNA loaded into PSNPs, or the equivalent amount of empty PSNPs. The results of this study, shown in **Figure C.3**, indicate that the shape of the PSNP delivery vectors had no effect on the anti-miRNA activity of the PNA cargo.

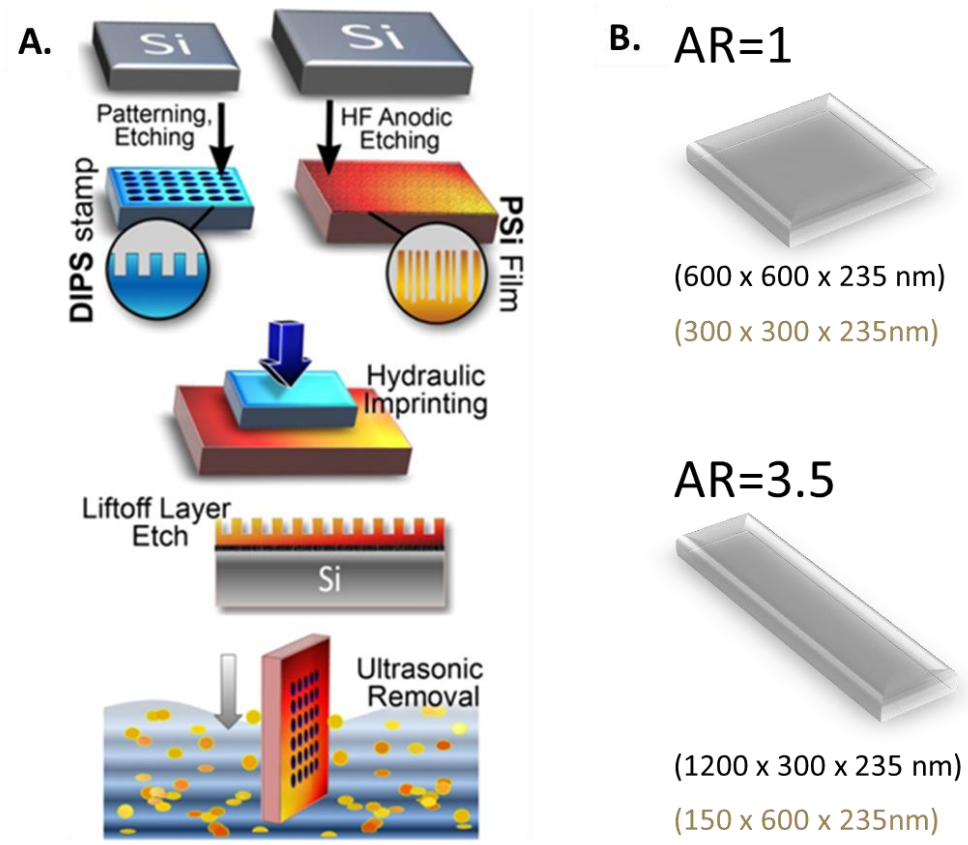

Figure C.1. A) Process flow for DIPS particle fabrication. **B)** Intended morphologies for shape engineered PSNPs with aspect ratios of 1 and 3.5. [Adapted from *Nanotechnology*, 26 (27), Jeremy W. Mares et. al., "Shape-Engineered multifunctional porous silicon nanoparticles by direct imprinting", 2015, with permission from IOP Publishing.]

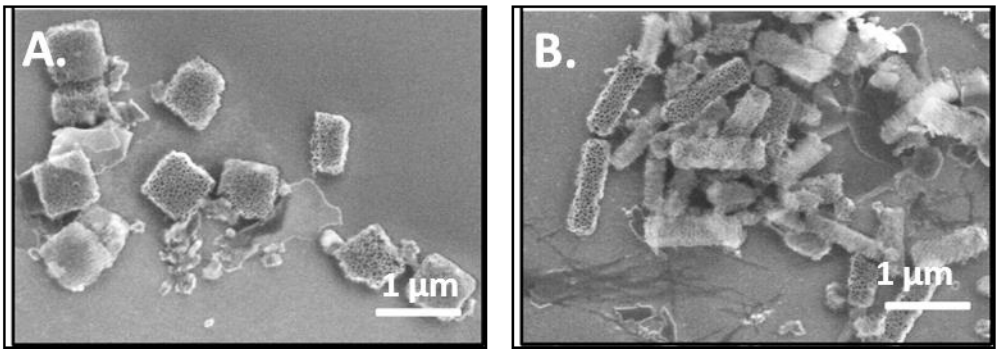

Figure C.2. Scanning Electron micrographs of shape-engineered PSNPs with intended aspect ratios equal to either **A)** 1, or **B)** 3.5, fabricated by the DIPS process.

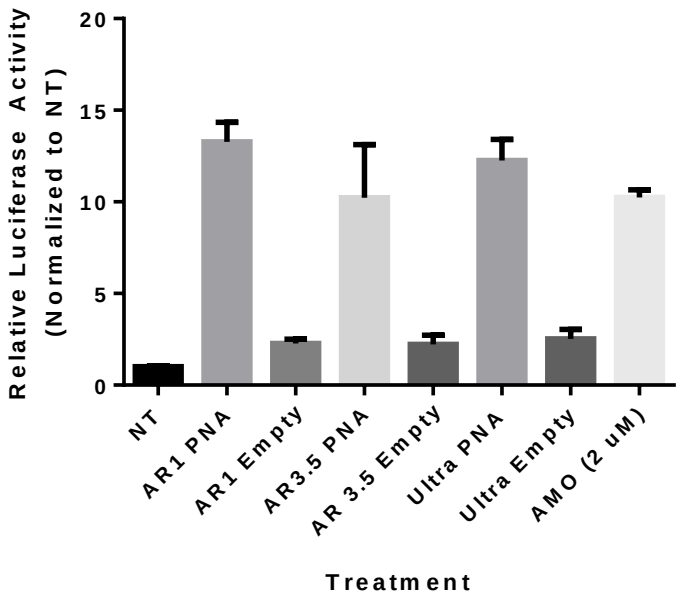

Figure C.3. Shape-engineering of PSNP vectors has no effect on anti-miRNA activity in luciferase-expressing Huh7 cells (1 μM anti-miR122 PNA dose, 24 h treatment). "AR1" and "AR3.5" stand for PSNPs with aspect ratios of 1 and 3.5, respectively. "Ultra" indicates PSNPs which were produced by ultrasonic fracture of multilayer films. "AMO" indicates treatment with a 2'OMe-modified RNA AMO delivered with Fugene6 at a 2 μM dose.

The lack of a shape effect observed in **Figure C.3.** may be attributed to the size of the PSNPs chosen for this study. As mentioned previously, Huh7 cells are limited to micropinocytosis to internalize particles larger than 200 nm in size. It is possible that PSNP shape will have a greater effect on internalization if the largest particle dimension tested is 200 nm. This will be challenging because the minimum dimension that can easily be produced by DIPS is ~100 nm. It is also possible that shape effects are muted by the addition of the PEGDB polymer coating. Additional electron microscopy studies will have to be performed on DIPS particles to determine if they maintain their aspect ratios following PNA loading and PEGDB coating. Even if the impact of PSNP shape is unapparent in in vitro cell culture models, I anticipate that shape engineered PSNPs may improve PNA activity in to context of intravenous or pulmonary PNA delivery in vivo.

REFERENCES

1. Lander, E.S., et al., *Initial sequencing and analysis of the human genome.* Nature, 2001. **409**(6822): p. 860-921.

2. Venter, J.C., et al., *The sequence of the human genome.* science, 2001. **291**(5507): p. 1304-1351.

3. Human Genome Sequencing, C., *Finishing the euchromatic sequence of the human genome.* Nature, 2004. **431**(7011): p. 931-945.

4. Watson, J.D., *Molecular Biology of the Gene*. 2014: Pearson.

5. Lunter, G., C.P. Ponting, and J. Hein, *Genome-wide identification of human functional DNA using a neutral indel model.* PLoS Comput Biol, 2006. **2**(1): p. e5.

6. Waterston, R., et al., *2002b. Initial sequencing and comparative analysis of the mouse genome.* Nature. **420**: p. 520.

7. Esteller, M., *Non-coding RNAs in human disease.* Nat Rev Genet, 2011. **12**(12): p. 861-874.

8. Mack, G.S., *MicroRNA gets down to business.* Nat Biotech, 2007. **25**(6): p. 631-638.

9. Nielsen, P.E., et al., *Sequence-Selective Recognition of DNA by Strand Displacement with a Thymine-Substituted Polyamide.* Science, 1991. **254**(5037): p. 1497-1500.

10. Braasch, D.A. and D.R. Corey, *Synthesis, Analysis, Purification, and Intracellular Delivery of Peptide Nucleic Acids.* Methods, 2001. **23**(2): p. 97-107.

11. Egholm, M., et al., *Pna Hybridizes to Complementary Oligonucleotides Obeying the Watson-Crick Hydrogen-Bonding Rules.* Nature, 1993. **365**(6446): p. 566-568.

12. Ratilainen, T., et al., *Thermodynamics of sequence-specific binding of PNA to DNA.* Biochemistry, 2000. **39**(26): p. 7781-7791.

13. Demidov, V., et al., *Sequence Selective Double-Strand DNA Cleavage by Peptide Nucleic-Acid (Pna) Targeting Using Nuclease S1.* Nucleic Acids Research, 1993. **21**(9): p. 2103-2107.

14. Demidov, V.V., et al., *Stability of peptide nucleic acids in human serum and cellular extracts.* Biochemical pharmacology, 1994. **48**(6): p. 1310-1313.

15. Oh, S.Y., Y. Ju, and H. Park, *A highly effective and long-lasting inhibition of miRNAs with PNA-based antisense oligonucleotides.* Molecules and Cells, 2009. **28**(4): p. 341-345.

16. McMahon, B.M., et al., *Pharmacokinetics and tissue distribution of a peptide nucleic acid after intravenous administration.* Antisense and Nucleic Acid Drug Development, 2002. **12**(2): p. 65-70.

17. Fang, H., et al., *Cationic Shell-Cross-Linked Knedel-like (cSCK) Nanoparticles for Highly Efficient PNA Delivery.* Molecular Pharmaceutics, 2009. **6**(2): p. 615-626.

18. Martinez, J.O., et al., *Engineering multi-stage nanovectors for controlled degradation and tunable release kinetics.* Biomaterials, 2013. **34**(33): p. 8469-8477.

19. Godin, B., et al., *Discoidal Porous Silicon Particles: Fabrication and Biodistribution in Breast Cancer Bearing Mice.* Advanced Functional Materials, 2012. **22**(20): p. 4225-4235.

20. Park, J.-H., et al., *Biodegradable luminescent porous silicon nanoparticles for in vivo applications.* Nature Materials, 2009. **8**(4): p. 331-336.

21. Tasciotti, E., et al., *Mesoporous silicon particles as a multistage delivery system for imaging and therapeutic applications.* Nature Nanotechnology, 2008. **3**(3): p. 151-157.

22. Canham, L. *Porous silicon as a therapeutic biomaterial*. in *1st Annual International Conference on Microtechnologies in Medicine and Biology*. 2000. Lyon.

23. Beavers, K.R., et al., *In situ synthesis of peptide nucleic acids in porous silicon for drug delivery and biosensing.* Bioconjugate Chemistry, 2014. **25(**7): p. 1192-7.

24. Beavers, K.R., et al., *Porous Silicon and Polymer Nanocomposites for Delivery of Peptide Nucleic Acids as Anti-MicroRNA Therapies.* Advanced Materials, 2016: p. n/a-n/a.

25. Ryckman, J.D., et al., *Direct imprinting of porous substrates: a rapid and low-cost approach for patterning porous nanomaterials.* Nano letters, 2010. **11**(5): p. 1857-1862.

26. Canham, L.T., *Properties of Porous Silicon*. 2006: Institution of Electrical Engineers.

27. Mawhinney, D.B., J.A. Glass, and J.T. Yates, *FTIR Study of the Oxidation of Porous Silicon.* The Journal of Physical Chemistry B, 1997. **101**(7): p. 1202-1206.

28. Nelson, C.E., et al., *Balancing Cationic and Hydrophobic Content of PEGylated siRNA Polyplexes Enhances Endosome Escape, Stability, Blood Circulation Time, and Bioactivity in Vivo.* ACS Nano, 2013. **7**(10): p. 8870-8880.

29. Lanford, R.E., et al., *Therapeutic silencing of microRNA-122 in primates with chronic hepatitis C virus infection.* Science, 2010. **327(**5962): p. 198-201.

30. Kang, S., et al., *Macro and small over micro: macromolecules and small molecules that regulate microRNAs.* Chembiochem, 2014. **15**(8): p. 1071-8.

31. Weiler, J., J. Hunziker, and J. Hall, *Anti-miRNA oligonucleotides (AMOs): ammunition to target miRNAs implicated in human disease?* Gene therapy, 2005. **13**(6): p. 496-502.

32. Garzon, R., G. Marcucci, and C.M. Croce, *Targeting microRNAs in cancer: rationale, strategies and challenges.* Nat Rev Drug Discov, 2010. **9**(10): p. 775-89.

33. Gregory, R.I., et al., *Human RISC couples microRNA biogenesis and posttranscriptional gene silencing.* Cell, 2005. **123**(4): p. 631-40.

34. Lee, Y.S., et al., *Depletion of human micro-RNA miR-125b reveals that it is critical for the proliferation of differentiated cells but not for the down-regulation of putative targets during differentiation.* J Biol Chem, 2005. **280**(17): p. 16635-41.

35. Kloosterman, W.P., et al., *Targeted inhibition of miRNA maturation with morpholinos reveals a role for miR-375 in pancreatic islet development.* PLoS Biol, 2007. **5**(8): p. e203.

36. Lennox, K.A. and M.A. Behlke, *Chemical modification and design of anti-miRNA oligonucleotides.* Gene Ther, 2011. **18**(12): p. 1111-1120.

37. Young, J.A., et al., *Regulation of vascular leak and recovery from ischemic injury by general and VE-cadherin-restricted miRNA antagonists of miR-27.* Blood, 2013. **122**(16): p. 2911-9.

38. Lennox, K.A., et al., *Improved Performance of Anti-miRNA Oligonucleotides Using a Novel Non-Nucleotide Modifier.* Mol Ther Nucleic Acids, 2013. **2**: p. e117.

39. Boutla, A., C. Delidakis, and M. Tabler, *Developmental defects by antisense-mediated inactivation of micro-RNAs 2 and 13 in Drosophila and the identification of putative target genes.* Nucleic Acids Res, 2003. **31**(17): p. 4973-80.

40. Hutvagner, G., et al., *Sequence-specific inhibition of small RNA function.* PLoS Biol, 2004. **2**(4): p. E98.

41. Lennox, K.A., et al., *Characterization of modified antisense oligonucleotides in Xenopus laevis embryos.* Oligonucleotides, 2006. **16**(1): p. 26-42.

42. Krutzfeldt, J., et al., *Silencing of microRNAs in vivo with `antagomirs'.* Nature, 2005. **438**(7068): p. 685-689.

43. Krutzfeldt, J., et al., *Specificity, duplex degradation and subcellular localization of antagomirs.* Nucleic Acids Res, 2007. **35**(9): p. 2885-92.

44. Liu, N., et al., *microRNA-133a regulates cardiomyocyte proliferation and suppresses smooth muscle gene expression in the heart.* Genes Dev, 2008. **22**(23): p. 3242-54.

45. Morrisey, E.E., *The magic and mystery of miR-21.* J Clin Invest, 2010. **120**(11): p. 3817-9.

46. Patrick, D.M., et al., *Stress-dependent cardiac remodeling occurs in the absence of microRNA-21 in mice.* J Clin Invest, 2010. **120**(11): p. 3912-6.

47. Obad, S., et al., *Silencing of microRNA families by seed-targeting tiny LNAs.* Nat Genet, 2011. **43**(4): p. 371-8.

48. Fabani, M.M. and M.J. Gait, *miR-122 targeting with LNA/2'-O-methyl oligonucleotide mixmers, peptide nucleic acids (PNA), and PNA-peptide conjugates.* RNA, 2008. **14**(2): p. 336-46.

49. Janson, C. and M. During, *Peptide Nucleic Acids, Morpholinos and Related Antisense Biomolecules*. 2007: Landes Bioscience/Eurekah.com.

50. Natsume, T., et al., *Hybridization energies of double strands composed of DNA, RNA, PNA and LNA.* Chem Phys Lett, 2007. **434**(1-3): p. 133-138.

51. Nielsen, P.E., *Applications of peptide nucleic acids.* Current Opinion in Biotechnology, 1999. **10**(1): p. 71-75.

52. Hyrup, B. and P.E. Nielsen, *Peptide nucleic acids (PNA): synthesis, properties and potential applications.* Bioorganic & medicinal chemistry, 1996. **4**(1): p. 5-23.

53. Prosser, H.M., et al., *A resource of vectors and ES cells for targeted deletion of microRNAs in mice.* Nat Biotechnol, 2011. **29**(9): p. 840-5.

54. Zhu, Q.B., et al., *Sponge Transgenic Mouse Model Reveals Important Roles for the MicroRNA-183 (miR-183)/96/182 Cluster in Postmitotic Photoreceptors of the Retina.* Journal of Biological Chemistry, 2011. **286**(36): p. 31749-31760.

55. Sun, K. and E.C. Lai, *Adult-specific functions of animal microRNAs.* Nat Rev Genet, 2013. **14**(8): p. 535-48.

56. Park, C.Y., et al., *A resource for the conditional ablation of microRNAs in the mouse.* Cell Rep, 2012. **1**(4): p. 385-91.

57. Baigude, H., et al., *Design and creation of new nanomaterials for therapeutic RNAi.* ACS Chem Biol, 2007. **2**(4): p. 237-41.

58. Qian, X., et al., *Star-branched amphiphilic PLA-b-PDMAEMA copolymers for co-delivery of miR-21 inhibitor and doxorubicin to treat glioma.* Biomaterials, 2014. **35**(7): p. 2322-35.

59. Kim, J.H., et al., *Effective delivery of anti-miRNA DNA oligonucleotides by functionalized gold nanoparticles.* J Biotechnol, 2011. **155**(3): p. 287-92.

60. Kim, J.H., et al., *A functionalized gold nanoparticles-assisted universal carrier for antisense DNA.* Chem Commun (Camb), 2010. **46**(23): p. 4151-3.

61. Zhang, M., et al., *Lactosylated gramicidin-based lipid nanoparticles (Lac-GLN) for targeted delivery of anti-miR-155 to hepatocellular carcinoma.* J Control Release, 2013. **168**(3): p. 251-61.

62. Shi, S.J., et al., *Solid lipid nanoparticles loaded with anti-microRNA oligonucleotides (AMOs) for suppression of microRNA-21 functions in human lung cancer cells.* Pharm Res, 2012. **29**(1): p. 97-109.

63. Oh, S.Y., et al., *PNA-based antisense oligonucleotides for micrornas inhibition in the absence of a transfection reagent.* Oligonucleotides, 2010. **20**(5): p. 225-30.

64. Kanasty, R., et al., *Delivery materials for siRNA therapeutics.* Nat Mater, 2013. **12**(11): p. 967-77.

65. Fabbri, E., et al., *miRNA therapeutics: delivery and biological activity of peptide nucleic acids targeting miRNAs.* EPIGENOMICS, 2011. **3**(6): p. 733-745.

66. Fabani, M.M., et al., *Efficient inhibition of miR-155 function in vivo by peptide nucleic acids.* Nucleic Acids Research, 2010.

67. Abibi, A., et al., *Specific versus Nonspecific Binding of Cationic PNAs to Duplex DNA.* Biophysical Journal, 2004. **86**(5): p. 3070-3078.

68. Cheng, C.J., et al., *MicroRNA silencing for cancer therapy targeted to the tumour microenvironment.* Nature, 2015. **518**(7537): p. 107-+.

69. Babar, I.A., et al., *Nanoparticle-based therapy in an in vivo microRNA-155 (miR-155)-dependent mouse model of lymphoma.* Proceedings of the National Academy of Sciences of the United States of America, 2012. **109**(26): p. E1695-E1704.

70. Danhier, F., et al., *PLGA-based nanoparticles: An overview of biomedical applications.* Journal of Controlled Release, 2012. **161**(2): p. 505-522.

71. Uhlir, A., Bell System Tech. J., 1956. **35**: p. 333.

72. Canham, L.T., *Bioactive silicon structure fabrication through nanoetching techniques.* Advanced Materials, 1995. **7**(12): p. 1033-1037.

73. Limnell, T., et al., *Surface chemistry and pore size affect carrier properties of mesoporous silicon microparticles.* International Journal of Pharmaceutics, 2007. **343**(1-2): p. 141-147.

74. Santos, H.A., *Porous silicon for biomedical applications*. 2014: Elsevier.

75. Santos, A. and T. Kumeria, *Electrochemical Etching Methods for Producing Porous Silicon*, in *Electrochemically Engineered Nanoporous Materials*. 2015, Springer. p. 1-36.

76. Qin, Z., et al., *Size Control of Porous Silicon Nanoparticles by Electrochemical Perforation Etching.* Particle & Particle Systems Characterization, 2014. **31**(2): p. 252-256.

77. Lam, C., et al., *Large-scale synthesis of ultrafine Si nanoparticles by ball milling.* Journal of Crystal Growth, 2000. **220**(4): p. 466-470.

78. Jugdaohsingh, R., et al., *Dietary silicon intake and absorption.* The American Journal of Clinical Nutrition, 2002. **75**(5): p. 887-893.

79. Boukherroub, R., et al., *Thermal route for chemical modification and photoluminescence stabilization of porous silicon.* physica status solidi (a), 2000. **182**(1): p. 117-121.

80. Song, J.H. and M.J. Sailor, *Dimethyl Sulfoxide as a Mild Oxidizing Agent for Porous Silicon and Its Effect on Photoluminescence.* Inorganic Chemistry, 1998. **37**(13): p. 3355-3360.

81. Shabir, Q., *Biodegradability of Porous Silicon*, in *Handbook of Porous Silicon*, L. Canham, Editor. 2014, Springer International Publishing: Cham. p. 395-401.

82. Kang, J., et al., *Self-Sealing Porous Silicon-Calcium Silicate Core–Shell Nanoparticles for Targeted siRNA Delivery to the Injured Brain.* Advanced Materials, 2016: p. n/a-n/a.

83. Liu, D., et al., *Co-delivery of a hydrophobic small molecule and a hydrophilic peptide by porous silicon nanoparticles.* Journal of Controlled Release, 2013. **170**(2): p. 268-278.

84. Beavers, K.R., et al., *In situ synthesis of peptide nucleic acids in porous silicon for drug delivery and biosensing.* Bioconjug Chem, 2014. **25**(7): p. 1192-7.

85. Sailor, M.J. and J.-H. Park, *Hybrid Nanoparticles for Detection and Treatment of Cancer.* Advanced Materials, 2012. **24**(28): p. 3779-3802.

86. Ruiz-Esparza, G.U., et al., *A specifically designed nanoconstruct associates, internalizes, traffics in cardiovascular cells, and accumulates in failing myocardium: a new strategy for heart failure diagnostics and therapeutics.* European Journal of Heart Failure, 2016. **18**(2): p. 169-178.

87. Chhablani, J., et al., *Oxidized Porous Silicon Particles Covalently Grafted with Daunorubicin as a Sustained Intraocular Drug Delivery SystemOxidized Porous Silicon for Delivery of Daunorubicin.* Investigative Ophthalmology & Visual Science, 2013. **54**(2): p. 1268-1279.

88. Archer, M., M. Christophersen, and P. Fauchet, *Macroporous silicon electrical sensor for DNA hybridization detection.* Biomed Microdevices, 2004. **6**(3): p. 203 - 211.

89. Furbert, P., et al., *Label-Free Optical Detection of Peptide Synthesis on a Porous Silicon Scaffold/Sensor.* Langmuir, 2008. **24**(6): p. 2908-2915.

90. Sullivan, T.P., et al., *Forced Peptide Synthesis in Nanoscale Confinement under Elastomeric Stamps.* Angewandte Chemie, 2004. **116**(32): p. 4286-4289.

91. McInnes, S.J. and N. Voelcker, *Porous silicon-based nanostructured microparticles as degradable supports for solid-phase synthesis and release of oligonucleotides.* Nanoscale Research Letters, 2012. **7**(1): p. 385.

92. Lawrie, J.L., et al., *Synthesis of DNA oligonucleotides in mesoporous silicon.* Physica Status Solidi (a), 2009. **206**(6): p. 1339-1342.

93. Torres, A.G., et al., *Chemical structure requirements and cellular targeting of microRNA-122 by peptide nucleic acids anti-miRs.* Nucleic Acids Research, 2012. **40**(5): p. 2152-2167.

94. Jopling, C.L., et al., *Modulation of hepatitis C virus RNA abundance by a liver-specific MicroRNA.* Science, 2005. **309**(5740): p. 1577-1581.

95. Arenas, M., et al., *Determination of the complex refractive index of porous silicon layers on crystalline silicon substrates.* International Journal of Modern Physics B, 2010. **24**(24): p. 4835-4850.

96. Filipe, V., A. Hawe, and W. Jiskoot, *Critical evaluation of Nanoparticle Tracking Analysis (NTA) by NanoSight for the measurement of nanoparticles and protein aggregates.* Pharmaceutical research, 2010. **27**(5): p. 796-810.

97. Lewis, J.K., J. Wei, and G. Siuzdak, *Matrix-Assisted Laser Desorption/Ionization Mass Spectrometry in Peptide and Protein Analysis.* Encyclopedia of Analytical Chemistry, 2000.

98. Connelly, C.M., M. Thomas, and A. Deiters, *High-throughput luciferase reporter assay for small-molecule inhibitors of microRNA function.* J Biomol Screen, 2012. **17**(6): p. 822-8.

99. Pacholski, C., *Photonic Crystal Sensors Based on Porous Silicon.* Sensors, 2013. **13**(4): p. 4694-4713.

100. Padmanabhan, S., J. Coughlin, and R. Iyer, *Microwave-assisted functionalisation of solid supports: application in the rapid loading of nucleosides on controlled-pore-glass (CPG).* Tetrahedron Lett, 2005. **46**: p. 343 - 347.

101. Lawrie, J.L., Y. Jiao, and S.M. Weiss, *Size-dependent infiltration and optical detection of nucleic acids in nanoscale pores.* IEEE Transactions on Nanotechnology, 2010. **9**(5): p. 596-602.

102. Rasmussen, H., et al., *The Influence of a Chiral Amino Acid on the Helical Handedness of PNA in Solution and in Crystals.* Journal of Biomolecular Structure and Dynamics, 2004. **21**(4): p. 495-502.

103. Gaur, G., D.S. Koktysh, and S.M. Weiss, *Immobilization of Quantum Dots in Nanostructured Porous Silicon Films: Characterizations and Signal Amplification for Dual-Mode Optical Biosensing.* Advanced Functional Materials, 2013. **23**(29): p. 3604-3614.

104. Anglin, E., et al., *Porous silicon in drug delivery devices and materials ☆.* Advanced Drug Delivery Reviews, 2008. **60**(11): p. 1266-1277.

105. Santos, H.A., et al., *In vitro cytotoxicity of porous silicon microparticles: Effect of the particle concentration, surface chemistry and size.* Acta Biomaterialia, 2010. **6**(7): p. 2721-2731.

106. Mack, G.S., *MicroRNA gets down to business.* Nat Biotechnol, 2007. **25**(6): p. 631-8.

107. Koppelhus, U. and P.E. Nielsen, *Cellular delivery of peptide nucleic acid (PNA).* Advanced Drug Delivery Reviews, 2003. **55**(2): p. 267-280.

108. Leung, A.K.L., *The Whereabouts of microRNA Actions: Cytoplasm and Beyond.* Trends in Cell Biology. **25**(10): p. 601-610.

109. Shahbazi, M.A., et al., *Augmented cellular trafficking and endosomal escape of porous silicon nanoparticles via zwitterionic bilayer polymer surface engineering.* Biomaterials, 2014. **35**(26): p. 7488-7500.

110. Benjaminsen, R.V., et al., *The Possible Proton Sponge Effect of Polyethylenimine (PEI) Does Not Include Change in Lysosomal pH.* Molecular Therapy, 2013. **21**(1): p. 149-157.

111. Boussif, O., et al., *A versatile vector for gene and oligonucleotide transfer into cells in culture and in vivo: polyethylenimine.* Proceedings of the National Academy of Sciences of the United States of America, 1995. **92**(16): p. 7297-7301.

112. Levchenko, T.S., et al., *Liposome clearance in mice: the effect of a separate and combined presence of surface charge and polymer coating.* International Journal of Pharmaceutics, 2002. **240**(1–2): p. 95-102.

113. Camacho, A.I., et al., *Poly(methyl vinyl ether-co-maleic anhydride) nanoparticles as innate immune system activators.* Vaccine, 2011. **29**(41): p. 7130-7135.

114. Herranz-Blanco, B., et al., *On-Chip Self-Assembly of a Smart Hybrid Nanocomposite for Antitumoral Applications.* Advanced Functional Materials, 2015. **25**(10): p. 1488-1497.

115. Connelly, C.M., M. Thomas, and A. Deiters, *High-Throughput Luciferase Reporter Assay for Small-Molecule Inhibitors of MicroRNA Function.* Journal of Biomolecular Screening, 2012. **17**(6): p. 822-828.

116. Evans, B., et al., *Ex Vivo.* Red Blood Cell, 2013.

117. Adolph, E.J., et al., *Enhanced performance of plasmid DNA polyplexes stabilized by a combination of core hydrophobicity and surface PEGylation.* Journal of Materials Chemistry B, 2014. **2**(46): p. 8154-8164.

118. Esau, C., et al., *miR-122 regulation of lipid metabolism revealed by in vivo antisense targeting.* Cell Metabolism, 2006. **3**(2): p. 87-98.

119. Serda, R.E., et al., *The association of silicon microparticles with endothelial cells in drug delivery to the vasculature.* Biomaterials, 2009. **30**(13): p. 2440-2448.

120. Blanco, E., H. Shen, and M. Ferrari, *Principles of nanoparticle design for overcoming biological barriers to drug delivery.* Nat Biotech, 2015. **33**(9): p. 941-951.

121. Xie, G., et al., *Biodistribution and toxicity of intravenously administered silica nanoparticles in mice.* Archives of Toxicology, 2009. **84**(3): p. 183-190.

122. Tsai, W.-C., et al., *MicroRNA-122 plays a critical role in liver homeostasis and hepatocarcinogenesis.* The Journal of Clinical Investigation. **122**(8): p. 2884-2897.

123. Nair, J.K., et al., *Multivalent N-Acetylgalactosamine-Conjugated siRNA Localizes in Hepatocytes and Elicits Robust RNAi-Mediated Gene Silencing.* Journal of the American Chemical Society, 2014. **136**(49): p. 16958-16961.

124. Zhang, H., et al., *Fabrication of a Multifunctional Nano-in-micro Drug Delivery Platform by Microfluidic Templated Encapsulation of Porous Silicon in Polymer Matrix.* Advanced Materials, 2014. **26**(26): p. 4497-4503.

125. Savage, D.J., et al., *Porous silicon advances in drug delivery and immunotherapy.* Current opinion in pharmacology, 2013. **13**(5): p. 834-841.

126. Águila Rodríguez, G., et al., *FTIR and photoluminescence studies of porous silicon layers oxidized in controlled water vapor conditions.* Revista mexicana de física, 2007. **53**(6): p. 431-435.

127. Weng, Y.M., Z.N. Fan, and X.F. Zong, *Luminescence studies on porous silicon.* Applied Physics Letters, 1993. **63**(2): p. 168-170.

128. Turner, A., I. Karube, and G.S. Wilson, *Biosensors: fundamentals and applications.* 1987.

129. Bora, U., A. Sett, and D. Singh, *Nucleic acid based biosensors for clinical applications.* Biosensors Journal, 2013. **2013**.

130. Briones, C. and M. Moreno, *Applications of peptide nucleic acids (PNAs) and locked nucleic acids (LNAs) in biosensor development.* Analytical and Bioanalytical Chemistry, 2012. **402**(10): p. 3071-3089.

131. Wang, J., et al., *Peptide Nucleic Acid Probes for Sequence-Specific DNA Biosensors.* Journal of the American Chemical Society, 1996. **118**(33): p. 7667-7670.

132. Li, J. and N. Wu, *Biosensors based on nanomaterials and nanodevices*. 2013: CRC Press.

133. Beavers, K.R., N.E. Marotta, and L.A. Bottomley, *Thermal stability of silver nanorod arrays.* Chemistry of Materials, 2010. **22**(7): p. 2184-2189.

134. Zhao, Y., et al., *Effect of DNA-Induced Corrosion on Passivated Porous Silicon Biosensors.* ACS Applied Materials & Interfaces, 2014. **6**(16): p. 13510-13519.

135. Rong, G., et al., *Nanoscale porous silicon waveguide for label-free DNA sensing.* Biosensors and Bioelectronics, 2008. **23**(10): p. 1572-1576.

136. Pon, R.T., *Solid-Phase Supports for Oligonucleotide Synthesis*, in *Protocols for Oligonucleotides and Analogs: Synthesis and Properties*, S. Agrawal, Editor. 1993, Humana Press: Totowa, NJ. p. 465-496.

137. Kaiser, E., et al., *Color test for detection of free terminal amino groups in the solid-phase synthesis of peptides.* Analytical Biochemistry, 1970. **34**(2): p. 595-598.

138. Vácha, R., F.J. Martinez-Veracoechea, and D. Frenkel, *Receptor-Mediated Endocytosis of Nanoparticles of Various Shapes.* Nano Letters, 2011. **11**(12): p. 5391-5395.

139. Hao, N., et al., *The shape effect of PEGylated mesoporous silica nanoparticles on cellular uptake pathway in Hela cells.* Microporous and Mesoporous Materials, 2012. **162**(0): p. 14-23.

140. Gratton, S.E., et al., *Nanofabricated particles for engineered drug therapies: A preliminary biodistribution study of PRINT< sup>™</sup> nanoparticles.* Journal of Controlled Release, 2007. **121**(1): p. 10-18.

141. Meng, H., et al., *Aspect Ratio Determines the Quantity of Mesoporous Silica Nanoparticle Uptake by a Small GTPase-Dependent Macropinocytosis Mechanism.* ACS Nano, 2011. **5**(6): p. 4434-4447.

142. Khalil, I.A., et al., *Uptake Pathways and Subsequent Intracellular Trafficking in Nonviral Gene Delivery.* Pharmacological Reviews, 2006. **58**(1): p. 32-45.

143. Mares, J.W., et al., *Shape-Engineered multifunctional porous silicon nanoparticles by direct imprinting.* Nanotechnology, 2015. **26**(27): p. 271001.